A. P. Alexandrov
RESEARCH INSTITUTE
OF TECHNOLOGY
N I T I

INVESTIGATION OF CORIUM MELT INTERACTION WITH NPP REACTOR VESSEL STEEL (METCOR)

Phase №2

Intermediate report
01/10/03 – 31/12/03

INVESTIGATION OF SUBOXIDISED CORIUM INTERACTION WITH VESSEL STEEL UNDER INERT ATMOSPHERE

TEST MC6/03

Project	**Investigation of Corium Melt Interaction with NPP Reactor Vessel Steel (METCOR, Phase 2)**, №833.2
Contracting organization	ISTC
File specification	METCOR2/RPMC6-03
Project location	Aleksandrov Research Institute of Technologies of the RF Ministry for Atomic Energy Russia, 188540, Sosnovy Bor of Leningrad Oblast, NITI

Project manager	Name	V.B. Khabensky
	Signature	
	Date	December, 2003

Authors

Professor	V.B. Khabensky
Doctor	S.V. Bechta
Doctor	V.S. Granovsky
	S.A. Vitol
	E.V. Krushinov
Doctor	S.Ju. Kotova
Professor, Associate member of the Russian Academy of Sciences	V.V. Gusarov
Professor	Yu.B. Petrov
Doctor	I.V. Kulagin
Doctor	D.B. Lopukh
Doctor	A.Yu. Pechenkov
Doctor	I.V. Pozniak
	V.G. Blizniuk
	V.R. Bulighin
	E.K. Kaliago
	N.E. Kamensky
	V.I. Almiashev
	I.A. Loghinov
	A.V. Lisenko
	A.P. Martinov
	V.V. Martinov
	E.V. Shevchenko
	A.A. Chertkov

ABSTRACT

The report presents a description and main results of Test MC of the ISTC Project METCOR, Phase 2, performed by NITI, Sosnovy Bor at the “Rasplav-3” test facility.

Vessel steel ablation during its interaction with molten corium ~C-30 has been studied in oxygen-free atmosphere and at 1400°C on the specimen surface.

CONTENTS

Introduction

In accordance with Work plan [1] and experimental matrix of METCOR, Phase 2 an experiment has been conducted on the interaction between corium melt ~C-30 and vessel steel, the interaction was performed through the crust in oxygen-free atmosphere.

The oxygen-free atmosphere above the melt was simulated by argon. Duration of the test was approx. 10 hours at practically stable temperature conditions on the interaction interface. Maximum temperature on the interacting steel surface was 1400ºC.

Similar to MC5 in MC6 the contact-free monitoring of steel ablation was performed using the ultrasonic sounding technique.

Experimental objective

In the test the vessel steel ablation rate in oxygen-free (argon) atmosphere during its interaction with molten corium ~C-30 through the crust at maximum temperature 1400ºC on the steel specimen surface was studied.

1. Test description

1.1. Experimental setup

Same crucible, as in MC5, was used. The furnace schematics is presented in Fig. 1.1.1.

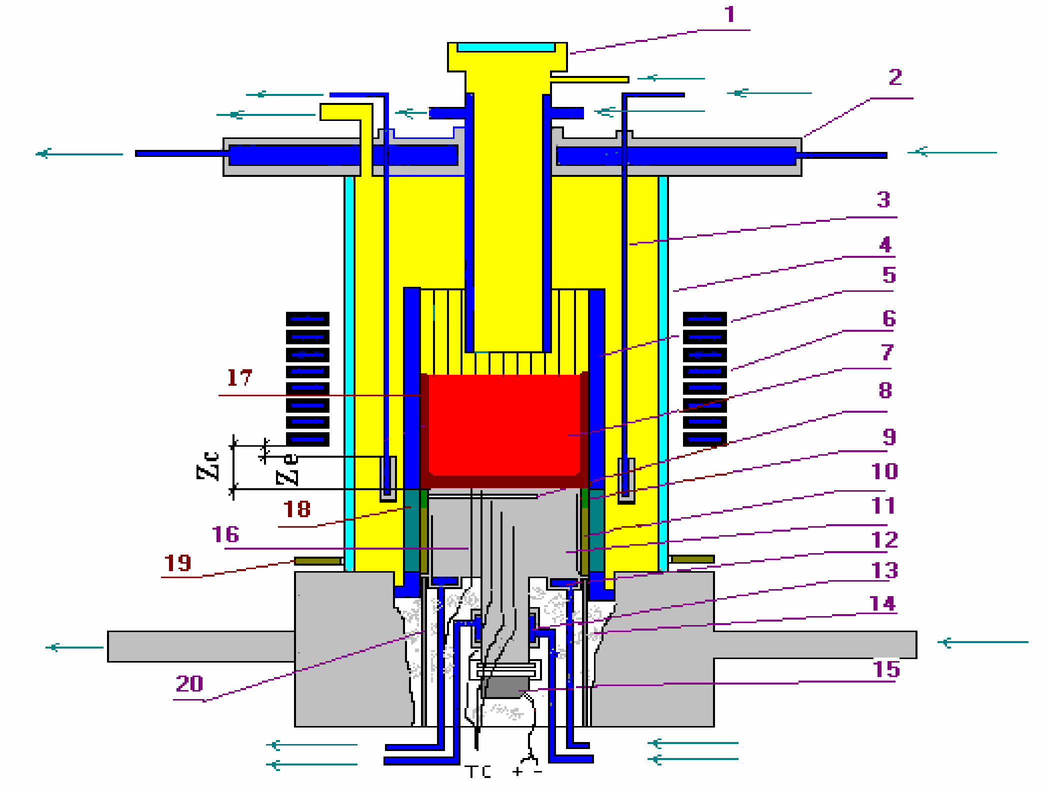

Fig.1.1.1. Furnace schematics

1 – water-cooled pyrometer shaft; 2 – water-cooled cover; 3 – water-cooled electromagnetic screen; 4 – quartz tube; 5 – crucible sections; 6 – inductor; 7 – melt; 8 – acoustic defect; 9 – molten ZrO_2 (fianite); 10 –ZrO_2 powder; 11 – vessel steel specimen; 12 – top specimen calorimeter; 13 – bottom specimen calorimeter; 14 – mullite wool insulation; 15 –ultrasonic sensor; 16 – K-type thermocouples; 17 – crust, 18 – electromagnetic screen (crucible sections are welded); 19 – uncooled electromagnetic screen; 20 – cylindrical support of the specimen.

The vessel steel specimen (11) used in the test is shown in Fig.1.1.2. In order to determine heat fluxes from melt to specimen and cooling of the zone, where the ultrasonic sensor (USS) was attached to the specimen, two calorimeters were provided – a top calorimeter (12) and a bottom calorimeter (13).

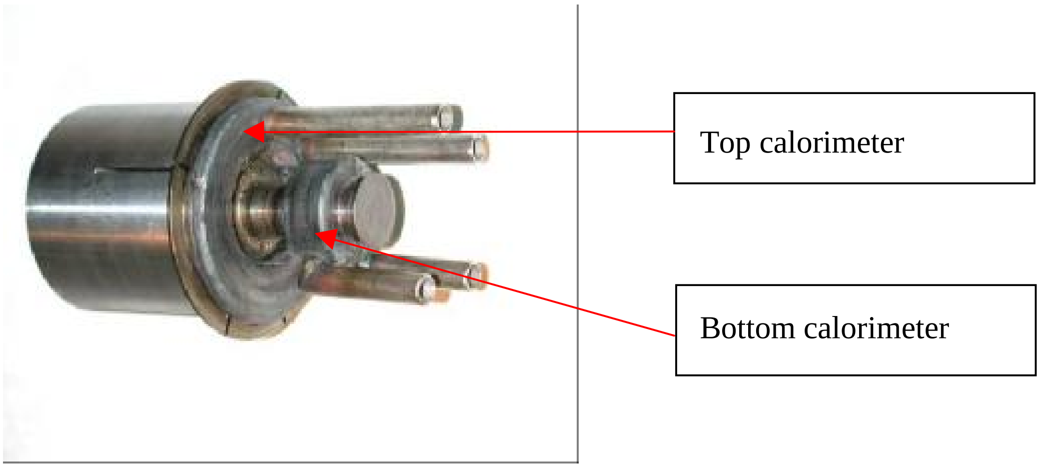

Fig.1.1.2. Vessel steel specimen

Table 1.1.1 presents the locations of K-type thermocouple junctions, which were embedded into the specimen. Thermocouples located at 10mm from the specimen axis, were placed into ø1.5mm holes, and those located at 29 mm – into the 1.5mm grooves.

Table 1.1.1

Thermocouple hot junction locations

№	α^o (horizontal angle)	r, mm (distance from specimen axis)	h, mm (distance from the top)
TC01	0	10	0
TC02	90	10	2
TC03	45	10	4
TC04	135	10	6
TC05	270	10	6
TC06	180	10	8
TC07	225	10	20
TC08	315	29	0
TC09	90	29	2
TC10	45	29	4
TC11	225	29	20
TC12	180	29	40
TC13	45	7.5	102.2

To exclude electromagnetic heating of the specimen the crucible sections were welded together in the lower part of crucible top, this arrangement served as an electromagnetic screen (18). Specimen was positioned in the crucible so that its top was 1 mm below the top of welded sections. The gap between the specimen and crucible sections was filled with ZrO_2 powder (10) and pellets of molten ZrO_2 (fianite)(9). An additional shielding of specimen from electromagnetic heating and control of the pool bottom crust thickness was performed using water-cooled movable screen (3). An argon-sparged pyrometer shaft (1) was used for the melt surface monitoring.

An acoustic defect (8) was made in the specimen for studying steel corrosion rate, the same ultrasonic sensor (15) as in MC5 was used for the purpose. The furnace was insulated with quartz tube (4) and water-cooled cover (2).

Gas-aerosol sampling system (Fig. 1.1.3) was assembled for the monitoring of oxygen partial pressure in the off gases of the furnace and for making the experiment mass balance. Oxygen content was measured with electrochemical sensor (12). Alternatively connected large-area filters (LAF) (9) were used to remove aerosols from the off-gas. Gas flow parameters (flow rate, pressure) were kept under control by electromechanic flow-rate meters G1, G2 of OP-40/C-type, rotameters G3, Motorolla pressurizers Pr01,02,03,06. Silica gel dehumidifier (2) was incorporated into the furnace inlet scheme to provide the complete drying of the incoming gas. The gas was supplied into the furnace from the top through shaft (4) in order to blow aerosols off and make pyrometric measurements and video recording possible.

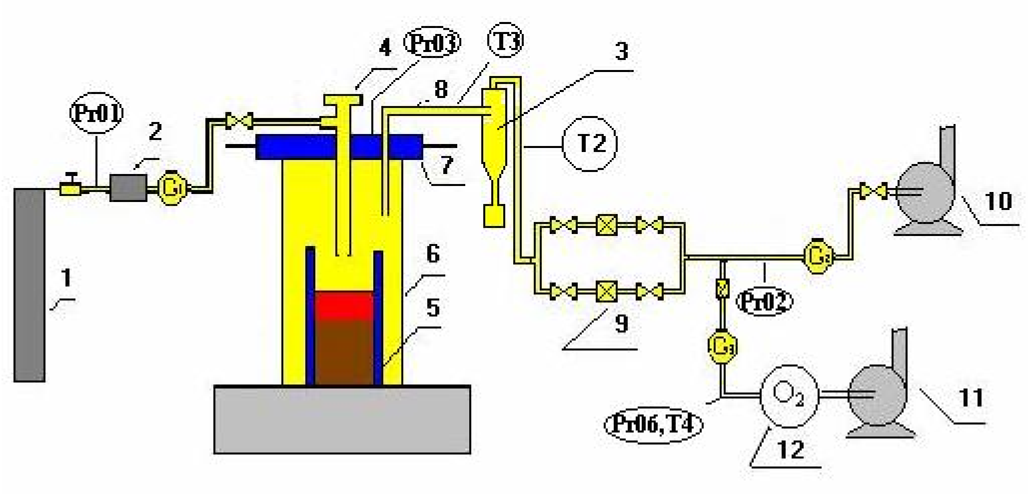

Fig.1.1.3. Gas in and out

1 – Ar tank; 2 – silica gel dehumidifier; 3 – cyclone;4 - Ar-sparged pyrometer shaft; 5 - crucible; 6 – quartz tube; 7 – water-cooled cover; 8 – aerosol pathway; 9 - LAF filters; 10-fan; 11 - vacuum pump; 2 – oxygen sensor; PrO1-O3, PrO6 – pressurizers; G1,2– flow-rate meters, G3-rotameter;T1-T4 thermocouples

1.2. Materials

The following materials were used in the test: vessel steel 15Kh2NMFA-A, uranium dioxide, zirconium oxide, metallic zirconium, argon. The basic component of all materials used was subjected to the analysis. The oxygen/uranium ratio was determined for uranium dioxide powder, it was 2.0. Table 1.2.1 gives the corium charge inventory.

The charge was put into the crucible in argon atmosphere using a technology developed in test MC5. 150 g of corium was placed on the specimen top, the corium had C-27.0 composition (76.4%UO_2; 7.9% ZrO_2; 15.7%Zr), here and hereafter mass.%), particle dispersiveness ≤ 50 μm. Corium C-27.0 had been synthesized in argon in a separate test Pr1-MC6. The charge composed from UO_2, ZrO_2 powder and metallic zirconium C-32 (76.00%UO_2; 9.33% ZrO_2; 14.67%Zr) was put on its top.

Table 1.2.1

Corium charge inventory

Component	Content of the basic substance, %	Admixtures, %	Note
UO_2	> 99.0	Fe < 0.03; As < 0.0003; Cu < 0.01; phosphates < 0.002; chlorides < 0.003	Certificate data; thermogravimetry
ZrO_2	(ZrO_2+ HfO_2) > 99.3	Al_2O_3<0.03; Fe_2O_3<0.05; CaO<0.03; MgO<0.02; SiO_2<0.2; TiO_2<0.1; P_2O_5<0.15; (Na_2O+K_2O)<0.02	Certificate data
Zr	alloy H-1	Nb<1.0	XRF

Compositions and mass of components, which were put into the crucible before melting, are given in Table 1.2.2.

Table 1.2.2

Charge composition and mass

Function	Component	Fraction, µm	Mass, g	%
Crust simulator	Corium C-27.0 (76.4%UO_2; 7.9% ZrO_2; 15.7%Zr)	< 50	150	8.1
Main charge	UO_2	< 500	1292.0	69.8
	ZrO_2	< 50	158.6	8.6
	Zr	Pins 3 mm in diameter and 15 mm high	249.4	13.5
Total			1850.0	100.0

The required fractions of UO_2 and corium were obtained by crushing tablets taken from fuel elements and a corium C-27.0 ingot, which had been synthesized in Pr1-MC6, the crushing was performed in argon.

1.3. Experimental procedure

In the beginning the furnace was blown with argon (flow rate 10 l/min) for 10 minutes. This was followed by the start-up heating and molten pool production. In order to prevent the uncontrolled specimen heating its top was positioned 35 mm below inductor bottom, and the screen top was positioned level with the inductor bottom. The specimen top temperature was monitored using thermocouple readings. The following manipulations were made during molten pool formation:

- 340 sec. The screen was lowered by 10 mm.
- 486 sec. The crucible was moved into the inductor by 10 mm (in accordance with the design the crucible moves together with the screen).
- 672 sec. The screen was lowered by 5 mm.
- 873 sec. The screen was lowered by 5 mm.
- 1861 sec. The screen was lowered by 5 mm.
- 2228 sec. The crucible was moved into the inductor by 5 mm.

These manipulations resulted in the molten pool formation, at that time the specimen top was 20 mm below the inductor bottom and 10 mm – below the screen. After this, the crucible and screen were not moved, temperature on the specimen top was stabilized by adjusting voltage on the anode of generator.

In accordance with thermocouple indications, at 3200 sec. the specimen top temperature reached ~ 1300ºC and after this, following the experimental plan, the temperature was kept stable for 10 hours and ablation kinetics of vessel steel attacked by corium through the crust was studied. Fig.1.3.1. presents the dynamics of heat fluxes into the crucible and inductor, anode current and voltage. Readings of specimen thermocouples, which were taken throughout the test, are given in Fig.1.3.2 and 1.3.3. Fig 1.3.4 shows heat fluxes into the top and bottom specimen calorimeters vs. time. Sharp increases in heat fluxes are explained by the following: at 3300 sec. water started to boil in the top calorimeter, this was eliminated by increasing the water flow rate; at 5700 sec. pressure of water supplied into the bottom and top calorimeters dropped. After the 10-hour exposition, at 39360 sec. the melt sample was taken and frozen in argon. Throughout the test the molten pool surface was periodically recorded on video.

At 39500 sec. the heating was disconnected and ingot was cooled in argon together with the specimen. The cooled specimen and ingot were taken from the crucible without breaking the specimen-corium interaction boundary. After this the specimen and ingot were embedded in epoxy resin and cut along the axis in order to determine the ablation depth and interaction front boundaries. Figs 1.3.5, 1.3.6, 1.3.7 show the crucible after the test, the specimen with corium ingot and their cross section.

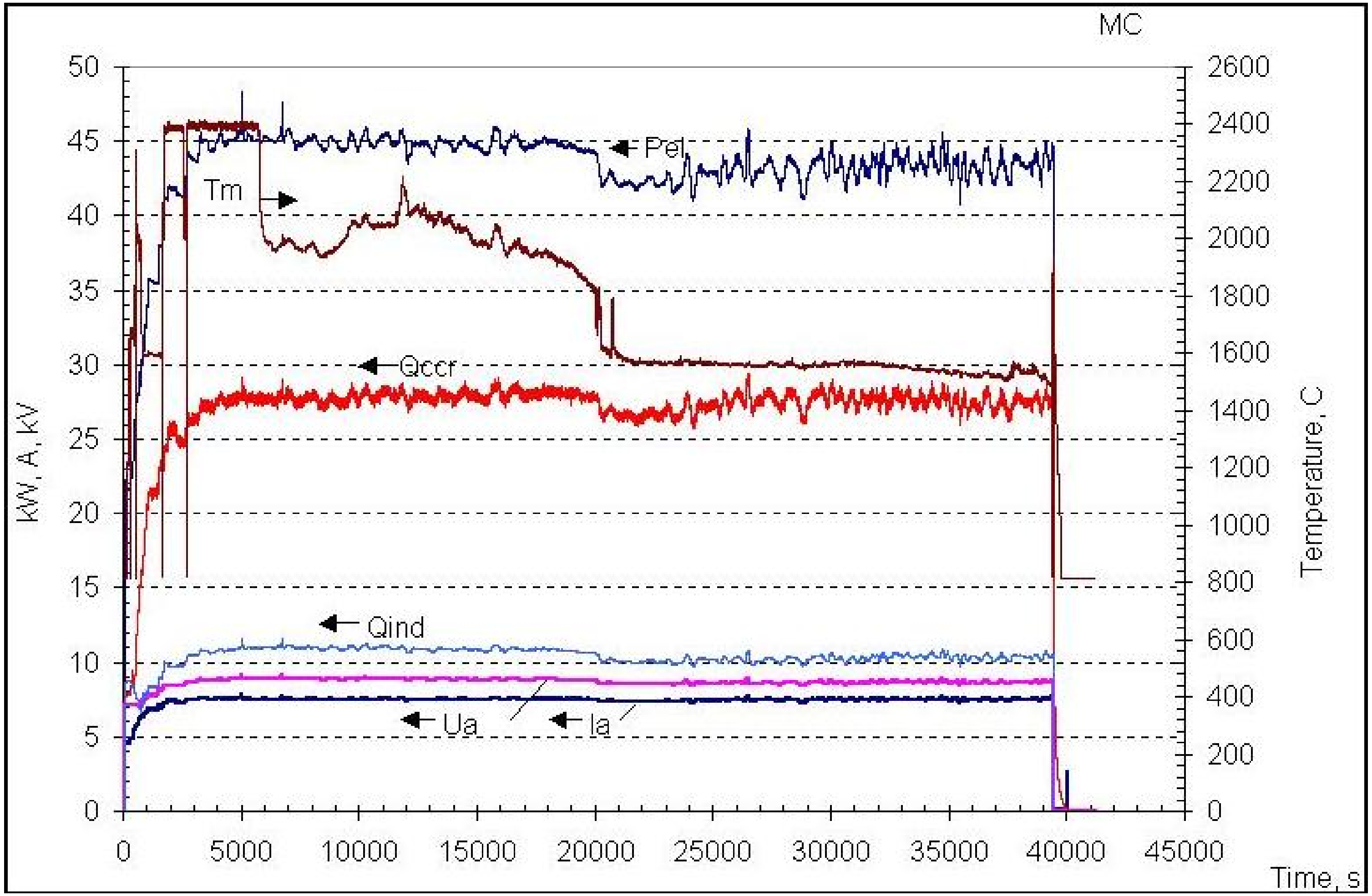

Q_{ccr}- heat flux into the crucible; Q_{ind} – heat flux into the inductor; Q_{cal} – heat flux into the calorimeter; Pel – total electric power, Tm-pyrometer readings; Ia – anode current; Ua- anode voltage.

Fig.1.3.1. Variation of heat and electromagnetic fluxes; anode current and voltage; pyrometer indications

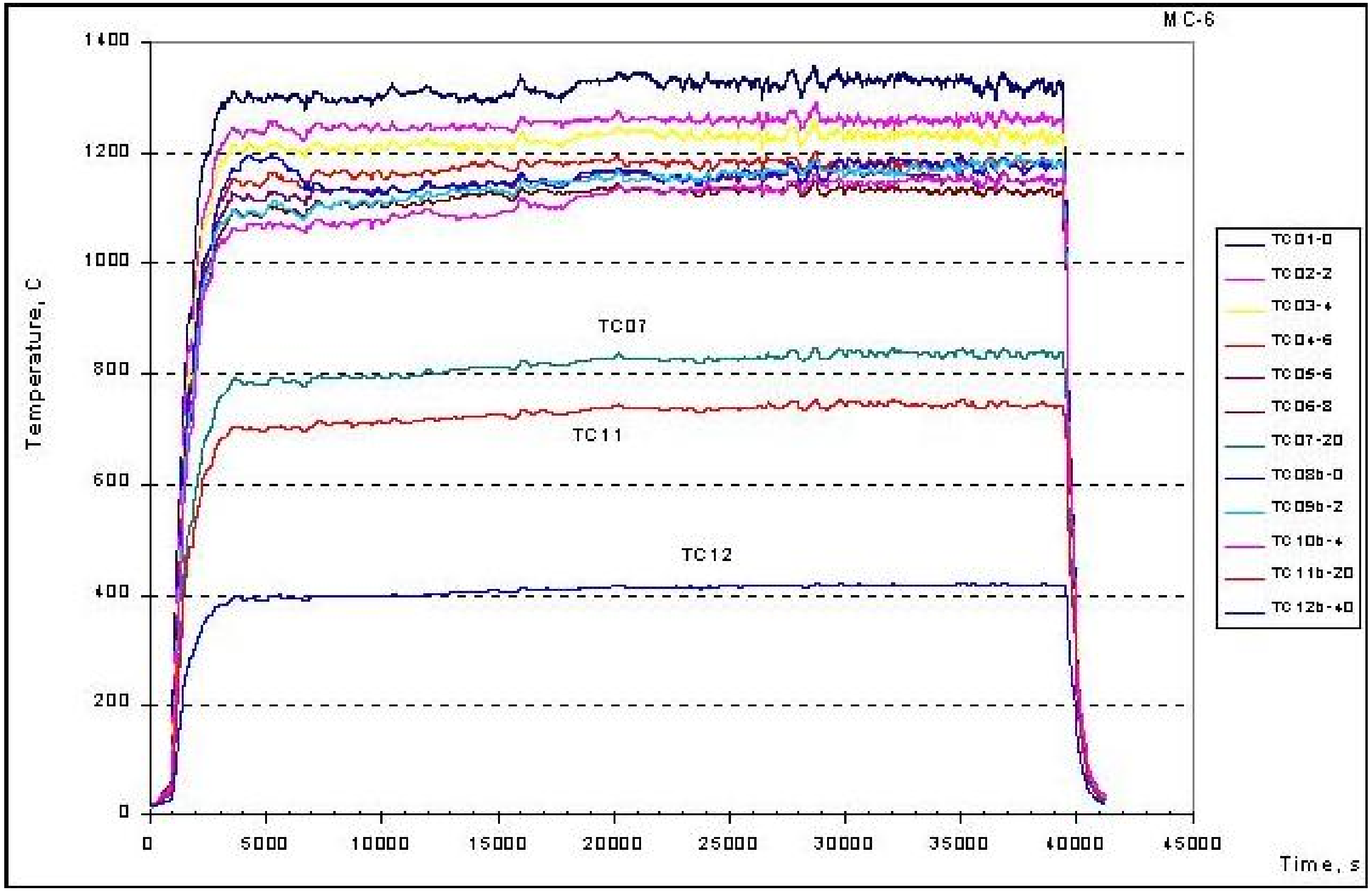

Fig. 1.3.2. MC6 thermocouple readings

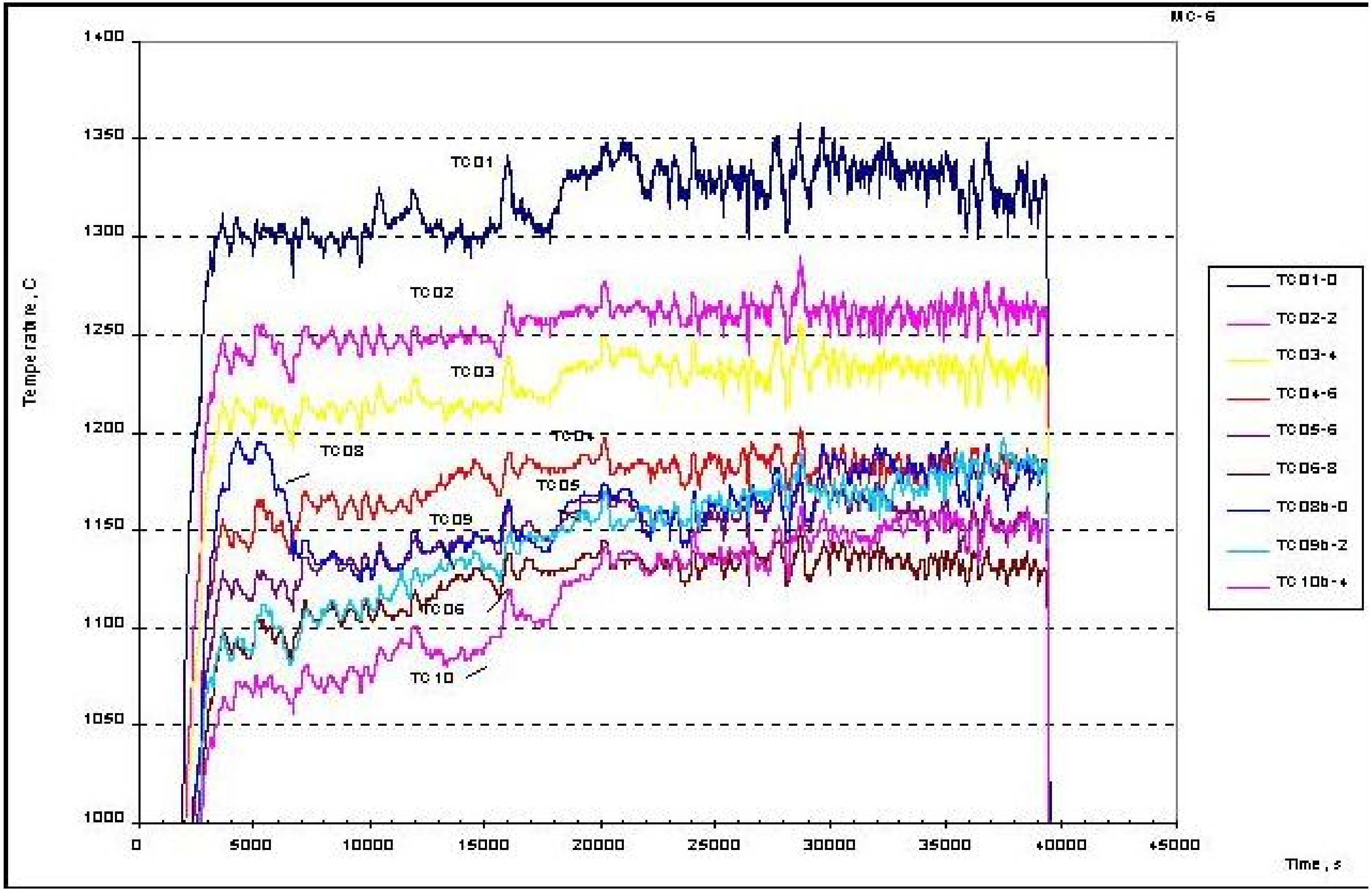

Fig. 1.3.3. MC6 thermocouple readings

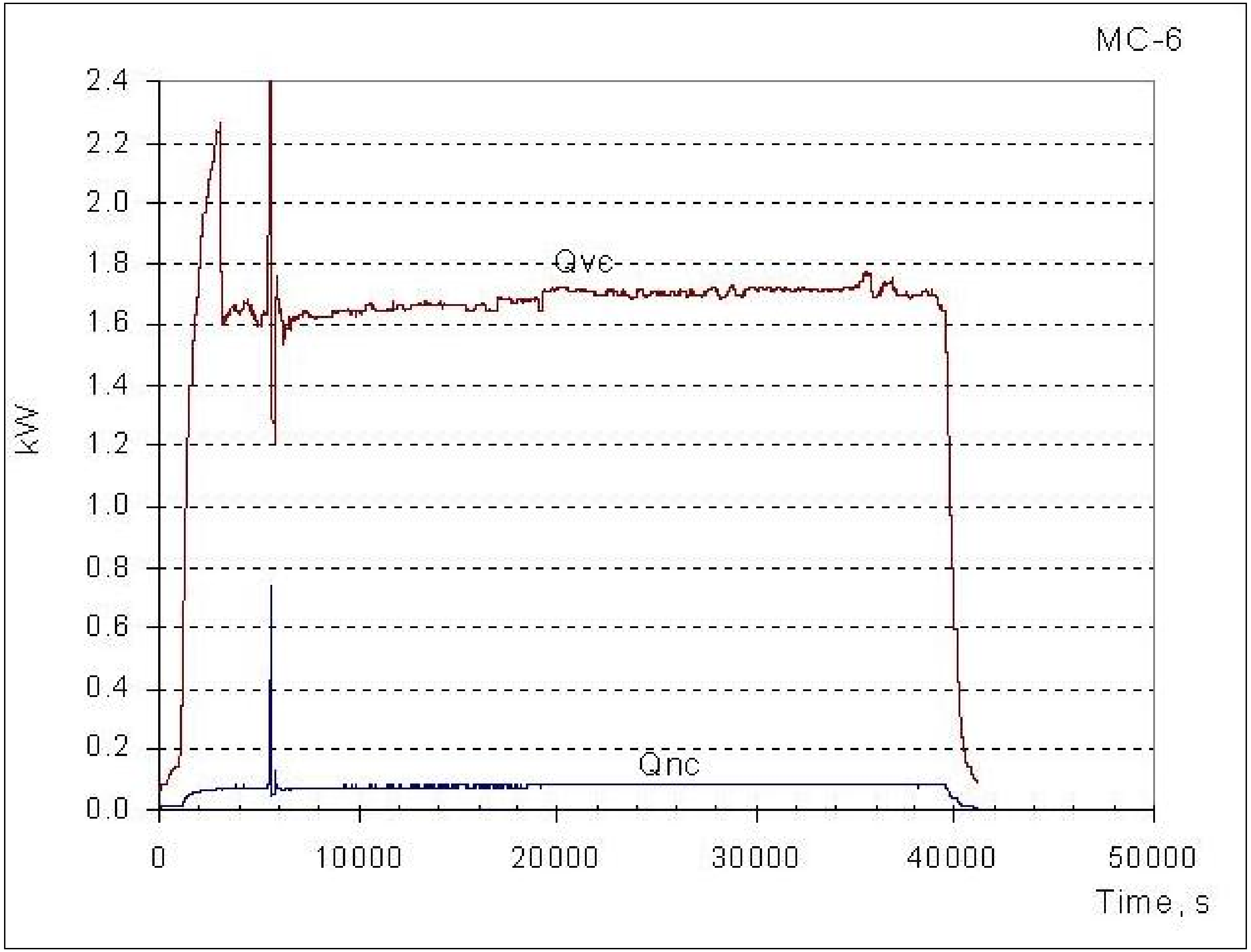

Fig.1.3.4. Heat fluxes into the top and bottom calorimeters vs. time

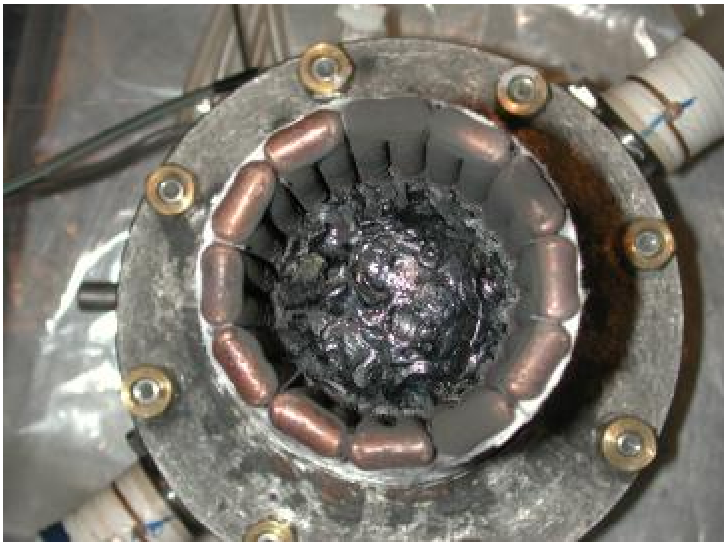

Fig.1.3.5. Crucible after the test

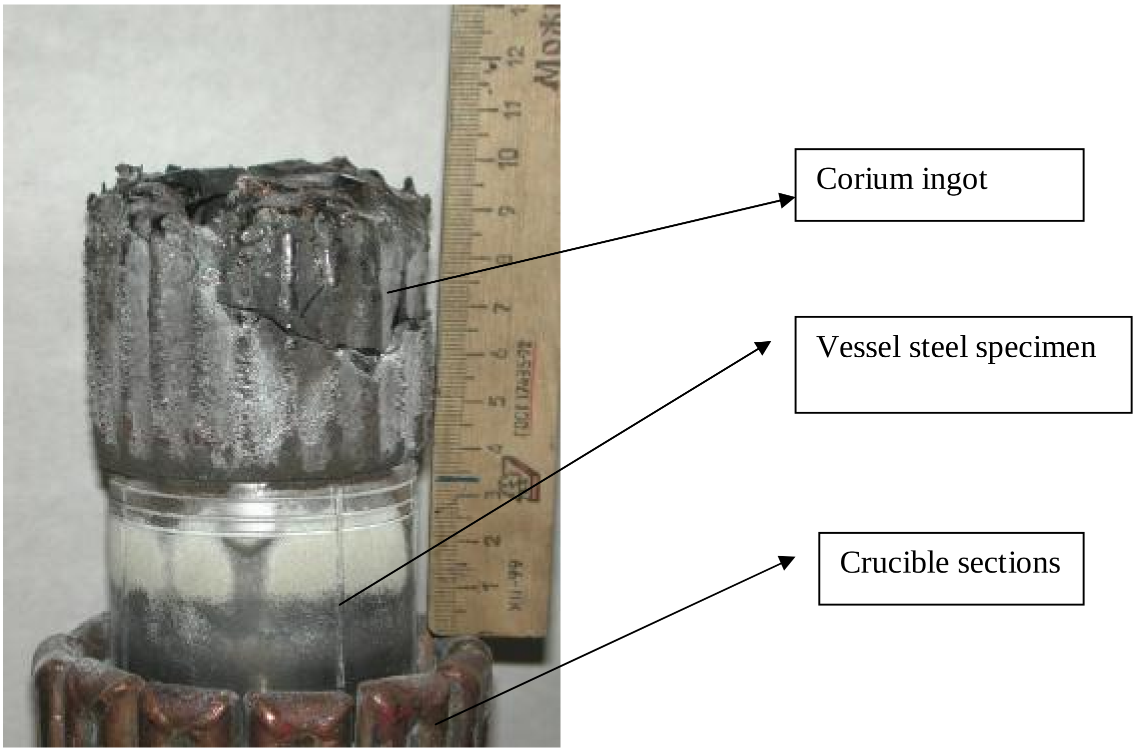

Fig.1.3.6. Vessel steel specimen with corium ingot

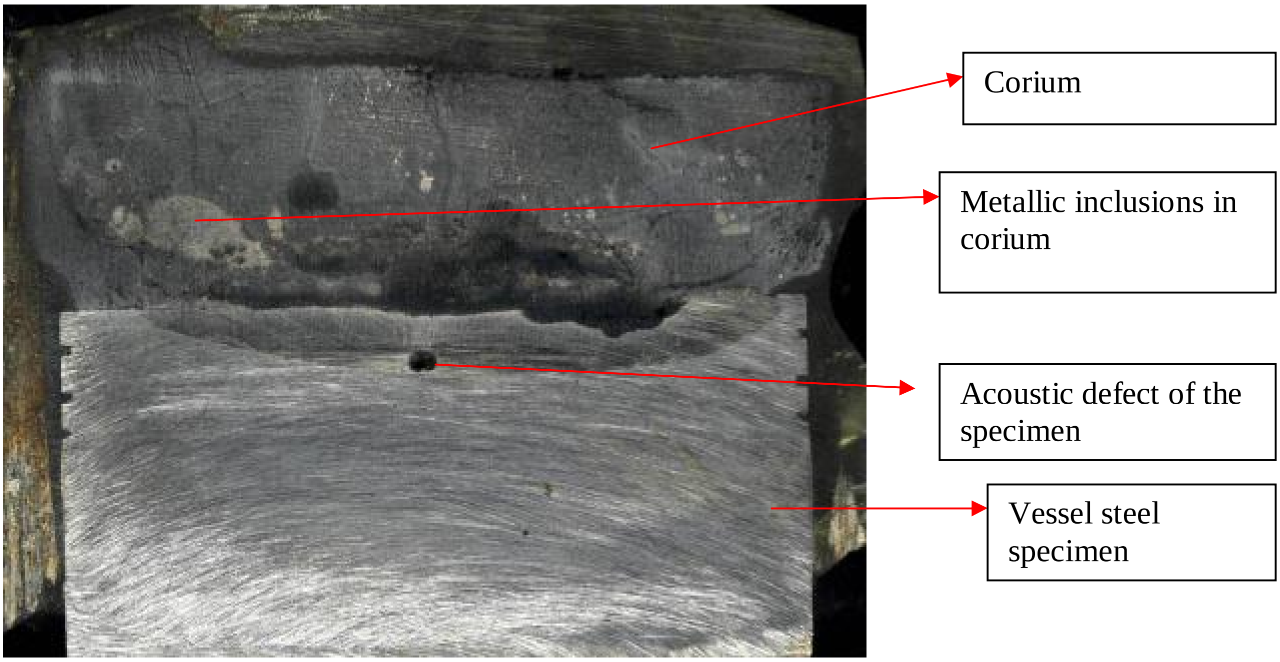

Fig.1.3.7. Longitudinal section of the specimen and corium ingot

2. Posttest analysis

2.1. Numeric modeling of the specimen temperature conditions

Similar to the MC-5 posttest analysis , in order to determine the temperature and heat flux density on the specimen top in two steady-state regimes, the specimen temperature conditions were calculated. In the calculations a finite-element program was used, which applied the solution of a stationary heat conductivity equation in an axi-symmetrical formulation. The following was set as boundary conditions:

- temperature on the internal surface of the top calorimeter (Fig. 1.1.1), which, in accordance with evaluations was 100 °C (a negligible evaluation error does not influence the calculation results);
- temperature on the internal surface of bottom calorimeter (20 °C) and
- temperature on the external surface of peripheral thermal insulation layer (Fig.1.1.1) , which was assumed to be equal to the average temperature of cooling water.

The value of heat conductivity of 15Kh2NMFA-A steel, from which the specimen was made, was borrowed from the ISTC METCOR, Phase 1 [2]. In the calculations the densities of heat flux to the specimen top were varied to achieve a best agreement between the calculated and experimental temperatures in the locations of thermocouple junctions in the specimen. At this the distribution of heat flux density along the radius was taken from the results of Pr1-MC6, and heat conductivity of peripheral heat insulating layer was assumed to be the same as in similar MC5 calculations.

The results of calculations for two steady states are presented in Fig.2.1.1, 2.1.2 and Table 2.1.1. Figs. 2.1.1 a), 2.1.2 a) experimental and calculated temperatures in the specimen at the distance of 10 and 29 mm from the specimen axis. Their comparison shows a satisfactory agreement of calculated and measured data. Figs. 2.1.1 b), 2.1.2 b) show the calculated radial distribution of temperatures on the specimen top. Fig. 2.1.1 c), 2.1.2 c) - numeric distributions of temperature in the axial section of the specimen. Table 2.1.1 shows calculated densities of heat flux to the specimen top (average and in the center, ∅ 15 mm), maximum temperature values (in the top center), and also calculated and measured power into the top calorimeter (power into the bottom calorimeter is negligibly small).

Table 2.1.1

Calculated and measured power, heat flux and temperature

Regime	Average heat flux density, MW/m^2	Heat flux density, ∅15, MW/m^2	Power into the top calorimeter, calculated kW	Power into the top calorimeter, measured kW	Maximum temperature, ^{o}C
1	0.85	1.23	1.67	1.64	1375
2	0.87	1.31	1.7	1.71	1397

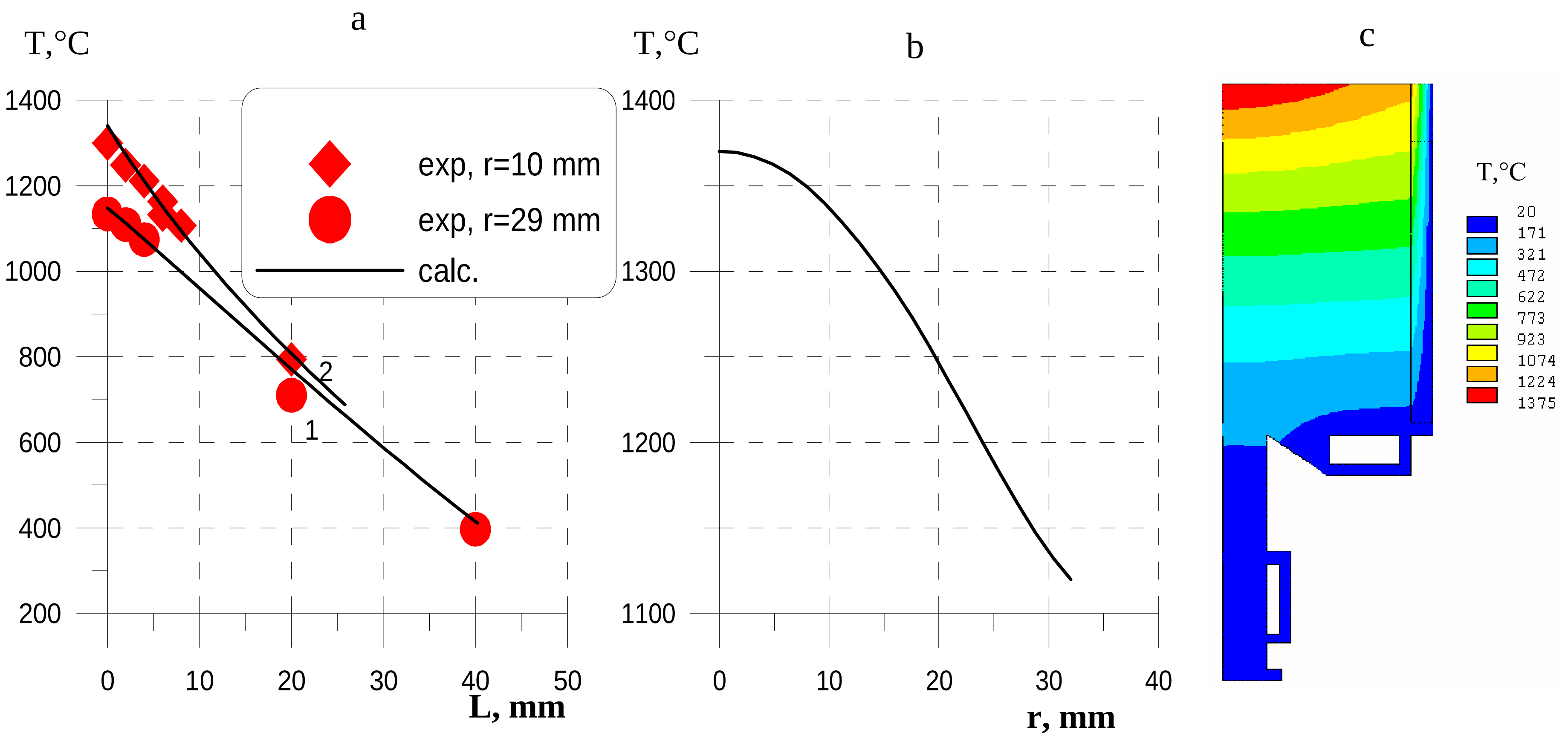

a – axial distribution of temperatures; b – radial distribution of temperatures on the specimen top; c – temperature field in the specimen (and insulation)

Fig. 2.1.1. Calculated distribution of temperature in the specimen (4000-17000 sec)

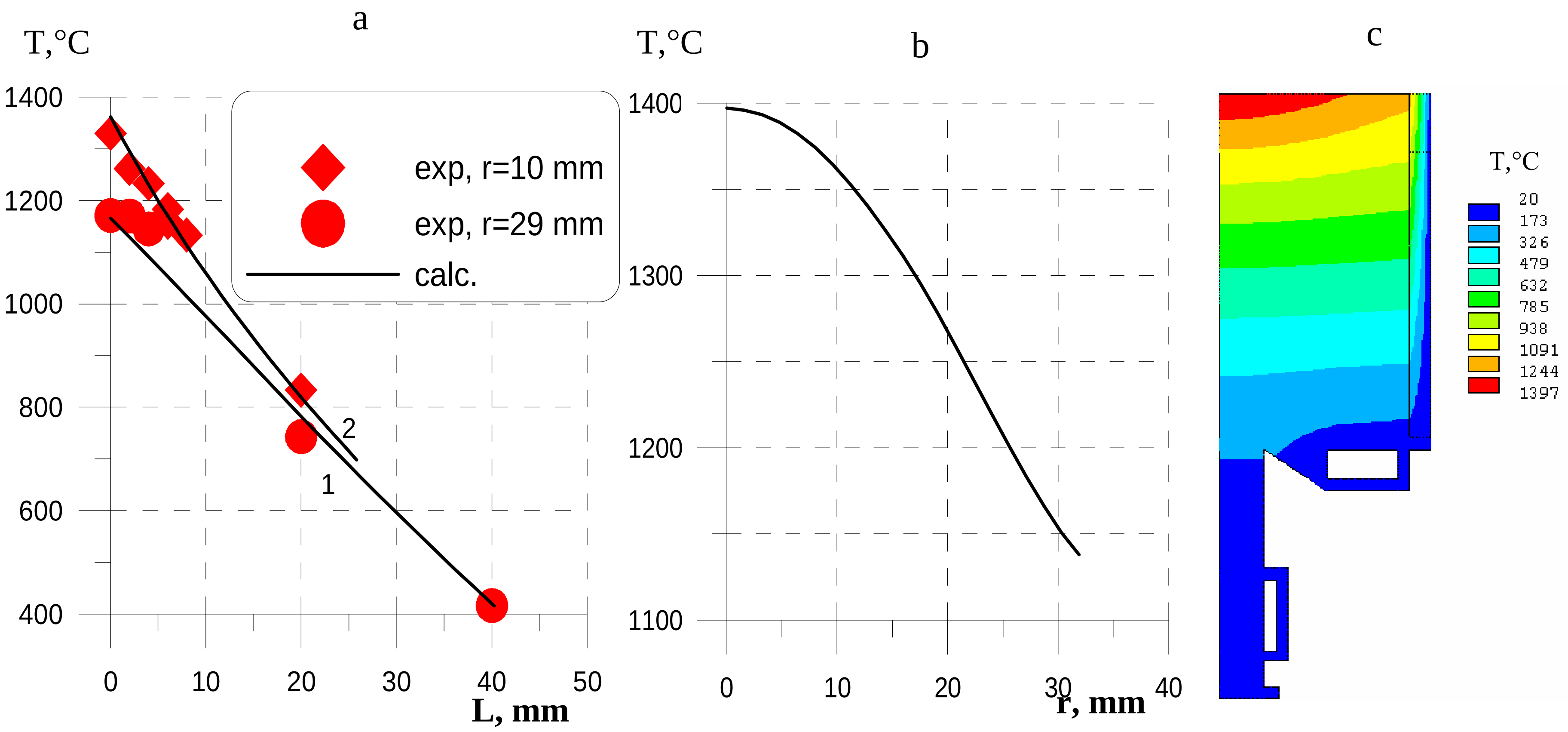

a – axial distribution of temperatures; b – radial distribution of temperatures on the specimen top; c – temperature field in the specimen (and insulation)

Fig. 2.1.2. Calculated distribution of temperature in the specimen (20000-39300 sec)

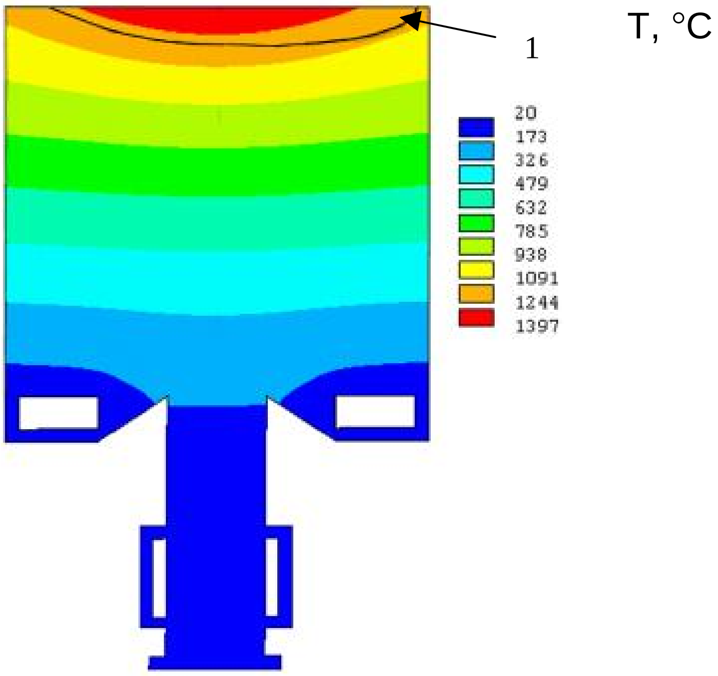

Fig. 2.1.3. Distribution of temperatures in the specimen and position of interaction boundary

Fig. 2.1.3 shows the temperature field of regime 2, the interaction boundary marked in it was determined by the posttest analysis. The asymmetric position of the boundary, uncertainty about the thermophysical properties of the material, which was formed as the result of interaction, and a possible change of hydrodynamic picture in the region adjacent to the specimen stipulate an approximate character of calculations. The resulting temperature boundary of mentioned interacted region, in accordance with Fig.2.1.3, is within 1120-1200°C.

2.2. Ultrasonic measurements of the specimen ablation rate

In MC6 the ultrasonic measurements were performed in order to determine the character of corium-steel interaction boundary progression.

The measurement methodology was described in detain in the MC5 report. In accordance with this methodology the distance between the specimen top and acoustic defect D_P is determined from distance D_m measured by the ultrasonic sensor taking into account the influence of temperature on the speed of sound in the studied material.

$$D_P = \frac{2D_m}{\left(1+b\,\frac{T_1l_2-T_2l_1}{l_2-l_1}\right)+\sqrt{\left(1+b\,\frac{T_1l_2-T_2l_1}{l_2-l_1}\right)^2+2b\,\frac{T_2-T_1}{l_2-l_1}D_m}}\,, \qquad (1)$$

where: T_1,T_2 – temperatures in the first and second measurement points located between the specimen top and acoustic defect;

l_1, l_2 – distance from the defect to the first and second temperature measurement points;

β– coefficient characterizing the influence of temperature on the speed of sound.

$$C(T) = \frac{C(0)}{1+bT(l)} \qquad (2)$$

Coefficient β is calculated at the stage of specimen heating, when the distance between the defect and top is still equal to initial D_0:

$$b = \frac{D_m - D_0}{\left(\frac{T_1 l_2 - T_2 l_1}{l_2 - l_1}\right) D_0 + \frac{T_2 - T_1}{l_2 - l_1} \times \frac{D_0^2}{2}} \qquad (3)$$

The test was conducted at the following initial values of basic parameters (Table 2.2.1).

Table 2.2.1

Initial values of relevant parameters

Parameter	Notation	Value	Meas. units	Note
Total length of the specimen	L gen	103.95	mm	
Distance between the acoustic defect and the 1st temperature measurement point	l_1	-0,043	mm	6.00 mm from the top
Distance between the acoustic defect and the 2nd temperature measurement point	l_2	3,957	mm	2.00 mm from the top
Temperature measured by thermocouple TC05 in the 1st point	T_1	variable	C^0	6.00 mm from the top
Temperature measured by thermocouple TC02 in the 2nd point	T_2	variable	C^0	2.00 mm from the top
Initial distance between the defect and top	Do	5.957	mm	
Initial speed of sound in the specimen	*C*	5.84	km/sec	

Measured value β was $1{,}9 \cdot 10^{-4}$.

Fig. 2.2.1 shows the curve of D_P change throughout the test.

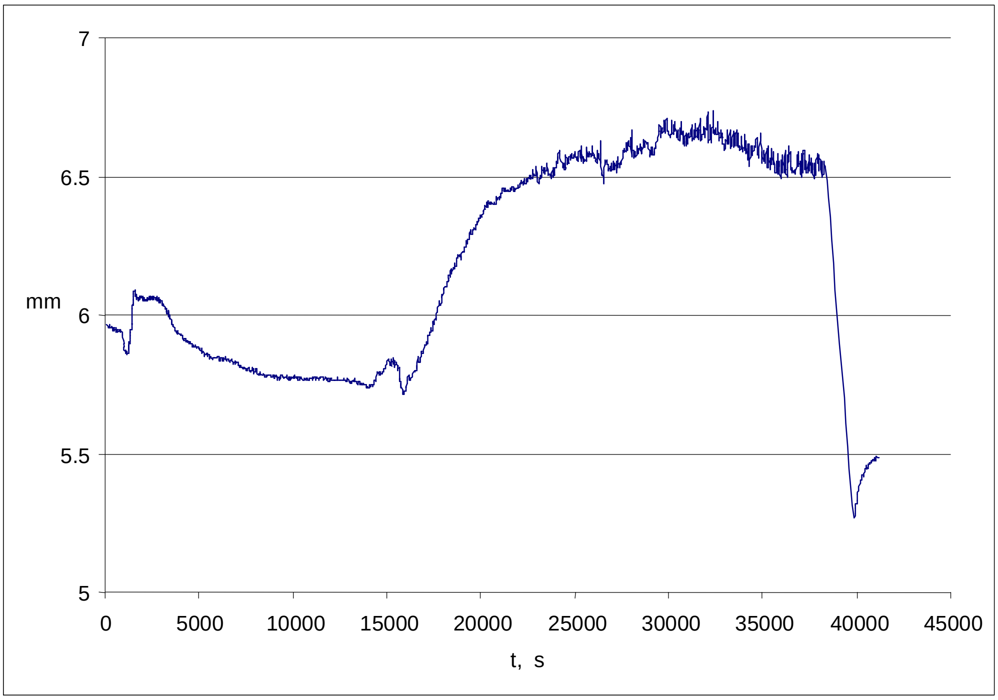

Fig. 2.2.1. D_p changes with time

As evident from Fig. 2.2.1, from the process onset and until 14960 sec a slow reduction of distance between the defect and specimen top is observed, by 0,27 mm, which testifies to the corrosion of specimen in contact with corium. A dramatic change of the value at 14960 - 15960 sec is explained by the changes in the device sensitivity, it does not reflect the real situation. Further on, starting from 15960 sec, D_p gradually increases by 0,8 mm and after 28260 sec practically stops changing. An apparent growth of D_p , probably cannot be not explained by the actual specimen lengthening, it was caused by changes in conditions of ultrasonic sound transfer.

As it was proven by the specimen posttest analyses (SEM/EDX and metallographic studies), 6 mm deeper than the top original position a region was found, which contained Fe-Zr-U; it also had a higher density than the original material. Further in the report we will refer to this region as the interaction zone. The ultrasonic measurements were performed to determine the position of interaction boundary during the test.

It can be assumed that the interaction region started to form from 15960 sec. Acoustic properties of the interaction region (density and the speed of sound), are likely to be different from those of vessel steel, which is supposed to provide in the ultrasonic signal reflection from its lower boundary.

But it is difficult to determine the position of this boundary using the single echogram of a US signal reflected from it, and the reasons are as follows:

- there is a background noise caused by interference of the main signals between the defect and specimen top;
- the amplitude of a signal reflected from the lower boundary of the interaction region is much smaller (~ 10 times) than the amplitude of a signal reflected from the top boundary of the interaction region; the first-mentioned is comparable to the background noise level;
- signal reflected from the lower boundary of the interaction region consists of several maximums and minimums, same can be said about signals from the defect and top interaction boundary. Therefore, in order to determine the location of the interaction boundary it is not enough to find, e.g., one of the maximums of a signal reflected from it, it is also necessary to attribute it to a certain maximum of a signal from the defect.

In these conditions an attempt can be made to estimate the character of the interaction front progression by changes in the ultrasonic signal from the specimen top.

The value of apparent increase D_p after 15960 sec. - h(t) can have the following formulation (Fig 2.2.2):

$$h(t) = \frac{C_T}{C_*} h_1(t) + H(t)\left(\frac{C_T}{C_*} - 1\right), \qquad (4),$$

where $h(t) = D_p(t) - D_p(15960)$,

$h_1(t)$ – actual position of the top interaction boundary in relation to D_p (15960);

$h_1(t)$ can be both positive and negative $h_1(15960) = 0$;

$H(t)$- depth of the interaction zone (position of its low boundary) vs. $D_p(15960)$, $H(15960) = 0$;

C_T, C_* - speed of sound in the solid steel specimen and in the interaction region;

$C_T > C_*$ due to a high density of the interaction region, which contains additional Zr and U.

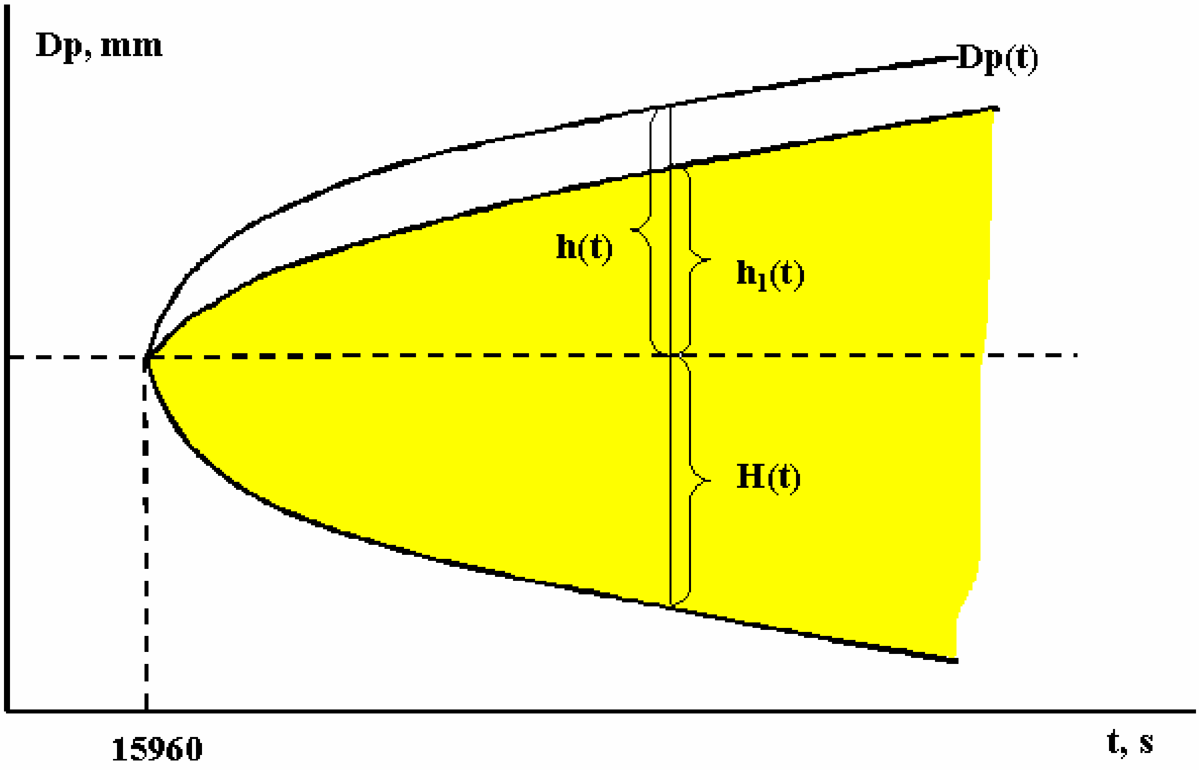

Fig 2.2.2. Scheme to illustrate expression (4)

Expression (4) correlates the apparent position of specimen top *h(t)* and depth of the interaction region *H(t).* Whereas $h_1(t)$ – actual position of the top interaction boundary – remains uncertain. If we assume that $h_1(t)$ is proportional to *H(t),* then from (4) we get that *H(t)* is proportional to *h(t).* From this follows that *H(t)* should achieve saturation as fast as *h(t).* In other words, it takes comparatively little time (by 28260 sec) for the interaction front to reach the depth, at which it is found after the test (H_{Final},) and which practically does not change afterwards.

Therefore, in a most simple approximation, when *h(t)* is in proportion to *H(t),* we get

$$H(t) = h(t)\frac{H_{Final}}{h_{Final}} , \qquad (5),$$

where $h_{Final} \approx 0{,}8$ mm (Fig.2.2.1), $H_{Final} = 5{,}73$ mm

It also follows from (4) and (5) that

$$h_1(t) = h(t)\frac{h_{1Final}}{h_{Final}} , \qquad (6)$$

where h_{1Final} – position of the top boundary of the interaction zone, which was found after the test - h_{1Final}= -0,5mm.

Fig 2.2.3 presents the approximate values *H(t)* and $h_1(t)$, which were calculated using this approach.

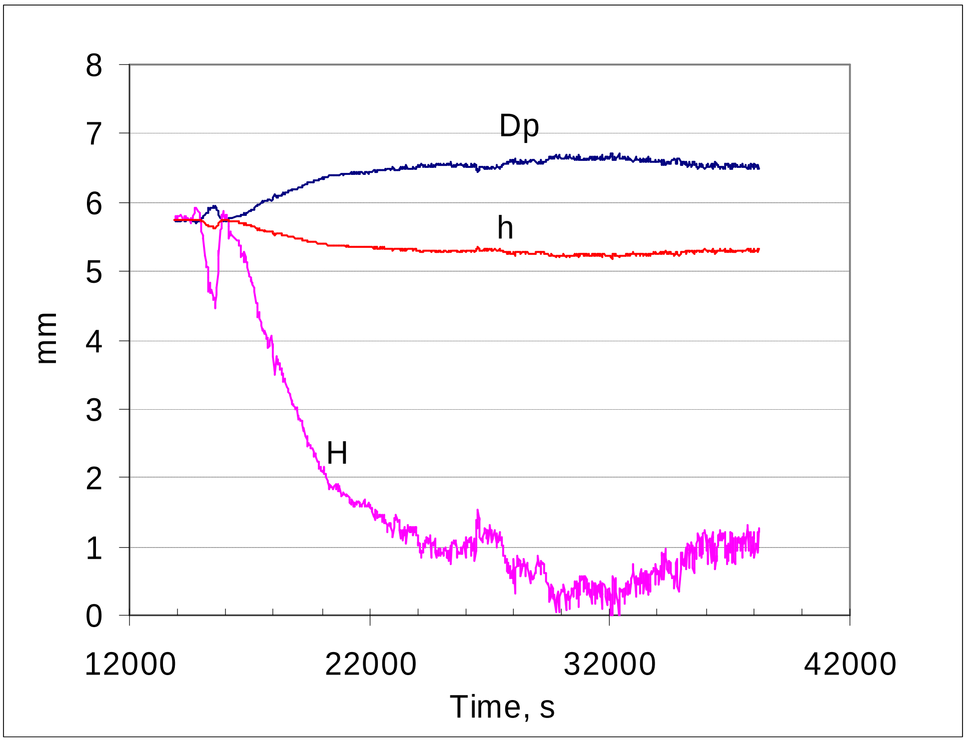

h – actual position of the top interaction boundary;
H – interaction region depth.

Fig.2.2.3. Evaluation of the interaction front progression in the course of MC6

Using (4) and values of h_{Finfl}, h_{1Final},H_{Final} we can calculate the speed of sound in the interaction region

$$C_* = C_T \frac{H_{Final} + h_{1Final}}{H_{Final} + h_{Final}} \tag{7}$$

With temperature correction C_T= 4,75km/sec. Therefore C_*= 3,8 km/sec.

Let's compare these evaluations of the interaction region position with the ultrasonic measurement data. As it has been mentioned, the data of a single echogram can hardly be used for determining the position of a signal reflected from the bottomline boundary of interaction region.

Let us analyze changes in the ultrasonic signal interference picture of the test using the echogram field.

For this we consider the function of two variables A(t,τ), where A – magnitude of US signal in relative units, t – test running time in seconds, τ – echogram scanning time in microseconds. At an optional t_1, A(t_1,τ) is an echogram recorded at a moment of time t_1. An echogram example is given in Fig. 2.2.4.

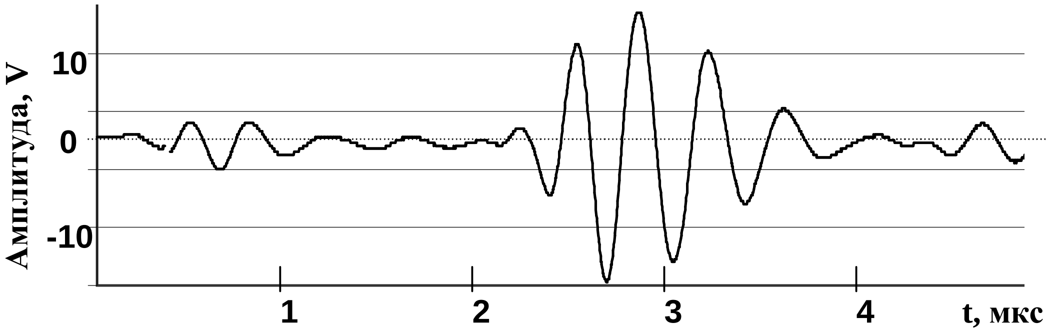

Fig 2.2.4. Example of an echogram

Fig 2.2.5 shows the 3D image of echogram surface A(t,*t*).

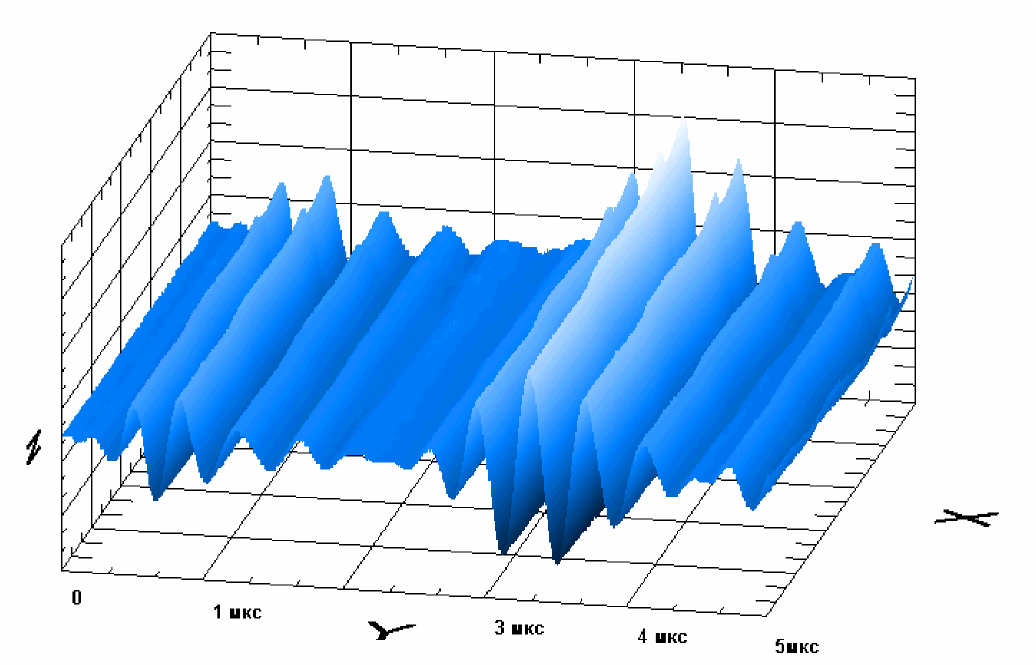

Fig. 2.2.5. An example of the echogram surface

Test time *t* is marked on axis X (Fig.2.2.5). Echogram scanning time τ is marked on axis Y. Amplitude of echogram signals is marked on axis Z. The colorscheme reflects the amplitude values. White color corresponds to the maximum positive value A; black – to the maximum negative value; different shades of blue reflect intermediate states.

We define the echogram field as the projection of color surface on plane (t,τ).

In order to construct the echogram field the position of echograms was modified in relation to the single time point, which was chosen in the beginning of the test from the central peak of the signal reflected from the defect. The horizontal line in the echogram bottom part shows the position of this central peak maximum.

In order to get a clearer interference picture of the process, the cross section of the echogram field was used. It differs from the original echogram field by color scheme parameters – white at A>3,0 and black at A< -10, Fig.2.2.6..

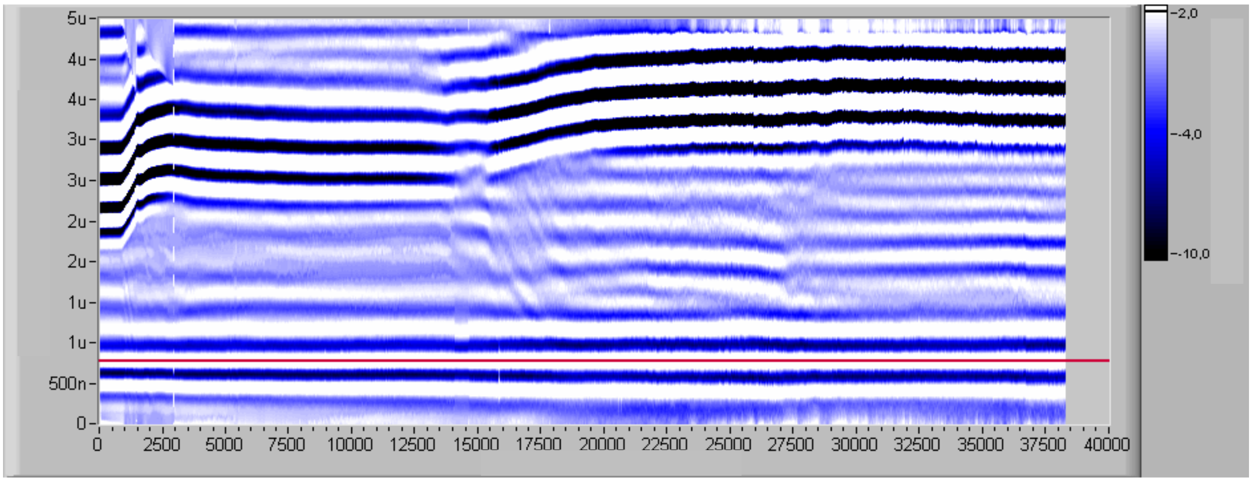

Fig. 2.2.6. Dynamics of cross section of the echogram field (whole test without the cooling stage) on the amplitude levels from +3,0 to -10 relative units

Further treatment of the echogram field is performed by subtraction. I.e., we take [A(t,τ)-A(t-Δt,τ)] instead of A(t,τ), Δt = 1500 sec. The result if this treatment is presented in Fig. 2.2.7. This figure also shows the position of the top interaction boundary calculated from (5). Fig. 2.2.7 demonstrates the disturbances of interference picture, they propagate from the specimen top to the defect; they should be interpreted as the US signals reflected from the low interaction boundary. The position of these signals matches the evaluation based on (5).

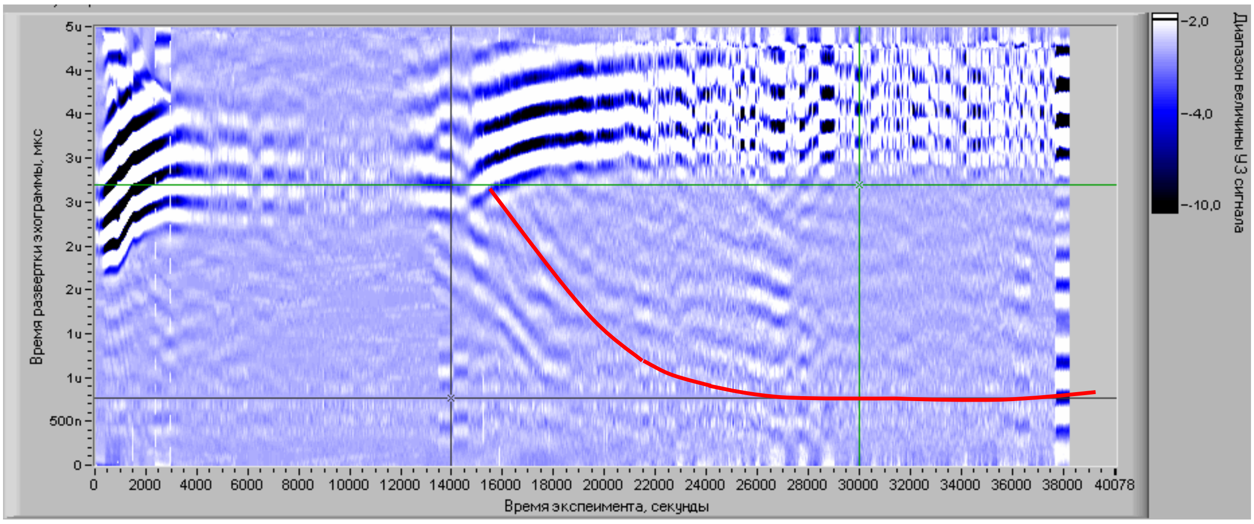

Fig. 2.2.7. Dynamics of cross section of the echogram field after the method of subtraction was applied

In conclusion the following must be noted:

- Corrosion was observed at the early stages of the test. Its rate was determined, in the period t 2460-4460 sec it was $7,6\times10^{-5}$ mm/sec, and in the period t 4460-13460 sec - 1×10^{-5} mm/sec;

- Starting from 15960 sec of the test the ultrasonic measurements indicate the establishment and progression of the interaction zone, its composition and rheology is discussed in the next section of the report.

- The zone started to establish itself in 5 hours after the test start.

- Progression of the interaction zone into the bulk of the specimen has a tendency to slow down, and its final position is confined by the isotherm of 1100 – 1200 ºC.

2.3. Physico-chemical analysis

2.3.1. Material balance of the test

In order to make the material balance of MC6 the input charge components and melting products were analyzed for the content of basic components and weighed with accuracy up to 0.1 g.

In a separate pretest Pr1-MC6 corium was molten, a part of it, 150 g, was used to simulate a crust on the steel specimen, such crust is produced when a suboxidized melt attacks reactor vessel under severe accident conditions. The ingot of corium produced in Pr1-MC6 was ground, and an average sample was prepared from it by quartering. Table 2.3.1 presents the results of physico-chemical analysis of this sample.

Table 2.3.1

Results of the physico-chemical analysis of the Pr1-MC6 average sample

Detection method	XRF			Gas-volumometric	Oxidation degree, C
Element	U	Zr	Admixtures and O*	Zr^0	
Average sample of the ingot, mass.%	67.3	21.6	11.1	16.0	27.0

*- from the residue.

Material balance of components in MC6 is given in Table 2.3.2.

Table 2.3.2

MC 6 material balance

Introduced into the melt, g		Collected after the test, g	
Corium C-27.0 (76.4 mass.%UO_2, 7.9 mass.% ZrO_2, 15.7 mass.% Zr)	150.0	Sample	8.9
UO_2	1292.0	Ingot and steel specimen*	3206±10
ZrO_2	158.6	Aerosols	6.8
Zr metallic	249.4	Spillages	44.3
Steel specimen	1712.7		
Σ	3562.7	Σ	3563±10

*) the specimen and corium ingot were embedded in epoxy immediately after the test, for this reason the ingot mass was determined from the residue of the whole charge mass.

2.3.2. X-ray fluorescence (XRF) of the witness specimen and melting products

The elemental composition of the witness-specimen and melting products was determined by the XRF method using the SPARK-1M/IBM PC spectrometer [3].

Similar to MC5, the witness steel specimen, having the shape of a 40 mm diameter disc, was lathed from a cylindrical block and subjected to the XRF analysis.

Table 2.3.3 presents the XRF data of the witness specimen and its comparison to the requirements of the Standard Specifications (TU, Russian acronym) of this vessel steel brand.

Table 2.3.3

XRF data of the 15Kh2NMFA-A steel witness specimen

TU, method of analysis	Chemical elements, % mass.											
	C	Si	Mn	Cr	Ni	Mo	V	P	S	Cu	Co	As
TU 108-765-78	0.13-0.18	0.17-0.37	0.30-0.60	1.8-2.3	1.0-1.5	0.5-0.7	0.10-0.12	<0.02	<0.02	<0.3	<0.03	<0.003
XRF	-	0.25	0.49	2.24	1.00	0.70	0.10	<0.02	-	0.07	<0.03	<0.003

The XRF data testify to the full compliance of steel used in the tests with TU 108-765-78 requirements.

After the test the corium ingot and steel specimen were embedded in epoxy and cut along the axis. A half of the corium ingot was cut again to produce the average samples of top and bottom parts, which were subjected to analyses.

The average samples of top and bottom ingot parts were prepared by quartering and crushed until the particles were ≤ 50 μm.

Table 2.3.4 presents the XRF data of molten products.

Table 2.3.4

XRF data of the top and bottom parts of corium ingot

Sample	Content, mass.%				Note
	U	Zr	Fe	O***	
Average corium sample (ingot top)*	61.5	21.4	0.5	16.6	
Average corium sample (ingot bottom)*	60.5	20.6	1.5	17.4	
Average corium sample (ingot top)**	59.2	20.9	0.4	19.2	0.3% Nb
Average corium sample (ingot bottom) (powder <50 μm)**	58.4	20.5	1.4	19.1	0.6% Nb

*) Sample from the solution in concentrated acids

**) Sample as a powder tablet.

***) O and admixtures from the residue.

2.3.3. Chemical analysis of melting products

Average samples of the ingot top and bottom were analyzed for U^{+4}, U^{+6} content.

The methodology of U^{+4}, U^{+6} determination is used for measuring microquantities of uranium in corium samples. Its sensitivity is 0.04 μg/ml. The method is based on a phenomenon that tetravalent uranium forms colored compounds with arsenazo III reagent in 4 N HCl. For the reduction of uranium the granulated zinc in presence of ascorbic acid is used. At the interaction with arsenazo III, the tetravalent uranium forms a green complex; if the reagent is in excess, a multi-shade violet coloring is observed. The spectrophotometry gives best results at the 2-5-fold molar excess of the reagent. The coloring appears immediately and stays stable at least for 2 hours. The method enables to determine separately the content of tetravalent uranium and full inventory of uranium in the solution. The content of hexavalent uranium is calculated from the difference between uranium (IV) and full uranium inventory.

The volumometric method [4] was used for determining free zirconium in corium samples. The method is based on measuring hydrogen release at the interaction of metallic zirconium, which is present in corium, with concentrated phosphoric acid. The reaction of interaction between metallic zirconium and concentrated phosphoric acid was analyzed in the following way:

(dissolution of free zirconium in phosphoric acid accompanied by the generation of two moles of hydrogen per each gram-atom of zirconium)

$$Zr + 4H_3PO_4 = Zr(H_2PO_4)_4 + 2H_2\uparrow. \qquad (1)$$

Calculation of free zirconium from the volume of released hydrogen was made using:

$$Zr_{св} = \frac{91,22 \cdot 273,15}{2 \cdot 22,416 \cdot 760} \cdot \left(\frac{V_2 \cdot P_2}{273,15 + t_2} - \frac{V_1 \cdot P_1}{273,15 + t_1} \right) \qquad (2)$$

where

91,22 –Zr atomic weight

273,15 – absolute temperature of water freezing, К;

2241,60 – volume of one mole of hydrogen gas under temperature 273,15 К and 760 mm mercury column, l.

V_2 and V_1 – volumes of gas measured after and before the tested mixture dissolution, ml.

P_2 and P_1 - atmospheric pressure after and before the tested mixture dissolution, mm merc. col.

t_2 and t_1 – ambient air temperature measured after and before the tested mixture dissolution, ^oC.

The determination of free and total Zr enables to evaluate the zirconium oxidation degree (C_n) from:

$$C_n = (Zr_{total} - Zr_{free.}) / Zr_{total} * 100\%, \qquad (3)$$

The content of metallic iron, Fe^0, was determined by the copper-sulphate method [5].

Table 2.3.5 presents the results of chemical analysis of the top and bottom parts of corium ingot.

Table 2.3.5

Chemical analysis of top and bottom parts of corium ingot

Method	Photocolorimetry (dissolution in H_2SO_4 and $H_3PO_{4)}$		Volumometric method	Copper-sulphate method
Sample	U^{+4}	U^{+6}	Zr^0	Fe^0
	mass.%			
Average corium sample (ingot top)	63.7±0.3	-	14.7±0.1	0.08
Average corium sample (ingot bottom)	62.5±0.4	-	17.8±0.4	0.09

Table 2.3.6 gives the analysis errors

Table 2.3.6

Analysis errors

Element	Error % relative	Method
U	5*, 10**	XRF
Zr	5*, 10**	XRF
Fe	5*, 10**	XRF
U^{+4}	3	Photocolorimetry
Zr^0	10	Volumometric
Fe^0	10	Copper-sulphate

*- at the analysis of a powder sample.

**- at the analysis of a liquid sample (solution).

2.3.4. Density of molten corium

The picnometric density of molten corium was determined for the average sample, which was prepared by quartering [6,7]. Distilled water was used as a picnometric liquid. The evaluation of density under normal conditions is presented in Table 2.3.7.

Table 2.3.7

Picnometric density of molten corium

Sample	Molten corium particles, µm	Picnometric density, g/cm^3
Average corium sample (ingot top)	100-200	8.78
Average corium sample (ingot bottom)	100-200	8.52

The density evaluation error was ± 0.02 g/cm^3.

Physico-chemical analysis, which included material balance and evaluation of elemental composition, has shown the following:

- Material balance: losses of relevant components were negligibly small.

-XRF and chemical analysis: when corium interacts with steel specimen at 1300^{o}C, some steel components migrate into molten corium (tables 2.3.4 and 2.3.5). Most of them stay in the ingot bottom part, so content of uranium and corium density in the ingot top is slightly higher than in the bottom part.

2.4. SEM/EDX analysis of corium and steel

The microstructure and elemental composition of samples were determined using the methods of scanning electron microscopy (SEM) and energy dispersion X-ray (EDX).

For SEM studies the scanning electron microscope CamScan MV2300 was used. The elemental analysis of chosen parts was made using microprobe device Oxford Link.

The spectral characteristics of each sample were taken, it was used for determining its integral composition and the composition of each separate fraction. The qualitative analysis was made by comparing the spectral intensities of the reference (highly pure, specially prepared substances) and studied samples. The reference samples of U, Zr, Cr, Fe, Si, Ca, Ni, O were taken from the accessories kit of the Link microprobe.

The limit of reliable determination of an element depends on its number in the Mendeleev Periodical table of elements, and it varies from 0.1 mass % for light elements to 0.3 mass% for heavy ones. The determination of elements found in smaller quantities is unreliable.

2.4.1. SEM/EDX-analysis of Pr1-MC6 corium

In order to determine the microstructure of molten corium (Pr1-MC), used for the crust simulation in MC6, a template was prepared.

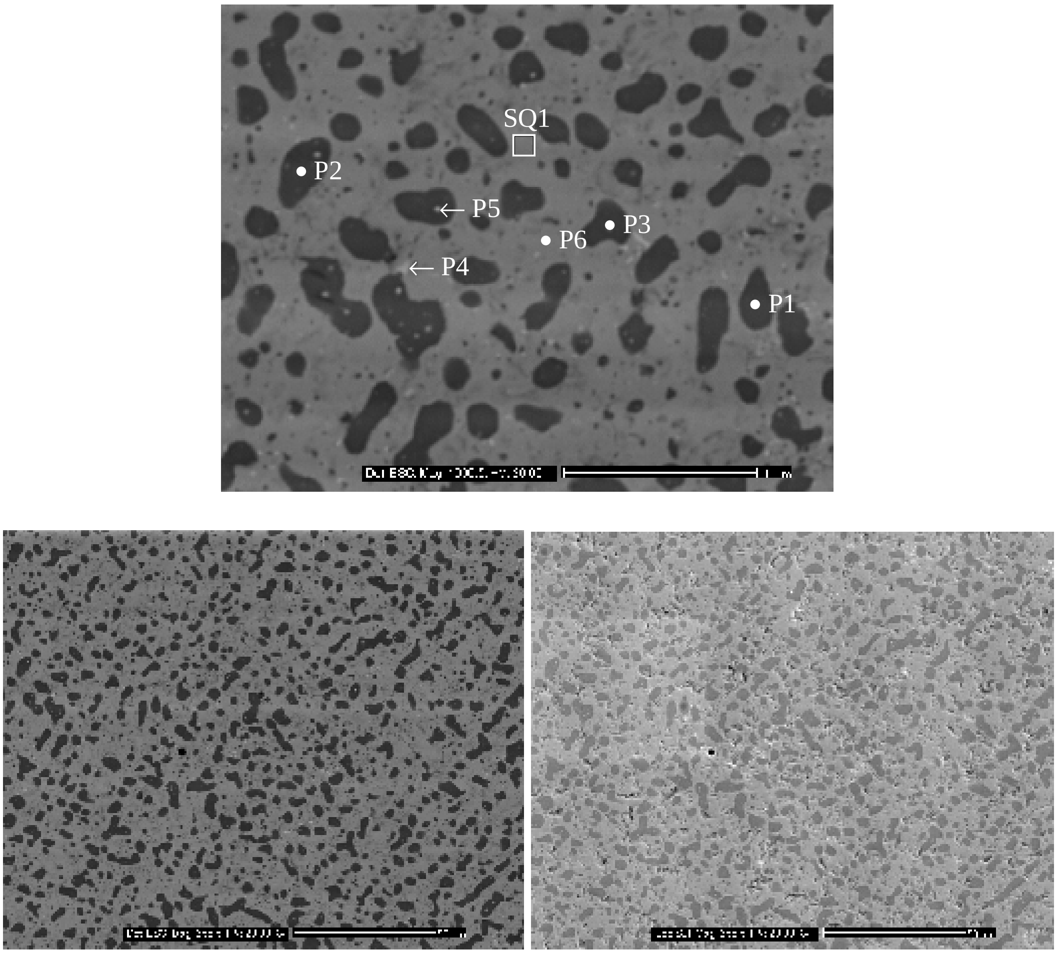

(SQ2) chemical; composition

(SQ2) relief

Fig. 2.4.1. Microphotograph of the Pr1-MC6 template

Table 2.4.1

EDX-analysis

№		U	Zr	O	Nb	Comments
P1	mass.%	2.52	90.97	6.51	-	α-Zr(U,O)
	mol.%	0.75	70.49	28.76	-	
P2	mass.%	3.55	89.83	6.62	-	
	mol.%	1.05	69.66	29.29	-	
P3	mass.%	2.07	91.27	6.66	-	
	mol.%	0.61	70.18	29.21	-	
P4	mass.%	84.83	4.05	6.70	4.42	U(Zr,Nb)O
	mol.%	41.09	5.12	48.30	5.49	

P5	mass.%	59.09	34.45	6.46	-	U(Zr)O + α-Zr(U,O)
	mol.%	24.11	36.67	39.23	-	
P6	mass.%	80.95	4.07	14.98	-	$U(Zr)O_2$
	mol.%	25.74	3.37	70.88	-	
SQ1	mass.%	80.39	4.29	15.31	-	
	mol.%	25.17	3.51	71.32	-	
SQ2	mass.%	58.80	28.30	12.90	-	Total composition
	mol.%	18.12	22.75	59.13	-	

SEM/EDX analysis of the template is given in Fig. 2.4.1 and Table 2.4.1. After crystallization the suboxidized corium features three types of phases:

- α-Zr-based, containing a certain amount of uranium (points P1, P2, P3);
- α-Zr-based, enriched with uranium (point P5)
- and a UO_2-based phase, which contains a certain amount of ZrO_2 (point P6 and area SQ1)

It also has also a certain amount of solid solution based on uranium monoxide, which contains a certain amount of zirconium monoxide and niobium oxide (point P4). The total composition approximately corresponds to the predetermined corium stoichiometry (area SQ2). The recalculation of UO_2-ZrO_2-Zr for area SQ2 gives corium index – 50.308, which can be explained by the oxidation of the polished section prepared for the SEM/EDX analysis.

2.4.2. SEM/EDX-analysis of MC6 templates

Corium microstructure and elemental composition, corium-steel interaction boundary, as well as the elemental composition of the MC6 steel specimen were determined using three templates (template №1 Fig. 2.4.2, template №2 Fig. 2.4.9 and template №3 Fig. 2.4.23). The figures (Figs. 2.4.3-2.4.8, 2.4.10-2.4.22, 2.4.24-2.4.29) and corresponding tables (2.4.2-2.4.6, 2.4.7-2.4.17, 2.4.18-2.4.19) present the microstructure and elemental composition of regions chosen for examination.

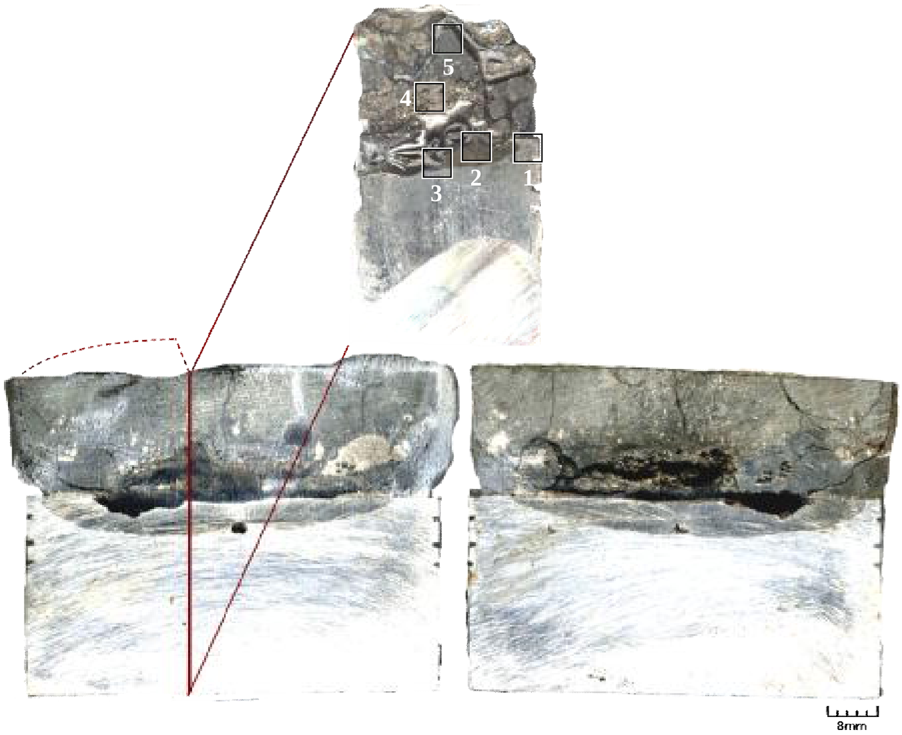

Fig. 2.4.2. MC6 ingot cross section and schematics of template №1 cutting with marked regions

SEM/EDX analysis of corium-steel interaction boundary, which was conducted from periphery to the center (template №1, Fig. 2.4.2), showed the presence of a certain zone between corium and steel. The zone had a dendrite type of iron crystallization, regions between the dendrites were iron-based and looked typical of the eutectic crystallization of the melt. This proves that this zone was in molten state during the test (regions 1, 2 and 3 in Figs. 2.4.2, 2.4.3, 2.4.4 and 2.4.5).

The examined interaction region was crystallized from the melt enriched with uranium, zirconium and oxygen; the crystallization had a dendrite character (region 1-1, Fig. 2.4.3, Table 2.4.2, area SQ2). After the crystallization it comprised three phases: 1) iron-based, containing a certain amount of Cr and admixtures of Mg, N, Si (Fig. 2.4.3, region 1-1-1; Table 2.4.2, point P1); 2) (U,Zr)Fe_2-based compounds with admixtures of Cr, N, Mg and Si (Fig. 2.4.3, region 1-1-1; Table 2.4.2, point P2); 3) UO_2-ZrO_2 –based solid solution (Fig. 2.4.3, region 1-1-1; Table 2.4.2, point P3).

The total composition of steel near the crystallized U-Zr-Fe-O melt does not differ much from the initial composition of steel (Fig. 2.4.3; cf. Table 2.4.2. – area SQ1 and Table 2.3.3 - XRF of steel initial composition). The steel had several pores near the melt ingot. These pores can be explained either by the recrystallization, which resulted in the pore size increase, or by the carbon oxidation in the inter-crystal space by the oxygen, which diffused into steel.

It should be noted, that in accordance with the data of SEM/EDX analysis a certain difference is observed in the crystallized melt microstructure and composition on the ingot periphery (Fig. 2.4.3 – region 1-1, Table 2.4.2 – area SQ2) and on the steel – corium boundary(Fig. 2.4.4 – region 2-1 SQ1, Table 2.4.3 – area SQ1). The mentioned differences are likely to be explained by different crystallization conditions of the melt after the induction heating was disconnected.

Molten corium and interaction zone in this template (template №1, Fig. 2.4.2) were separated by large pores of a typical ~3 mm size, which appeared during the melt crystallization.

In region 3 the interaction zone broke off from steel, it probably happened when the template was prepared for analyses (Fig. 2.4.5).

Region 4 (Fig. 2.4.6) is the oxygen-enriched crystallized U-Zr-Fe-O melt present near the interaction zone. It can be considered as the melt of initial corium, which incorporated the iron-containing component when contacting the melt, which formed in the corium-steel interaction zone (Table 2.4.4, area SQ1). The presence of pores in the bottom part proves the release of oxygen during the melt crystallization.

Region 5 (Fig. 2.4.7) –UO_2-ZrO_2-FeO melt (Table 2.4.5, area SQ1), in composition it is close to the initial oxidic melt (U:Zr ratio, Fig. 2.4.8, Table 7, SQ1 – melt sample), but enriched with the iron component.

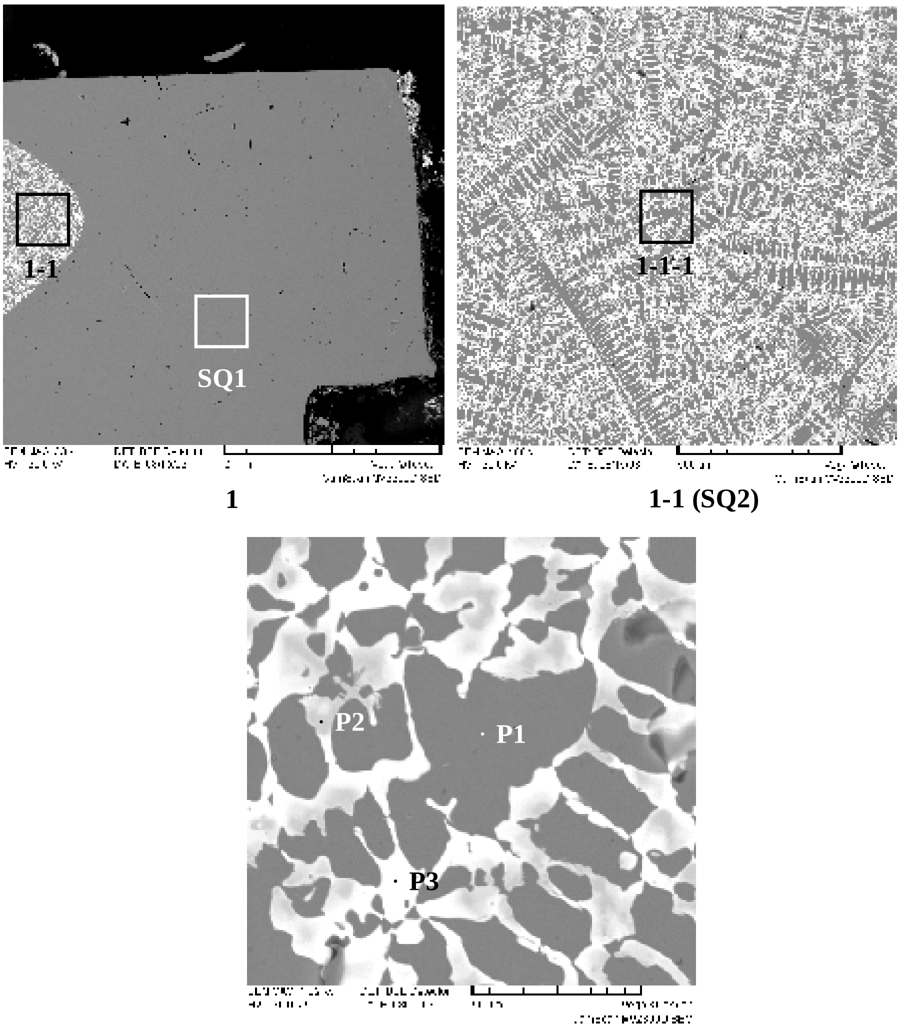

1 1-1 (SQ2)

1-1-1

Fig. 2.4.3. Microphotographs of Region 1

Table 2.4.2

EDX-analysis of the specimen

№		Fe	Cr	Ni	Mn	Si	Comments
SQ1	mass.%	95.6	2.4	1.3	0.3	0.4	Total composition of steel
	mol.%	95.2	2.6	1.2	0.3	0.7	
P1	mass.%	93.9	4.2	0.4	1.2	0.3	Iron-based region of crystallized Fe-U-Zr-O melt
	mol.%	93.4	4.5	0.4	1.2	0.5	

№		U	Zr	Fe	Cr	Ni	Mn	Si	O	Comments
SQ2	mass.%	25.6	4.8	58.3	2.3	0.7	0.5	0.3	7.5	U-Zr-Fe(Cr,Ni,Mn,Si)-O melt
	mol.%	6.1	3.0	56.7	2.5	0.7	0.5	0.6	26.8	

№		U	Zr	Fe	Cr	Ni	Mn	Si	Comments
P2	mass.%	36.6	19.6	41.3	0.7	0.7	0.4	0.6	(U,Zr)Fe_2-based phase
	mol.%	13.2	18.5	63.6	1.2	1.0	0.6	1.8	

№		UO_2	ZrO_2	Comments
P3	mass.%	95.4	4.6	(U,Zr)O_2-based phase
	mol.%	90.5	9.5	

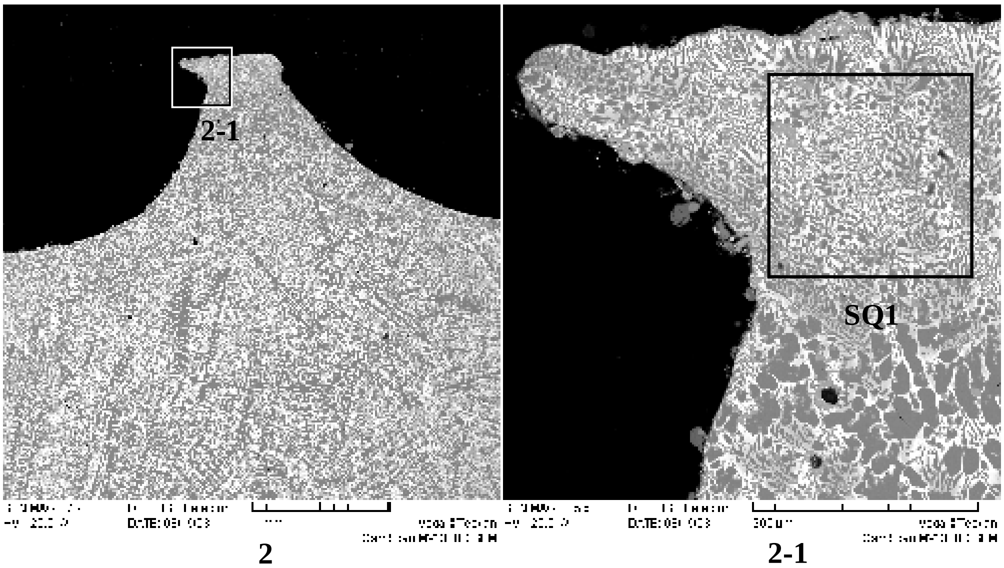

2 2-1

Fig. 2.4.4. Microphotographs of region 2

Table 2.4.3

EDX-analysis of the specimen

№		U	Zr	Fe	Cr	Ni	Mn	Si	O	Comments
SQ1	mass.%	25.7	24.2	47.2	1.6	0.6	0.6	0.2	-	U-Zr-Fe(Cr,Ni,Mn,Si,O) melt
	mol.%	8.4	20.8	66.2	2.3	0.8	0.9	0.6	-	

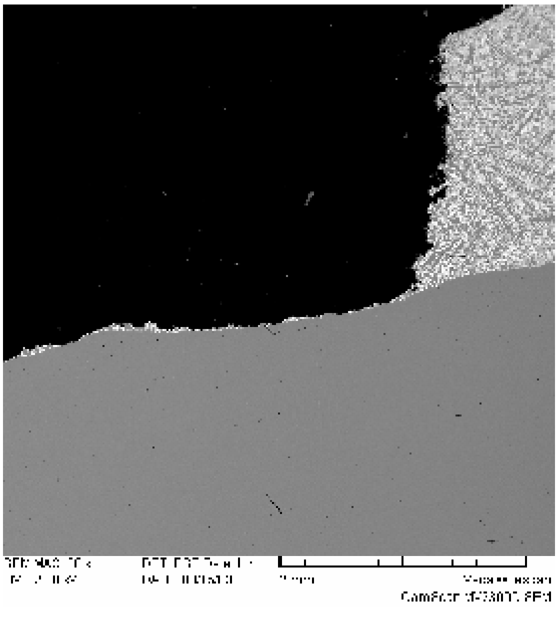

Fig. 2.4.5. Microphotographs of region 3

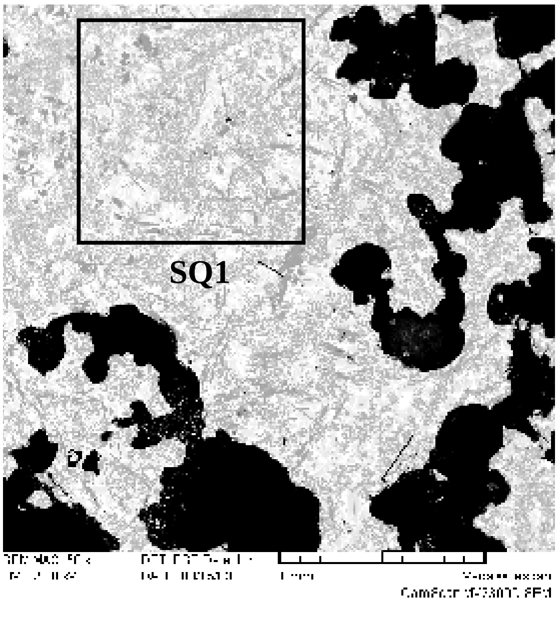

Fig. 2.4.6. Microphotographs of region 4

Table 2.4.4

EDX-analysis of the specimen

№		U	Zr	Fe	O	Comments
SQ1	mass.%	48.3	28.0	13.0	10.7	Molten corium C-32 with FeO
	mol.%	14.4	21.8	16.5	47.4	

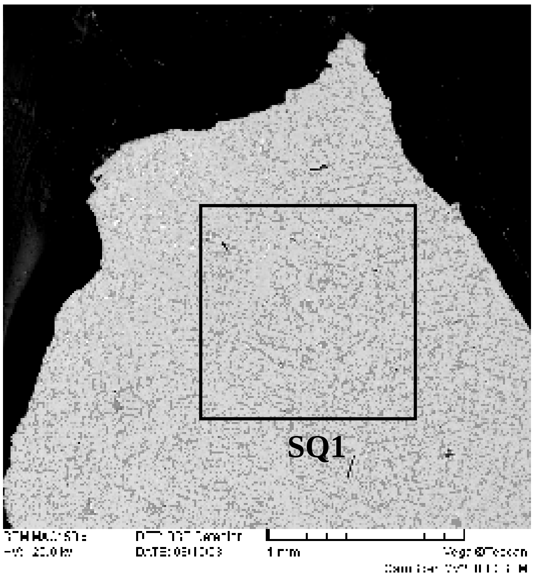

Fig. 2.4.7. Микрофотографии области 5

Table 2.4.5

EDX- analysis of the specimen

№		U	Zr	Fe	O	Comments
SQ1	mass.%	53.9	23.7	0.7	21.6	Molten corium C-97 with FeO
	mol.%	12.2	14.1	17.1	73.0	

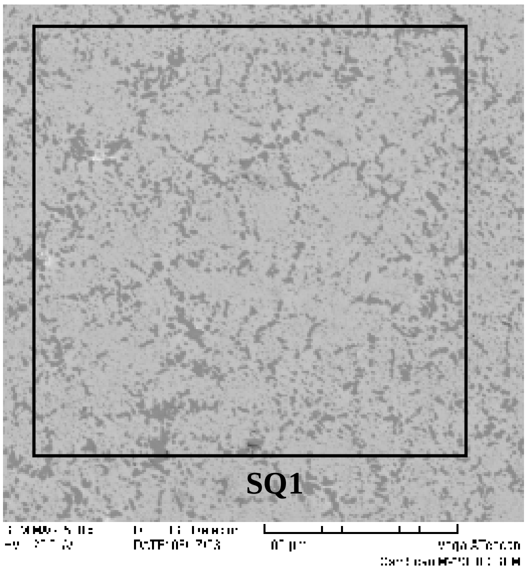

Fig. 2.4.8. Microphotographs of corium sample taken during the test

Table 2.4.6

EDX- analysis of the specimen

№		U	Zr	Fe	O
SQ1	mass.%	56.6	24.1	0.2	19.1
	mol.%	13.9	15.5	0.2	70.3

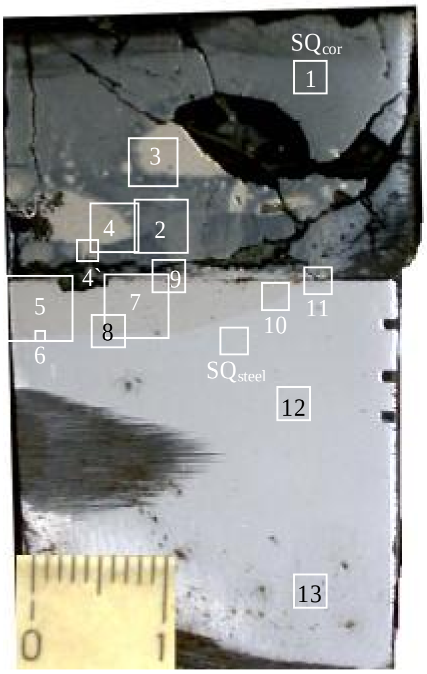

Fig. 2.4.9 MC6 template №2 with regions marked for examination

A more detailed SEM/EDX analysis of the crystallized corium –interaction zone – vessel steel structure was made using template №2 (template №2 with regions marked for examination, Fig. 2.4.9).

The crystallized corium beyond the interaction zone (Fig. 2.4.9, region 1), corium near the interaction zone (Fig. 2.4.9, region 2) and metallic inclusions into it (Fig. 2.4.9, regions 3, 4 and 4’) have been studied.

The analysis of total composition of non-interaction zone corium shows, that iron and thorium components are present in it in the trace-like quantities (Fig. 2.4.9 and 2.4.10, region 1, Table 2.4.7, areas SQ_{Cor} and SQ_2). The post-crystallization corium consists of two phases: solid solution $U(Zr)O_2$ and α-Zr-based phase containing a certain amount of uranium and iron.

The examination of corium near the interaction zone showed two typical crystallization patterns (region 2 in Figs. 2.4.9 and 2.4.11): crystallization of solid solution $U(Zr)O_2$ shifted in the direction of UO_2 (Fig. 2.4.11, Table 2.4.8 – area SQ1); and two-phase crystallization having a α-Zr-based phase enriched with iron (Fig. 2.4.11, Table 2.4.8 – area SQ2).

The analysis of drop-like inclusions showed that before the crystallization they existed as a U-Zr-Fe-O melt and that they were very close to each other in composition and microstructure (regions 3, 4 and 4’ in Figs. 2.4.9, 2.4.12 and 2.4.13, Table 2.4.9 – area SQ1 and SQ1’, and Table 2.4.10 – areas SQ1 and SQ1’). Around the drop-like inclusions corium did not crystallize uniformly (similar to region 2, Figs. 2.4.9 and 2.4.11). The drop-like inclusions have indistinct boundaries. They are surrounded by solid solution $U(Zr)O_2$, closer to the phase boundary there is a α-Zr –based phase concentration (regions 3, 3-1 in Fig. 2.4.12 and region 4 in Fig. 2.4.13). The microstructure of crystallized droplet inclusions has at least eight phases: 1) U monoxide-based phase with a small content of iron and zirconium, also thorium in microquantities (region 3-2-1 in Fig. 2.4.12, Table 2.4.9 - point P1); 2) –Zr-Fe-U-O-based phase with a small amount of thorium (region 3-2-1 in Fig. 2.4.12, Table 2.4.9 - point P2); 3) – a phase similar to the previous, but enriched with zirconium (region 3-2-1 in Fig. 2.4.12, Table 2.4.9 - point P3); 4) –phase, which was probably formed at the dissociation of U and Zr-based solid solution (from uranium side) and mostly containing iron, zirconium, uranium and oxygen with a small content of chrome (region 3-2-1 in Fig. 2.4.12, Table 2.4.9 - point P4); 5) – phase, in composition close to the previous, but slightly enriched with iron, zirconium and chrome (region 3-2-1 in Fig. 2.4.12, Table 2.4.9 - point P5); 6) – phase, in composition close to the previous, but to a higher extent enriched with iron and chrome and having depleted uranium (region 3-2-3 in Fig. 2.4.12, Table

2.4.9 - point P9); 7) – phase in the crystallization character close to α-Zr crystals (Fig. 2.4.12 and Table 2.4.9; due to a too fine size it was not possible to determine its composition precisely and point P6 – region 3.2.1 includes captured phase P2, a point P7 - region 3.2.3 includes captured phase P4); 8) – the most “metallized”, Fe and Zr-based phase containing uranium and chrome in small quantities (more chrome than in other phases) (region 3-2-3 in Fig. 2.4.12, Table 2.4.9 - point P9).

Along with that, the drop-like inclusions have parts, which in morphology are similar to corium-bordering regions, and their composition is similar to corium in region 2 (Fig. 2.4.11., Table 2.4.8 – area SQ2), but it is enriched with iron and oxygen in it is depleted.

It should be noted, that in spite of the similar composition of both drop-like inclusions studied, their crystallization picture is slightly different. The drop-like inclusion, which is located farther from the interaction region (region 3 in Fig. 2.4.12), as compared to the inclusion adjacent to the interaction zone (region 4 in Fig. 2.4.13), has more dendrite-like structures, and this can be explained by a different thermal history. In the drop-like inclusion above the interaction zone (region 4 in Fig. 2.4.13) the structures similar to the boundary ones prevail (Fig. 2.4.11., Table 2.4.8 – area SQ2, also Fig. 2.4.13). It is also interesting to find a “channel” connecting the interaction zone with the drop-like inclusion (region 4’ in Fig. 2.4.13) and a “gap” in the interaction zone above that channel (Fig. 2.4.9). In all likelihood these drop-like inclusions broke away from the interaction zone and were transported to the molten pool through the cracks in the crust above the interaction zone. There they exchanged components with corium, i.e. got enriched with U, Zr and O and their iron was depleted because of dissolution in molten corium.

The analysis of interaction zone in template №2 showed that its microstructure is similar to that of interaction region of template №1 (cf. Fig. 2.4.2, Fig. 2.4.3, region 1-1, Fig. 2.4.4, Fig. 2.4.14, region 5-1, Fig. 2.4.16 region 7 and Fig. 2.4.20, region 10). The interaction zone has a dendrite microstructure, which looks like iron dendrites with small amounts of Cr, Ni, Mg and Si (Fig. 2.4.3, Table 2.4.2, point P1 and Fig. 2.4.16, Table 2.4.13, point P1), iron-based phases with saturated Zr (Fig. 2.4.3, Table 2.4.2, point P2 and Fig. 2.4.16, Table 2.4.13, point P2) and U (Fig. 2.4.16, Table 2.4.13, point P3), also eutectics zones (Fig. 2.4.14, regions 5-1-1 and 5-1-2, Fig. 2.4.16, regions 7-2 and 7-3). The eutectics zone composition is presented in Tables 2.4.11 (Eut1 and Eut2) and 2.4.13 (Eut1, Eut2, Eut3 and Eut4). The similarity of eutectics zones composition in different parts of the interaction region is noteworthy. Negligible variations of composition, which exceed the value of measurement error, can be attributed to the catching of near-eutectics dendrites and phases by the probe.

The examination of total inventory of different interaction zone parts (the region was scanned from the center to periphery and from steel to corium) demonstrates the similarity of composition in the whole interaction region, which once again confirms the assumption, that this region had been in a fully molten state (compare Fig. 2.4.3, Table 2.4.2 – area SQ2, Fig. 2.4.14, Table 2.4.11, areas SQ1 and SQ2, Fig.2.4.16, Table 2.4.13 – areas SQ1, SQ2, SQ3 and SQ4, Fig. 2.4.20, Table 2.4.15 – area SQ1).

It also should be noted that in the crystallized U-Zr-Fe-O melt the untypical precipitation of a Zr-based (likely to be β-Zr) phase having the insignificant Fr and O presence is observed. This phenomenon can be attributed to the peculiarities of the U-Zr-Fe-O melt crystallization in the conditions of fast cooling and oxygen deficit (cf., e.g. Fig. 2.4.15, Table 2.4.12 – point P1, Fig. 2.4.14 – zone 5-1-1, Fig. 2.4.20 – zone 10-1).

The interaction boundary of this region with steel was studied in more detail. The studies were carried out from the center to periphery of the template (Fig 2.4.15, Fig. 2.4.16 – region 7-5, Fig. 2.4.18, Fig. 2.4.20 and Fig. 2.4.21). A distinct interaction boundary of U-Zr-Fe-O melt with steel was found, and presence in steel the Zr-based phase with a minor content of iron and oxygen in the ~ 5 μm-thick zone adjacent to the U-Zr-Fe-O melt boundary (e.g., Fig.2.4.20 – region 10-1-1, Table 2.4.15 – point P1, Fig. 2.4.21 – region 11-1, Table 2.4.16 – point P1). In all likelihood the penetration of Zr and O deep into steel followed the mechanism of inter-grain diffusion. A characteristic picture, which resulted from the temperature field peculiarities in this region and which confirms this assumption, is observed in the periphery region of interaction boundary (Fig. 2.4.21) – inter-grain space is dotted with zirconium (steel microstructure is distinct) and diffusion penetration region is evident. Therefore, the following two facts testify in favor of the inter-grain diffusion: 1) steel grain outlines are visible (Fig. 2.4.21); 2) a clear boundary of zirconium diffusion is observed, which can be explained by activation of the inter-grain transfer at a certain temperature, which equals to the melting temperature of the surface (inter-grain) phase.

Two crystallization pictures became evident after the analysis of the interaction zone. Close to the crust rupture area above the U-Zr-Fe-O melt a 50 μm crust of pure α-Zr is observed (Fig. 2.4.16 – region 7-4, Table 2.4.13 – point P4), above which UO_2 is crystallized (Fig. 2.4.16 – region 7-4, Table 2.4.13 – point P6) with inclusions of Fe and Zr-based phase with small quantities of U, Cr and O (Fig. 2.4.16 – region 7-4, Table 2.4.13 – point P5). In the zone of unbroken crust (Fig. 2.4.9 and Fig. 2.4.19 – region 9) a zone of crystallized iron-based melt enriched with U, Zr and O is observed above the crystallized U-Zr-Fe-O and a shrinking crack (Fig. 2.4.19 – region 9-1, Table 2.4.14 – area SQ1), UO_2 containing small amount of Zr and Fe precipitates above it (Fig. 2.4.19 – region 9-1, Table 2.4.14 – areas SQ2 and SQ3).

The comparison of steel composition near the interaction region (Fig. 2.4.3, Table 2.4.2 – area SQ1) and at a 3 cm distance from it (Fig. 2.4.9, Fig. 2.4.22, Table 2.4.17) shows the absence of any differences (taking into account the composition determination error 0.3 mass.%).

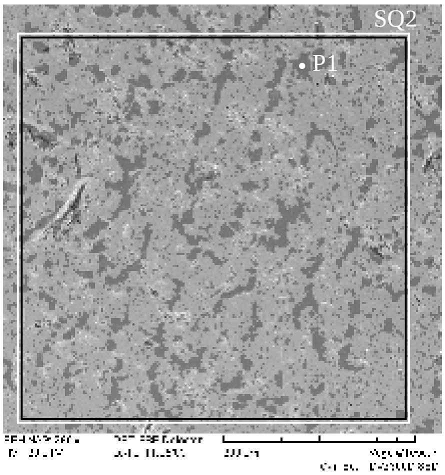

Fig. 2.4.10. Microphotograph of region 1 (crystallized corium)

Table 2.4.7

EDX-analysis of region 1

№		U	Zr	Fe	Th	O
SQ_{Cor} (2×2 mm)	mass.%	59.97	24.46	0.41	0.76	14.4
	mol.%	17.61	18.75	0.52	0.23	62.9
SQ2 (0.5×0.5 mm)	mass.%	59.65	24.69	0.37	0.68	14.61
	mol.%	17.36	18.75	0.46	0.2	63.23
P1	mass.%	9.2	82.75	0.82	-	7.23
	mol.%	2.74	64.23	1.04	-	32

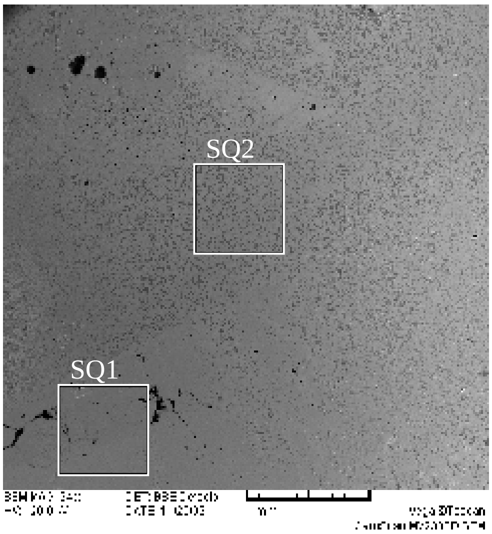

Fig. 2.4.11. Microphotograph of region 2 (ununiformly crystallized corium)

Table 2.4.8

EDX- analysis of region 2

№		**U**	**Zr**	**Fe**	**O**
SQ1 (0.5×0.5 mm)	mass.%	79.61	7.03	-	13.36
	mol.%	26.83	6.18	-	66.99
SQ2 (0.5×0.5 mm)	mass.%	59.91	26.68	0.95	12.46
	mol.%	18.78	21.83	1.27	58.12

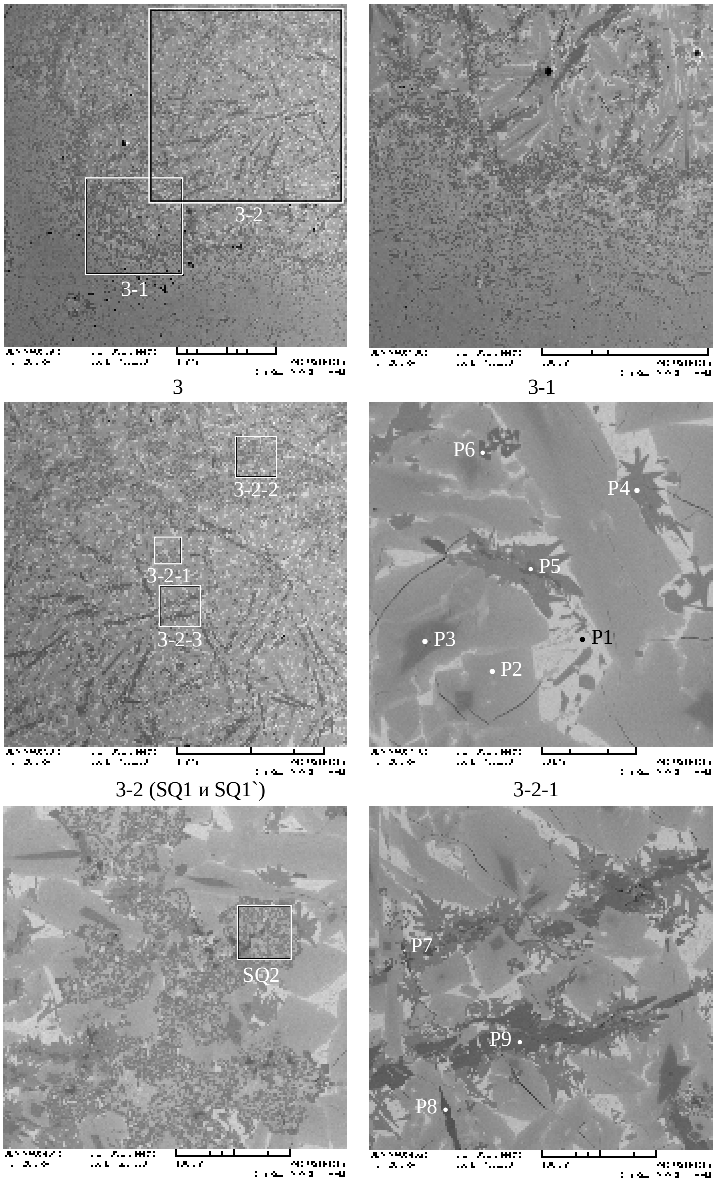

3 3-1

3-2 (SQ1 и SQ1`) 3-2-1

3-2-2 3-2-3

Fig. 2.4.12. Microphotograph of region 3 (metal-like inclusion into corium)

Table 2.4.9

EDX- analysis of region 3

№		U	Zr	Fe	Cr	Th	O
SQ1 (2×2 mm)	mass.%	55.44	25.21	14.71	-	-	4.64
	mol.%	21.92	26	24.79	-	-	27.29
SQ1` (2×2 mm)	mass.%	55.68	24	16.29	-	-	4.03
	mol.%	22.48	25.28	28.03	-	-	24.21
SQ2 (50×50 μm)	mass.%	54.27	27.6	10.89	-	-	7.24
	mol.%	19.35	25.68	16.55	-	-	38.41
P1	mass.%	86.63	2.47	5.23	-	0.66	5.01
	mol.%	45.46	3.38	11.7	-	0.36	39.11
P2	mass.%	54.73	26.45	14.44	-	0.97	3.41
	mol.%	23.09	29.12	25.97	-	0.42	21.4
P3	mass.%	25	60.86	11.77	-	-	2.37
	mol.%	9.29	58.98	18.63	-	-	13.1
P4	mass.%	40.22	28.62	27.5	0.73	-	2.94
	mol.%	14.41	26.75	41.98	1.2	-	15.67

P5	mass.%	40.58	28.7	27.19	0.84	-	2.69
	mol.%	14.74	27.21	42.11	1.4	-	14.54
P6	mass.%	54.88	25.2	13.35	-	-	6.57
	mol.%	19.94	23.89	20.67	-	-	35.51
P7	mass.%	32.85	45.76	18.3	0.33	-	2.77
	mol.%	12.03	43.74	28.57	0.55	-	15.1
P8	mass.%	17.39	74.3	3.79	-	-	4.53
	mol.%	5.9	65.78	5.48	-	-	22.84
P9	mass.%	16.32	36.43	43.88	1.56	-	1.81
	mol.%	4.91	28.59	56.25	2.15	-	8.1

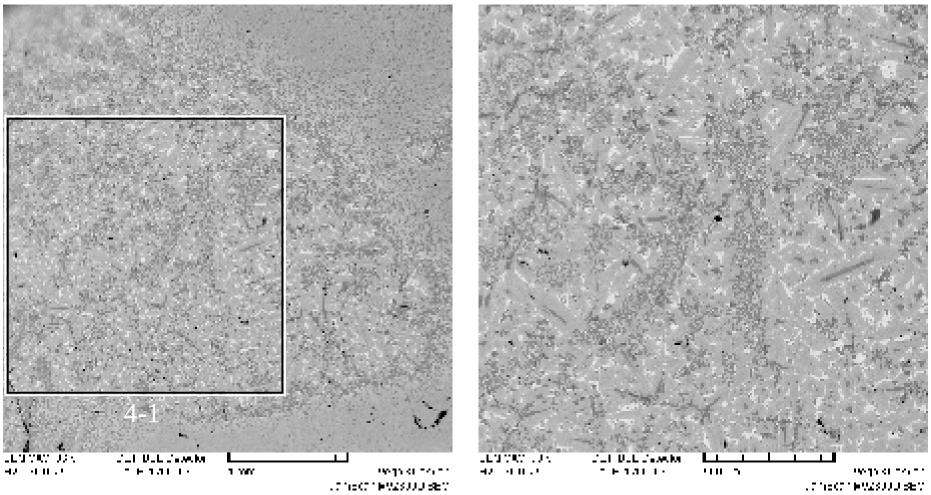

4 4-1 (SQ1 и SQ1`)

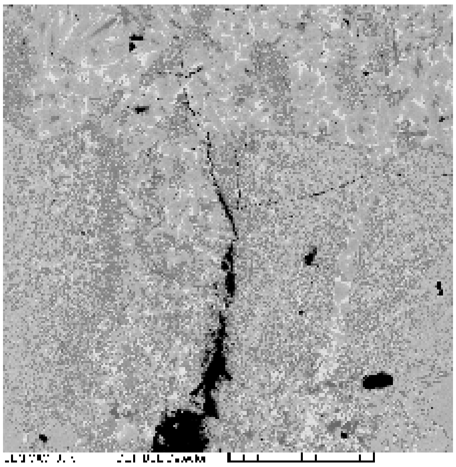

4`

Fig. 2.4.13. Microphotograph of region 4 (metal-like inclusion into corium)

Table 2.4.10

EDX- analysis of region 4

№		U	Zr	Fe	O
SQ1 (1.5×1.5 mm)	mass.%	56.35	25.32	13.98	4.35
	mol.%	22.84	26.78	24.15	26.23
SQ1` (1.5×1.5 mm)	mass.%	54.6	26.63	14.41	4.36
	mol.%	21.8	27.75	24.53	25.91

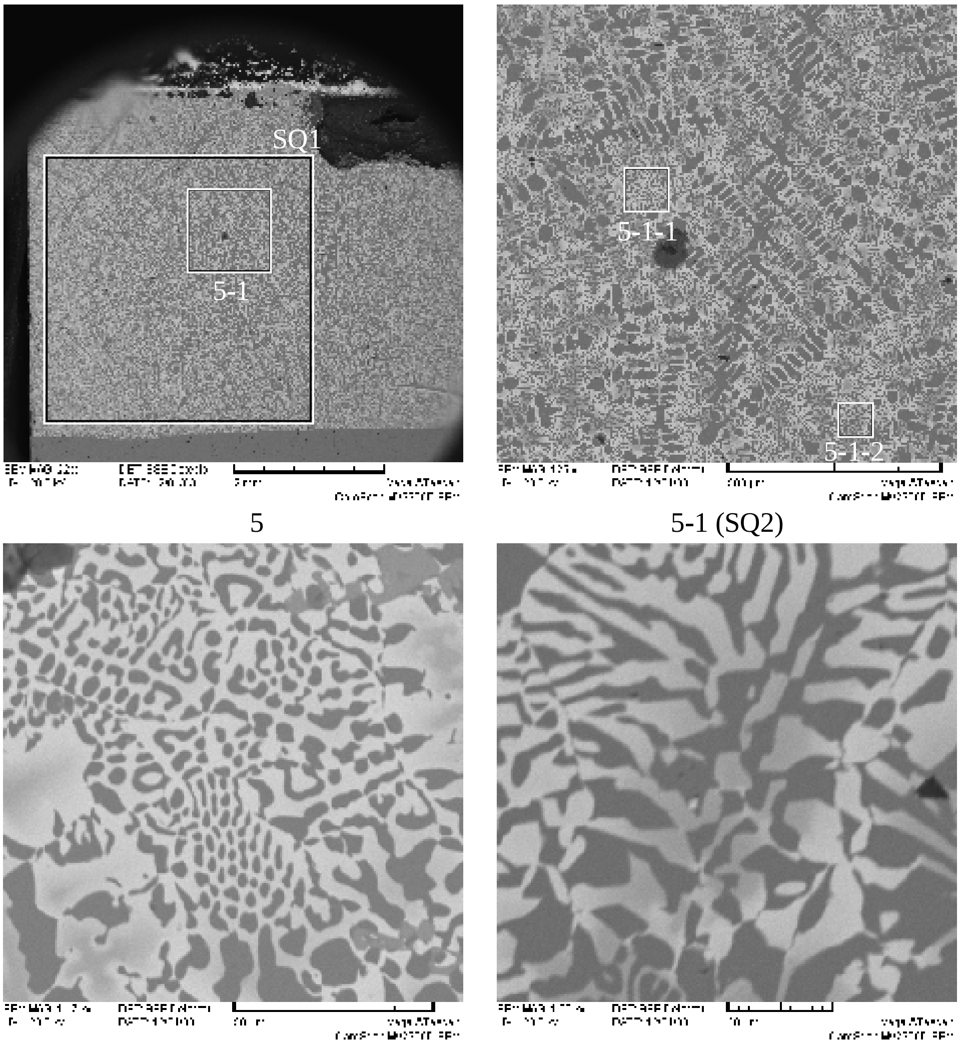

5 5-1 (SQ2)

5-1-1 (Eut1) 5-1-2 (Eut2)

Fig. 2.4.14. Microphotograph of region 5 (U-Zr-Fe-(O) melt – steel interaction boundary)

Table 2.4.11

EDX- analysis of region 5

№		**U**	**Zr**	**Fe**	**Cr**	**Ni**	**O**
SQ1 (4×4 mm)	mass.%	25.65	5.44	64.4	1.85	0.97	1.69
	mol.%	7.29	4.03	78.01	2.41	1.12	7.15
SQ2 (1×1 mm)	mass.%	24.37	4.77	66.56	1.89	0.91	1.5
	mol.%	6.86	3.5	79.87	2.44	1.04	6.28
Eut1	mass.%	37.53	1.74	56.57	1.31	0.92	1.93
	mol.%	11.67	1.41	74.97	1.86	1.16	8.93
Eut2	mass.%	26.7	4.12	65.25	1.97	0.8	1.16
	mol.%	7.74	3.12	80.59	2.61	0.94	5

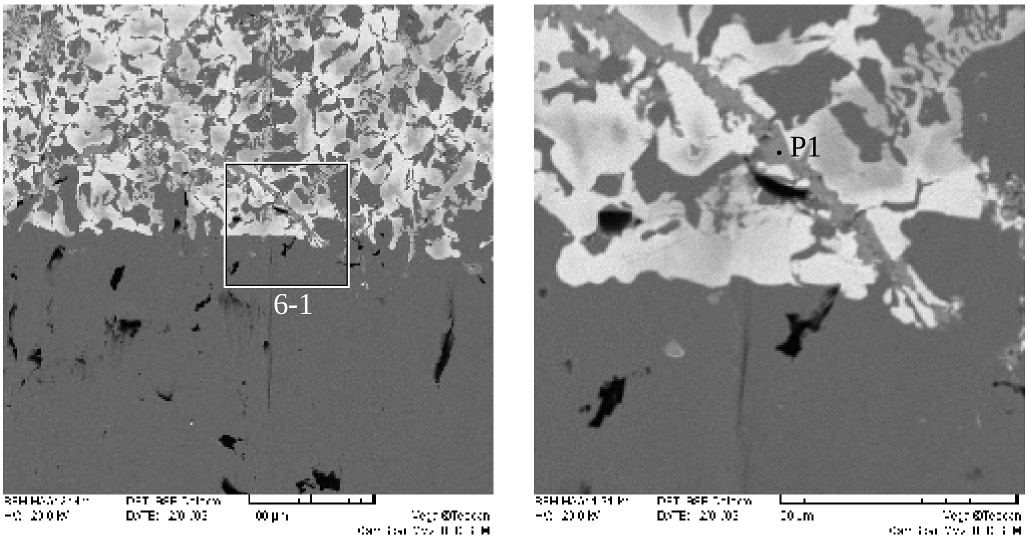

6 6-1

Fig. 2.4.15. Microphotograph of region 6 (U-Zr-Fe-(O) melt – steel interaction boundary)

Table 2.4.12

EDX- analysis of region 6

№		U	Zr	Fe	O
P1	mass.%	-	97.22	0.92	1.86
	mol.%	-	88.93	1.37	9.7

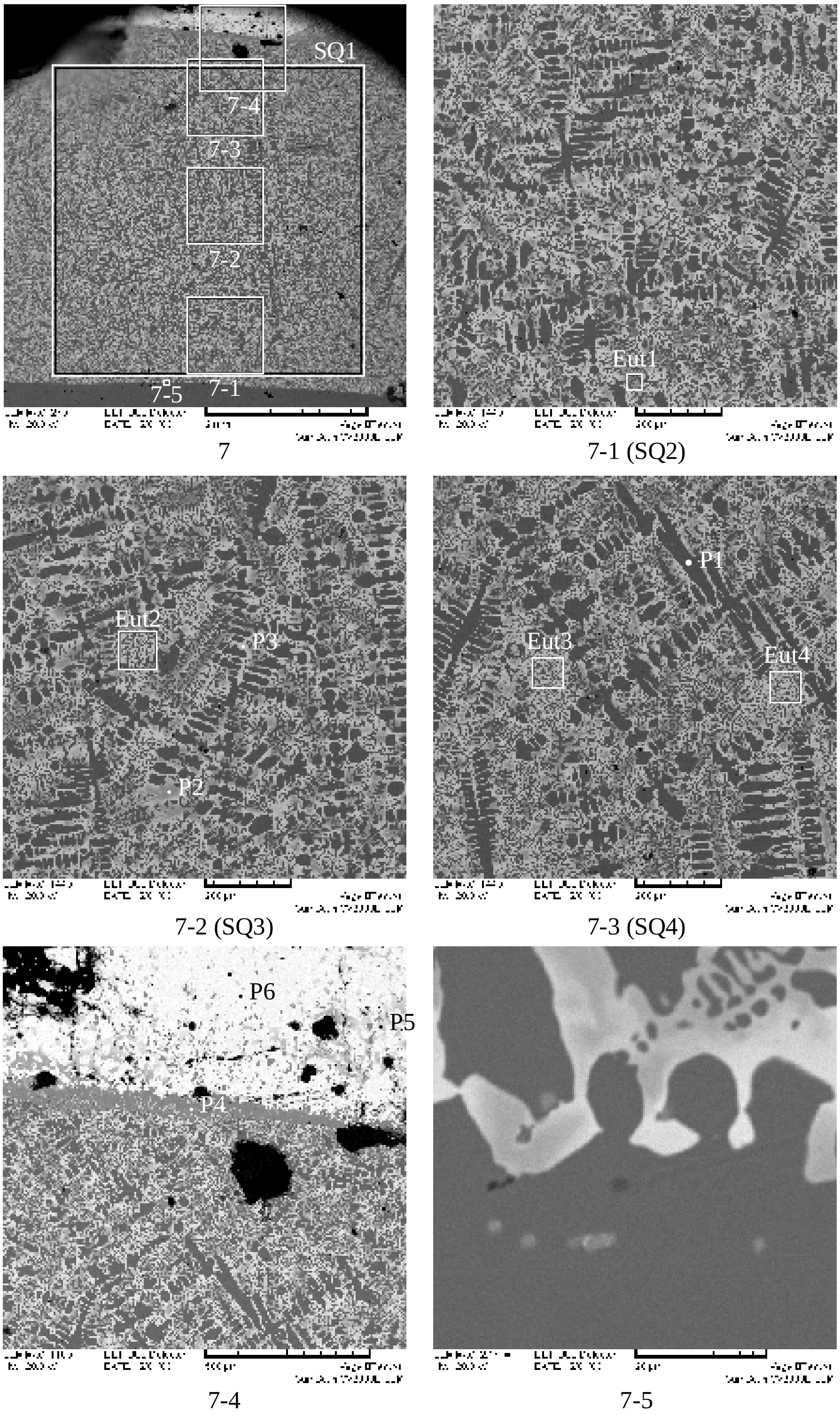

7

7-1 (SQ2)

7-2 (SQ3)

7-3 (SQ4)

7-4

7-5

Fig. 2.4.16. Microphotograph of region 7 (crystallized U-Zr-Fe-(O) melt and boundaries of its interaction with steel and corium)

Table 2.4.13

EDX- analysis of region 7

№		U	Zr	Fe	Cr	Ni	O
SQ1	mass.%	23.72	5.41	66.3	2.04	0.76	1.77
(4×4 mm)	mol.%	6.6	3.93	78.68	2.6	0.86	7.33
SQ2	mass.%	24.61	5.71	65.42	2	0.68	1.58
(1×1 mm)	mol.%	6.96	4.21	78.82	2.59	0.78	6.64
SQ3	mass.%	24.02	5.15	66.71	2.02	0.83	1.27

(1×1 mm)	mol.%	6.8	3.8	80.48	2.62	0.95	5.35
SQ4 (1×1 mm)	mass.%	23.56	4.79	67.08	2.21	0.8	1.56
	mol.%	6.57	3.49	79.74	2.82	0.91	6.47
P1	mass.%	-	-	95.94	3.7	-	0.36
	mol.%	-	-	94.83	3.93	-	1.24
P2	mass.%	22.57	22.09	51.79	0.64	1.06	1.85
	mol.%	6.72	17.17	65.75	0.87	1.28	8.2
P3	mass.%	59.89	2.31	34.07	-	0.94	2.79
	mol.%	23.36	2.35	56.62	-	1.49	16.18
P4	mass.%	-	95.66	-	-	-	4.34
	mol.%	-	79.45	-	-	-	20.55
P5	mass.%	30.1	22.85	44.15	1.11	-	1.79
	mol.%	9.72	19.26	60.78	1.64	-	8.6
P6	mass.%	88.06	1.54	-	-	-	10.4
	mol.%	35.68	1.63	-	-	-	62.69
Eut1	mass.%	26.62	6.43	62.72	1.69	0.81	1.73
	mol.%	7.66	4.83	76.93	2.23	0.95	7.41
Eut2	mass.%	35.63	2.55	57.54	1.41	1.1	1.77
	mol.%	10.97	2.05	75.51	1.99	1.37	8.11
Eut3	mass.%	38.53	1.04	56.5	1.24	1.21	1.48
	mol.%	12.24	0.86	76.53	1.8	1.56	7
Eut4	mass.%	37.94	1.29	56.77	1.24	1.11	1.65
	mol.%	11.93	1.06	76.09	1.79	1.42	7.72

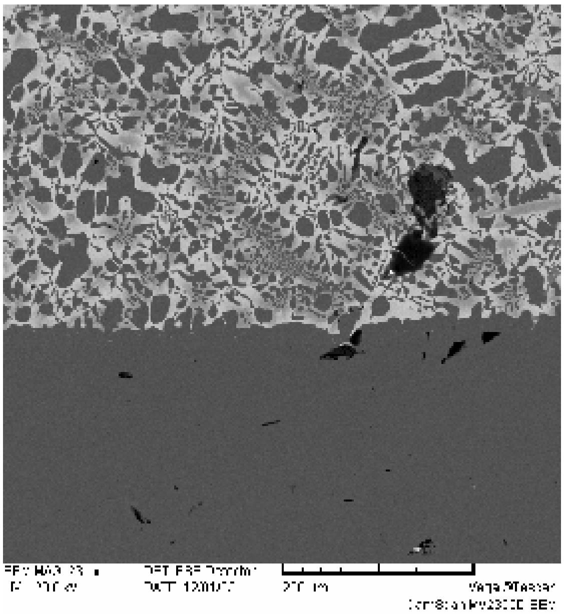

Fig. 2.4.18. Microphotograph of region 8 (U-Zr-Fe-(O) melt – steel interaction boundary)

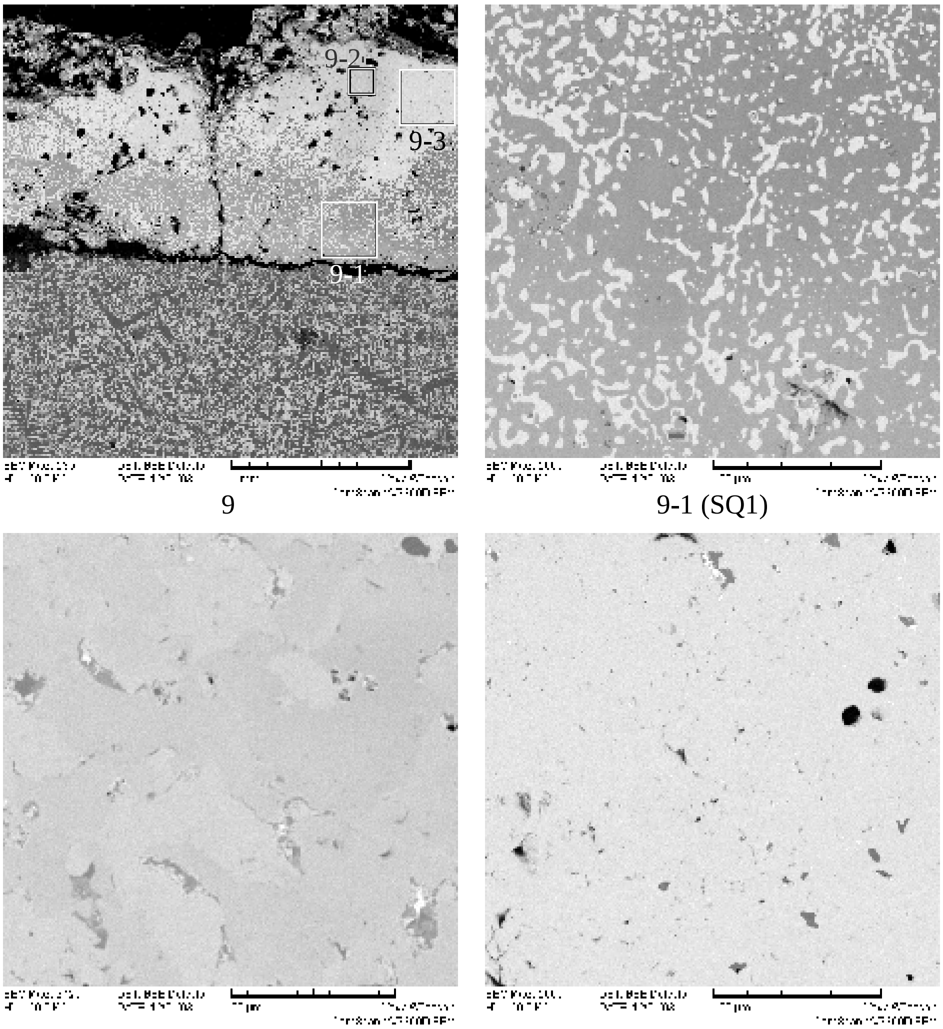

9 9-1 (SQ1)

9-2 (SQ2) 9-3 (SQ3)

Fig. 2.4.19. Microphotograph of region 9 (crust above the crystallized U-Zr-Fe-(O) melt)

Table 2.4.14

EDX- analysis of region 9

№		U	Zr	Fe	Cr	O
SQ1	mass.%	46.24	16.58	32.19	0.87	4.13
(0.2×0.2 mm)	mol.%	15.83	14.81	46.97	1.36	21.03
SQ2	mass.%	71.42	15.43	1.03	-	12.12
(0.1×0.1 mm)	mol.%	24.1	13.58	1.48	-	60.84
SQ3	mass.%	84.75	3.36	0.6	-	11.29
(0.1×0.1 mm)	mol.%	32.1	3.32	0.97	-	63.61

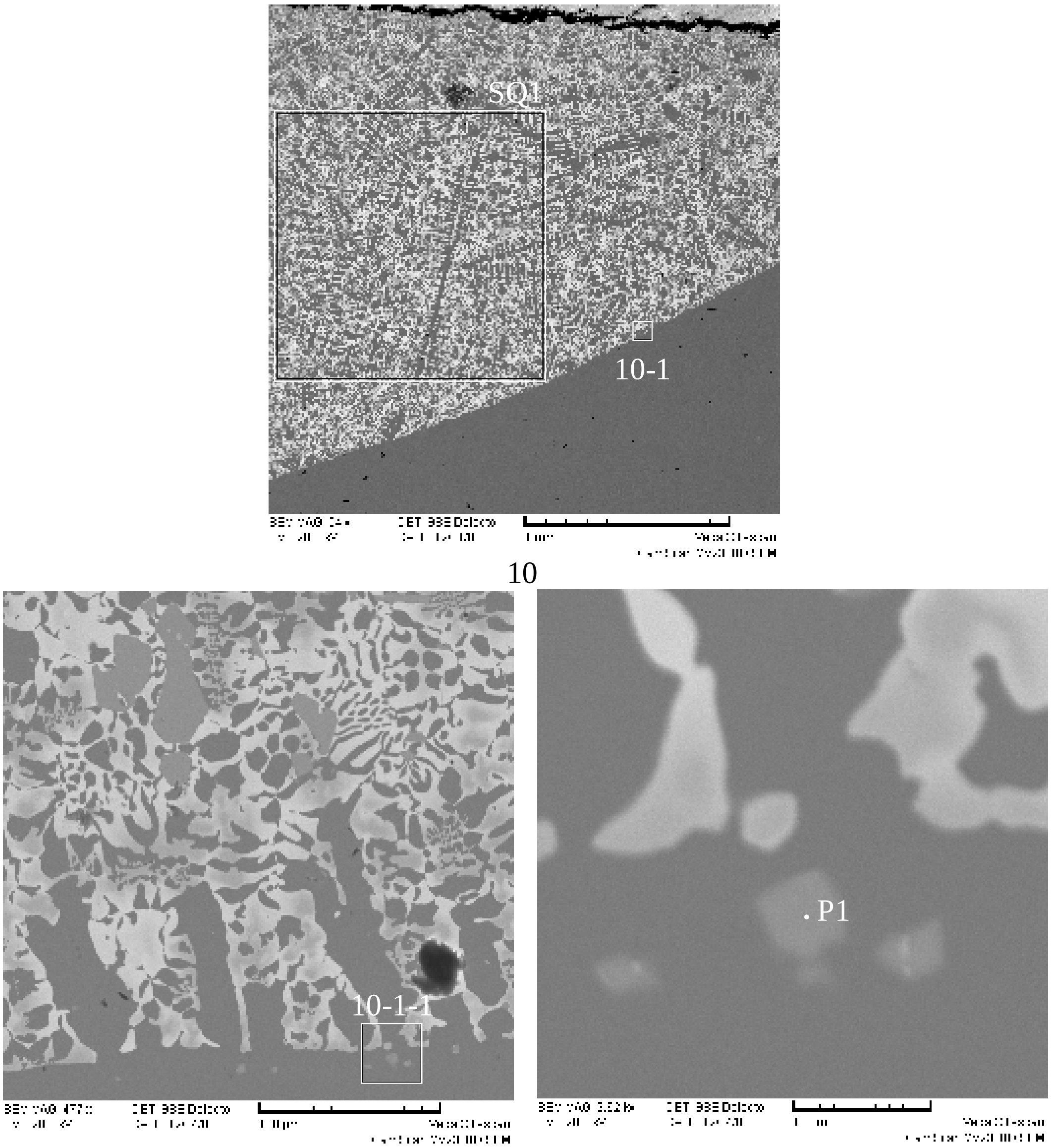

10

10-1

10-1-1

Fig. 2.4.20. Microphotograph of region 10 (U-Zr-Fe-(O) melt –steel interaction boundary)

Table 2.4.15

EDX- analysis of region 10

№		U	Zr	Fe	Cr	Ni	O
SQ1 (1.5×1.5 mm)	mass.%	23.93	8.13	64.37	2.18	0.68	0.71
	mol.%	6.98	6.19	80.03	2.91	0.8	3.08
P1	mass.%	-	96.12	3.08	-	-	0.8
	mol.%	-	90.93	4.76	-	-	4.31

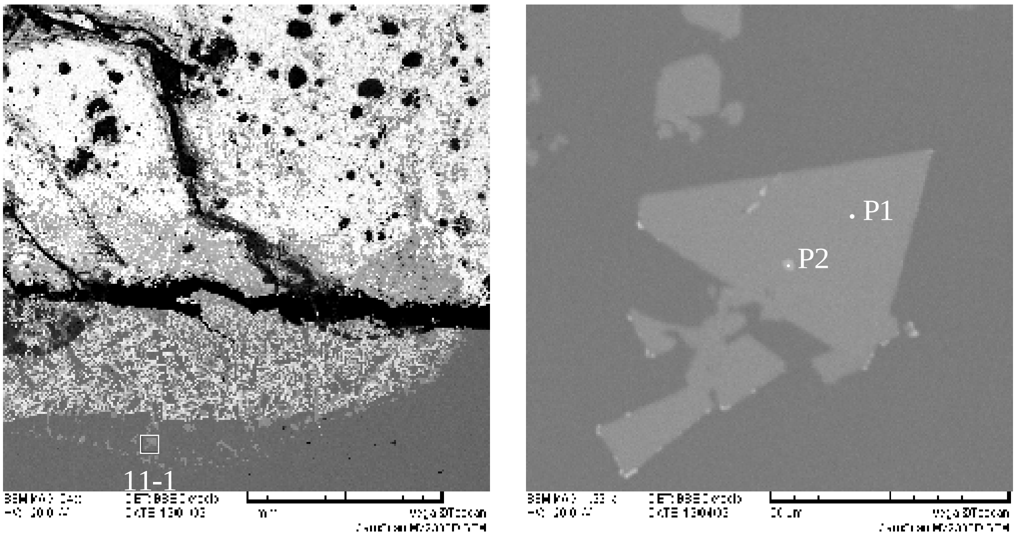

11 11-1

Fig. 2.4.21. Microphotograph of region 11 (U-Zr-Fe-(O) melt – steel interaction boundary)

Table 2.4.16

EDX- analysis of region 11

№		U	Zr	Fe	Cr	Ni		O
P1	mass.%	-	97.03	0.83	-	-	-	2.14
	mol.%	-	87.74	1.23	-	-	-	11.03
P2	mass.%	33.92	10.61	52.14	1.26	0.9	-	1.17
	mol.%	10.92	8.91	71.53	1.86	1.17	-	5.6

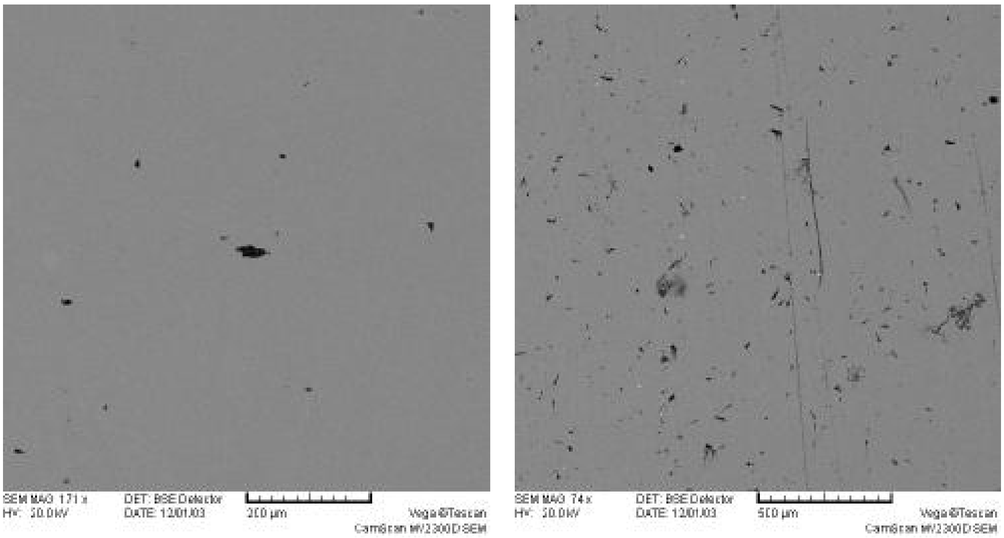

12 13

Fig. 2.4.22. Microphotograph of steel in regions 12 and 13

Table 2.4.17

EDX- analysis of steel

№		Fe	Cr	Ni	Mn	Si
P1	mass.%	95.61	2.23	1.19	0.49	0.48
	mol.%	95.05	2.38	1.12	0.5	0.95

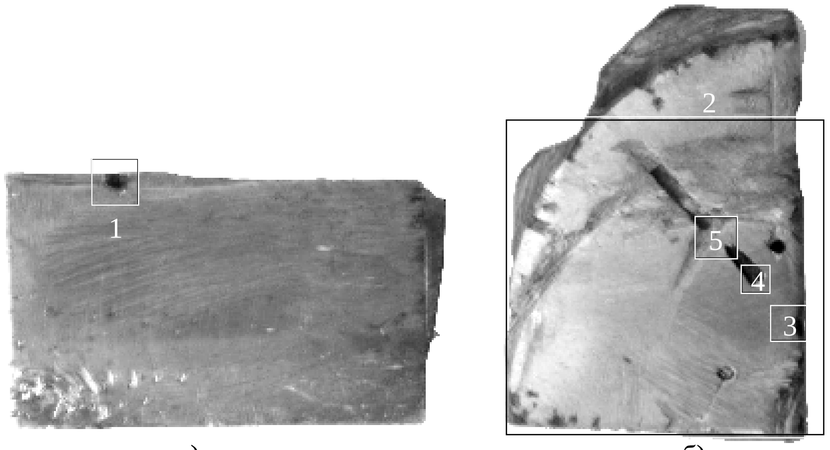

а) б)

Fig. 2.4.23. MC6 template № 3 with regions marked for examination

In order to study the U-Zr-Fe-O melt penetration into the technological borehole the specimen cross-section (taken on the level of the borehole center) and longitudinal section (template №3 with regions marked for examination, Fig. 2.4.23) have been studied.

SEM examination of the longitudinal section showed the absence of refractory crust between the U-Zr-Fe-O melt and borehole (Fig. 2.4.23 – a and Fig. 2.4.24).

Fig. 2.4.25 gives the image of template No3 cross section in the phase contrast regime. As evident from the microphotograph (Fig. 2.4.25), there are zones of U-Zr-Fe-O melt penetration into the borehole (also Fig. 2.4.26 – region 3, Fig. 2.4.27 – region 4 and Fig. 2.4.28 – region 5). But it is also evident (Fig. 2.4.25 – region 2-1), that there are borehole opening deformation zones without melt penetration into it. The analysis also has shown that the melt has a high degree of homogeneity on the boundary with the hole (e.g. Fig. 2.4.27 – region 4-1). This fact can be explained by the capillary effects in the technological opening, which is sealed with steel plugs from both sides and filled with argon, (like drops in the pipette).

Another thing, which should be noted, is the appearance of Zr inter-grain diffusion in the periphery zone, as it was observed in the template (cf. Fig. 2.4.21, Table 2.4.16 and Fig. 2.4.28, Table 2.4.18).

In conclusion we would like to note a similar crystallization character in the interaction zone (U-Zr-Fe-O melt) for all three templates.

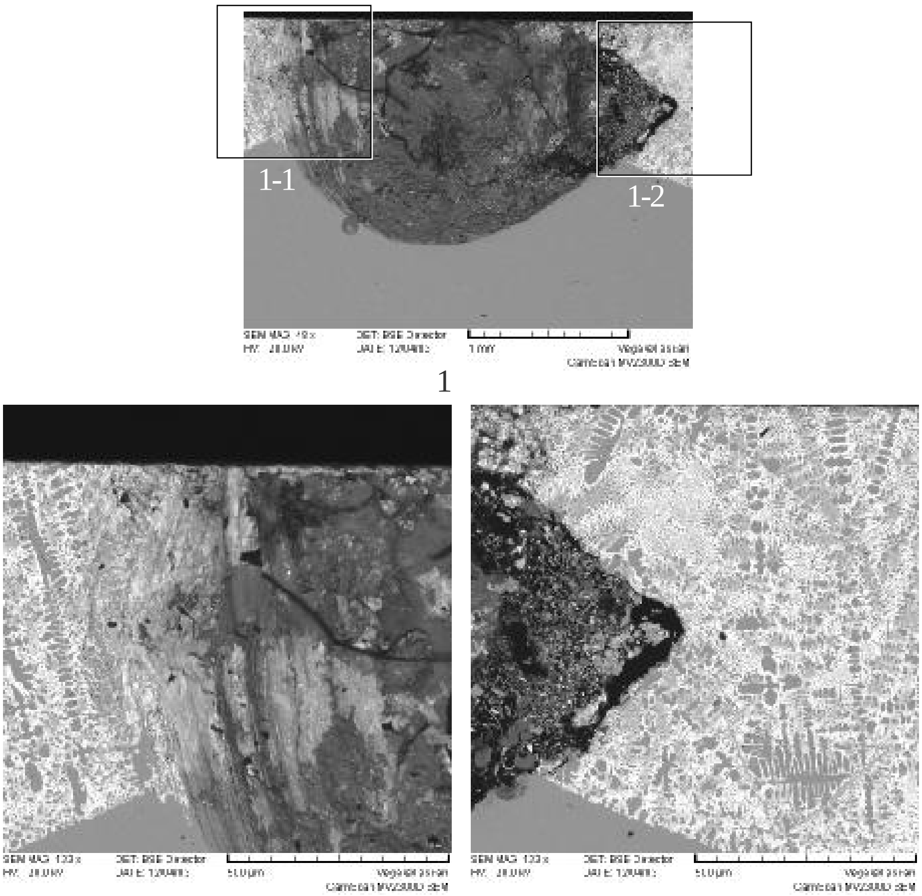

1-1 1-2

Fig. 2.4.24. Microphotograph of region 1 (technological USS hole)

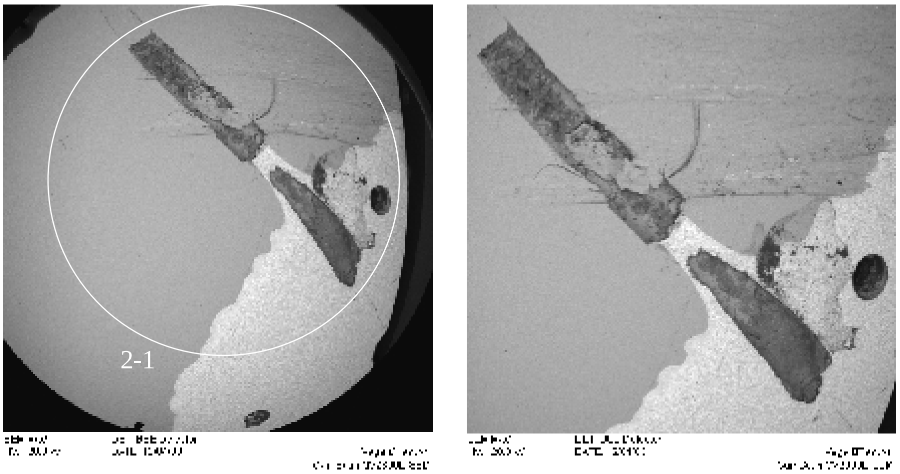

2 2-1

Fig. 2.4.25. Microphotograph of the diametrical section of the technological borehole (section 2 in Fig. 2.4.23)

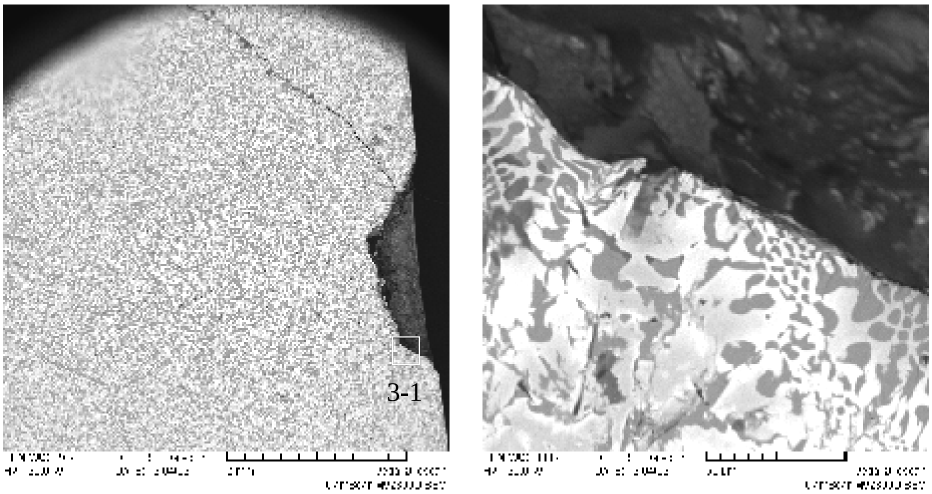

3 3-1

Fig. 2.4.26. Microphotograph of region 3 (edge of the technological borehole)

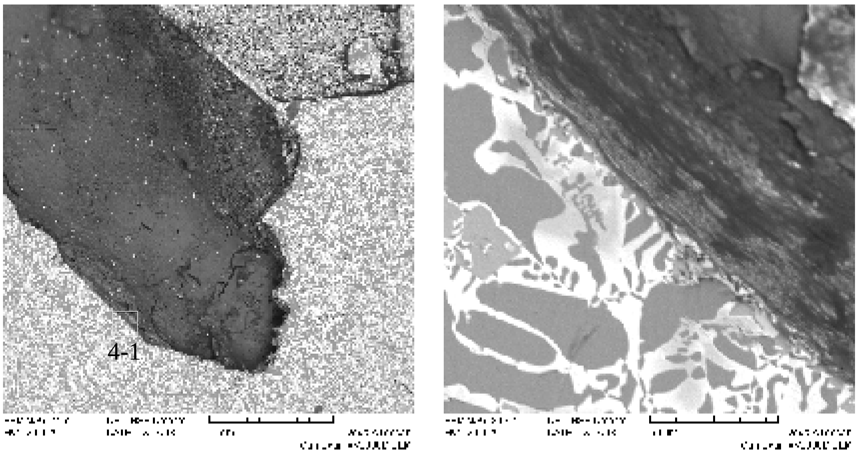

4 4-1

Fig. 2.4.27. Microphotograph of region 4

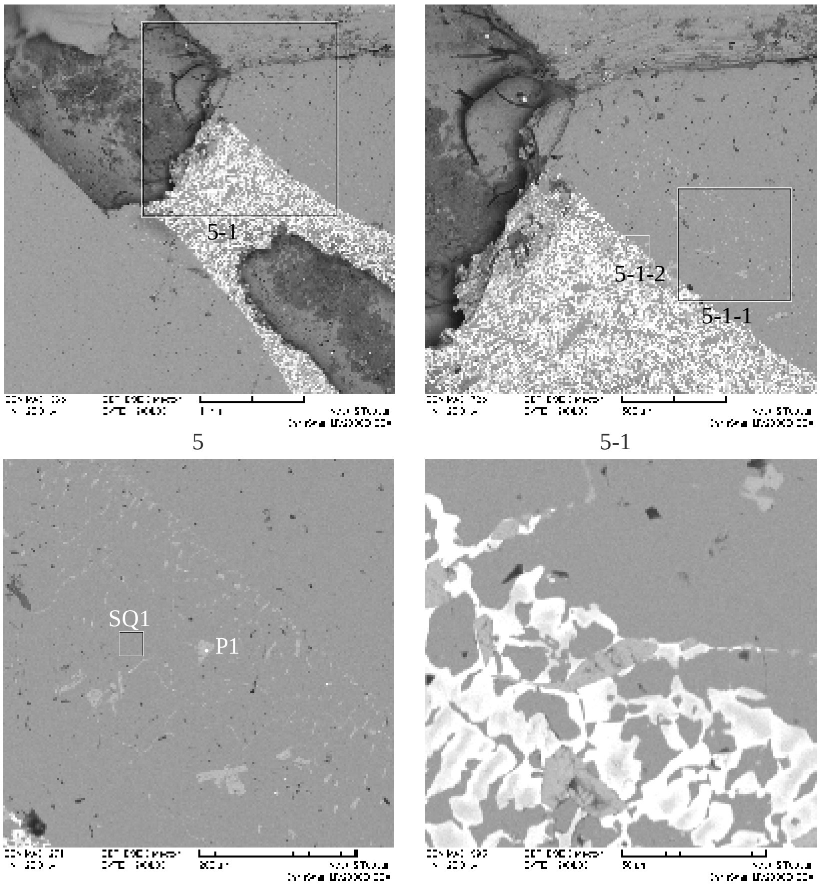

5 5-1

5-1-1 5-1-2

Fig. 2.4.28. Microphotograph of region 5

Table 2.4.18

EDX-analysis of region 5

№		Zr	Fe	Cr	Ni	Mn	O
SQ1	mass.%	-	95.37	3.26	0.8	0.57	-
	mol.%	-	95.16	3.5	0.76	0.58	-
P1	mass.%	97.51	1.45	-	-	-	1.04
	mol.%	92.16	2.24	-	-	-	5.6

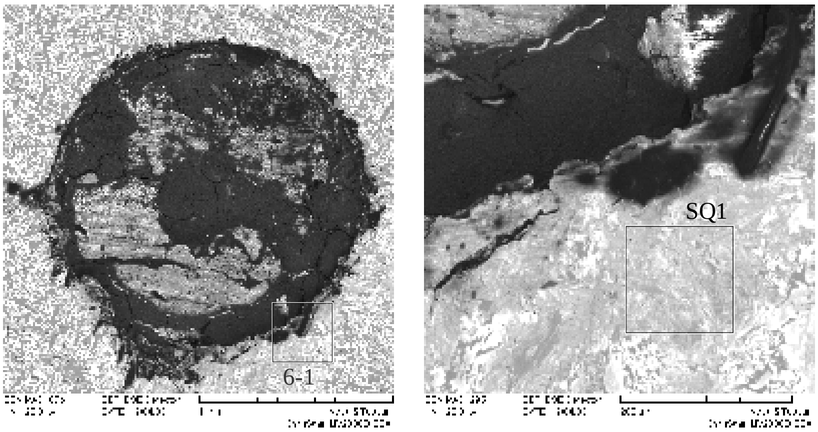

6 6-1

Fig. 2.4.29. Microphotograph of region 6

Table 2.4.19

EDX-analysis of region 5

№		U	Zr	Fe	Cr	Ni	Mn	O
SQ1	mass.%	24.1	4.26	67.71	1.89	0.8	0.4	0.84
	mol.%	6.89	3.17	82.48	2.48	0.92	0.5	3.56

SEM/EDX analysis conclusions

1. The chemical composition of the degenerated region between corium and steel is uniform (compare the data of regions 5, 7, 10 marked in Fig.2.4.9).
2. It can be asserted with a high degree of assurance, that before the crystallization this region was in a molten state. This is confirmed by the character of its microstructure – dendrites of the most refractory component, iron, and typical eutectic structure between the dendrites. The dendrite composition differs from the composition of steel. It serves as an additional confirmation of the phase being crystallized from the melt rather than being a solid-phase inclusion into the melt.
3. The composition of eutectics regions has been determined for different parts of the molten zone, and, as the analysis confirms, it varies rather insignificantly. I.e. we can assert with a high degree of certainty that the melt composition was within the following interval: iron (refractory component) – eutectics composition (fusible region). An eutectics point can be established for the considered system after determining the solidus temperature (on condition that the eutectics composition is known).

2.5. Metallographic examination of the specimen

The studies had two objectives:1) quality control of procured steel; 2) analyses of steel attacked by C-32 corium melt.

2.5.1. Quality control of procured steel

The MC6 specimen was manufactured from the vessel steel 15Kh2NMFA-A of VVER -1000 reactor produced by the “Izhorskie Zavodi” company.

Similar to MC5, a block was cut from the reactor vessel part. The MC6 specimen and a witness specimen were made from it.

The quality control of witness specimen included the XRF elemental analysis and microhardness measurements.

The content of basic components in the specimen, which was determined by XRF, proved that it corresponded to standard specifications TU 108-765-78 for the vessel steel 15Kh2NMFA-A.

Microhardness values were determined using 5 prints. The integral microhardness value of the control specimen was $H_\mu = 250 – 260$.

The pre-test specimen measurements were made from the top and from grooves lathed on the cylindrical surface. A caliper with scale factor 0,02 mm and stereoscopic microscopeMBS-9 with scale factor 14 μm and 50-fold magnification were used for the measurements

Fig 2.5.1,a shows distance A from the top to the first groove, distance B - to the control hole (acoustic defect) and diameter D of the hole. The measurements were made four times in the opposite points of the specimen, Fig. 2.5.1,b; the data are given in Table2.5.1.

Table 2.5.1

Steel specimen measurements

A_1	**A_2**	**A_3**	**A_4**	**B_1**	**B_2**	**D_1**	**D_2**
mm							
2,83	2,88	2.89	2,84	5,15	5,26	2,04	2,1

Specimen length L = 103,95 mm

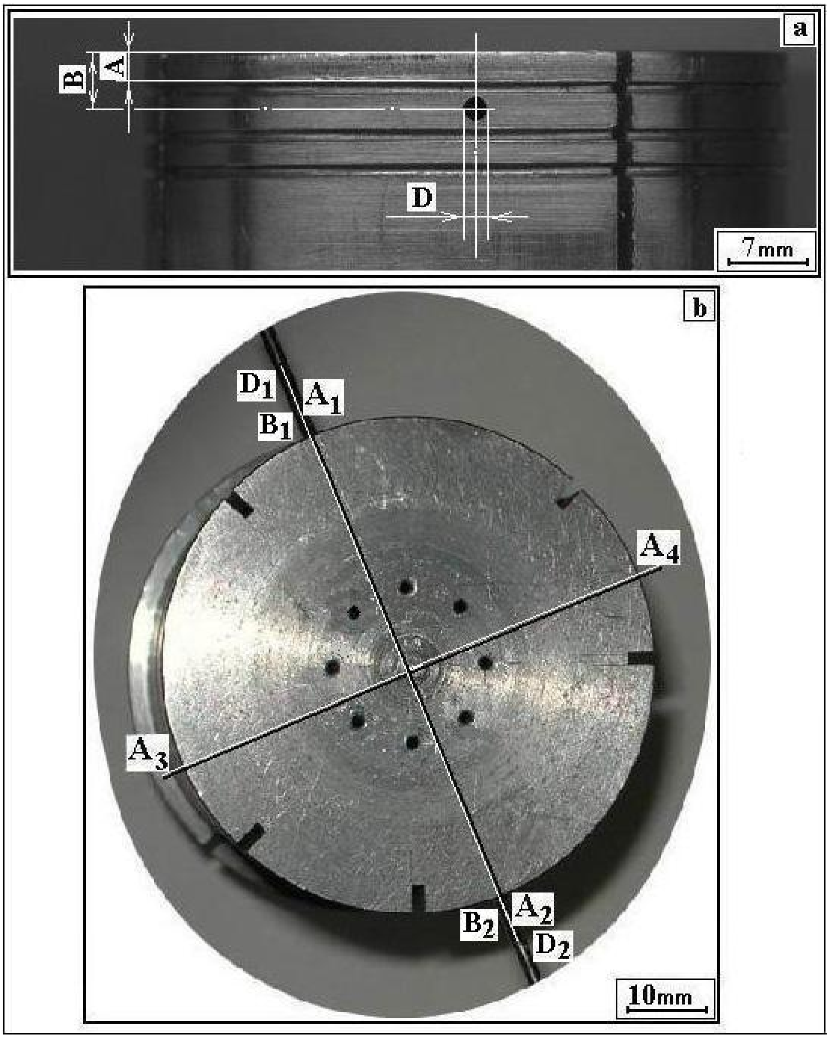

A (A_1, A_2, A_3, A_4), B (B_1, B_2), D (D_1, D_2)- measurement points

Fig. 2.5.1. Part of the lateral surface (a) and top (b) of the steel specimen before MC6 test

2.5.2. Steel ablation depth measurements

After the test all measurements were performed on the specimen longitudinal section. Direct measurements were performed with microhardness meter PMT-3 having magnification factor of 180^x and 487^x, and with stereoscopic microscope MBS-9 and 50^x and 100^x magnification. The scale factor of micrometer screw and object plate of the microhardnessmeter is 0,01 mm. The error was evaluated with stage micromemeter, it was ±10 µm. The scanned macrosection image was processed on computer. It was used for constructing specimen ablation curves, Fig 2.5.2, (line 2 and line 3)

The pre-and post-test specimen measurements showed that the top interaction boundary 2 was 3.45 mm deeper than original top position; and the interaction zone was 6,7 mm deep. Fig.2.5.2 shows the profilogram of the steel specimen length changes.

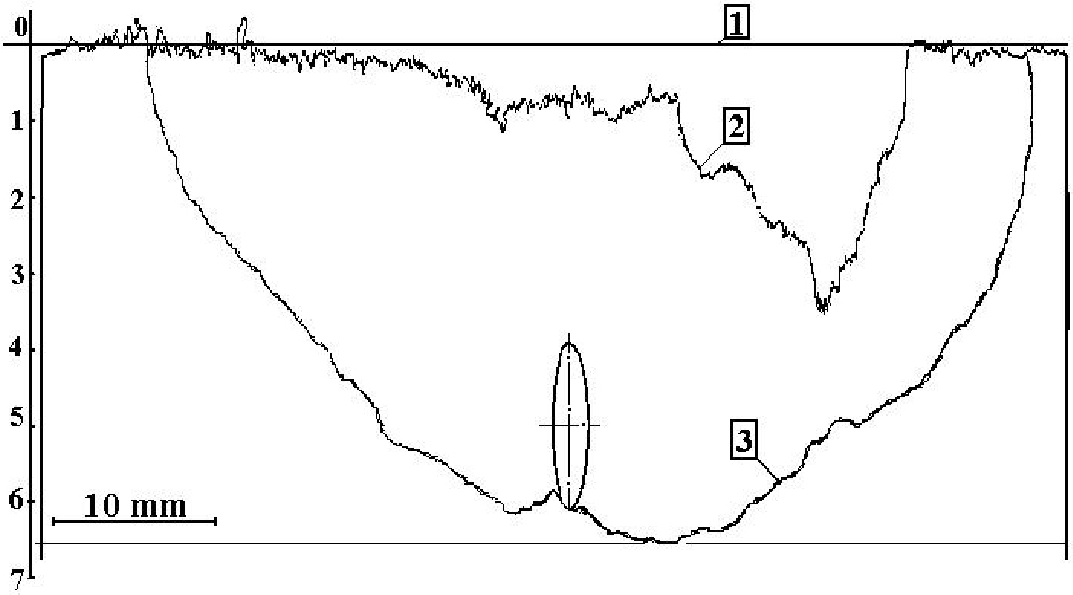

1 – initial position of the specimen top.
2 – boundary of oxides and iron melt enriched with U and Zr.
3 – boundary of the steel specimen and iron melt enriched with U and Zr.

Fig. 2.5.2. Profilogram of corium- U-Zr-Fe-O alloy - steel surfaces in the axial section of the specimen.

2.5.3. Steel macro- and microstructure after the test

The metallographic studies of the steel specimen were aimed at determining the thermal influence boundaries from T solidus to ~ 800°C. The following phenomena can leave indications of thermal influence:

- passing through solidus and cast structure stages;
- macrograin boundaries of former austenite, which grew at T > 1000°C and long-term heating;
- pearlite, intermediate or martensitic transformation of austenite at cooling and reflected in the cooled structure with a different grain pattern;
- grain coarsening of ferrite-pearlite mixture in the temperature interval of the incomplete recrystallization.

Templates for these studies were prepared in the following way. Corium ingot together with the specimen was embedded in epoxy, in order to avoid the destruction of corium ingot at cutting or exclude the flaking of posttest structures. The block was cut along and across its axis. The resulting sections are presented in Fig. 2.5.3, 2.5.4.

During the cutting one of the specimen sections broke along the yet uncut corium-steel interaction boundary. It happened of its own accord, though the section area was 40 mm^2. The fracture was brittle, grain size was up to 0,3 mm. The fracture revealed ≤0,2 mm pores and cracks. The microscopic studies of the fracture revealed three phases having different colors. The enlarged fracture is shown in Fig. 2.5.4, c.

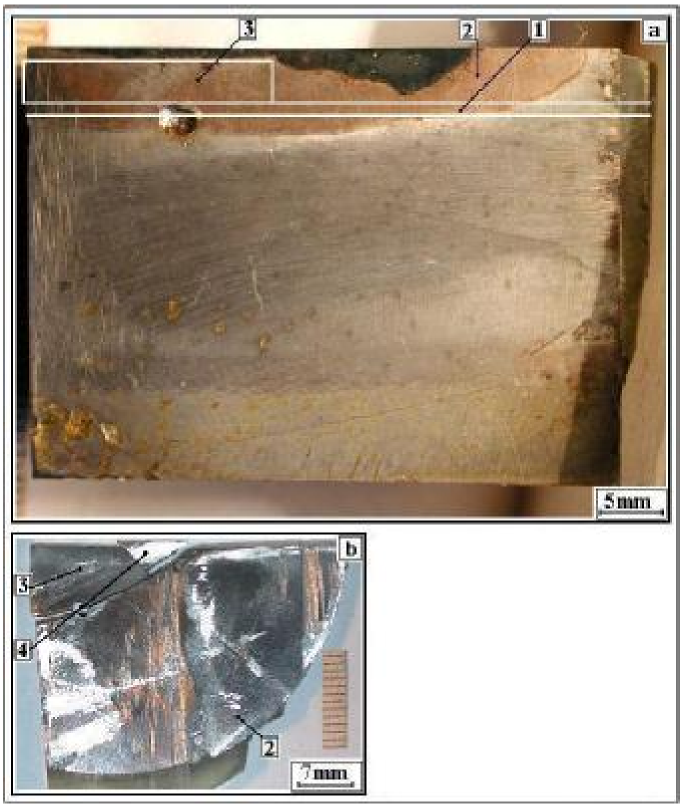

1 – cross cutting;
2 – 4 templates for material studies.

Fig. 2.5.3 Specimen top cutting schematics

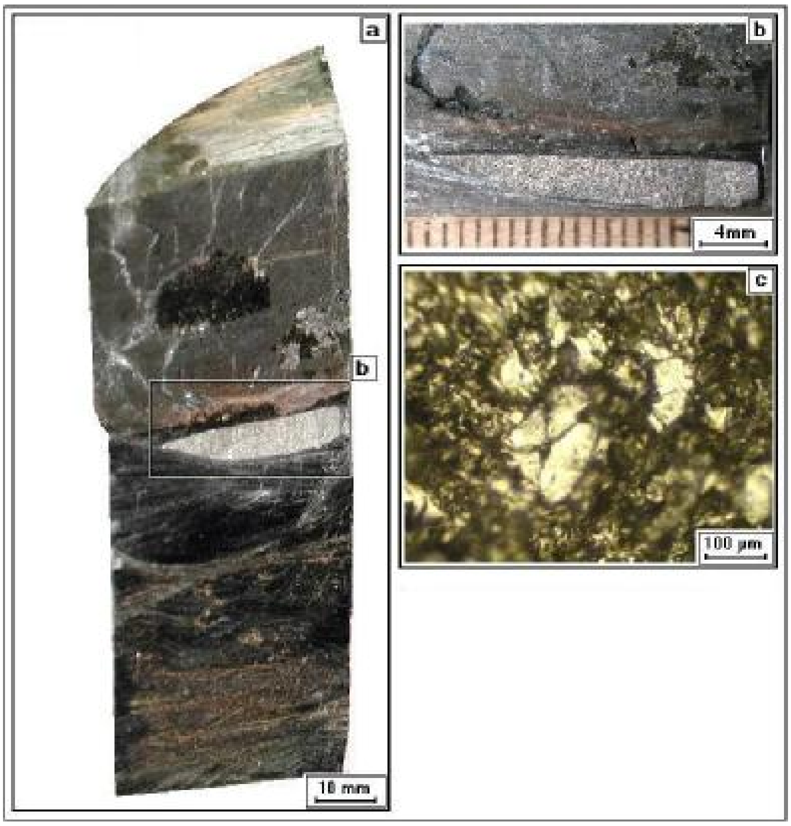

Fig. 2.5.4. Template of the corium-specimen longitudinal section (a) with a fractured section (b) and enlarged fracture fragment (c)

The template grinding and polishing followed a standard methodology. The pearlite and austentite steel etchants were used [9,10], their combined studies enabled to reveal the macro- and microstructure in the zone of high-temperature corium impact and to identify the structure of steel. The surface of sections was photographed by a digital camera "NIKON" through the metallographic microscope METALLUX with the magnification factor of 100; 200; 400 and 800.

Steel macro- and microstructure was studied on templates, Fig.2.5.5, where after the microscopic studies the boundaries of 4 - 7 temperature influence zones were marked along with the examination regions: A, B, C.

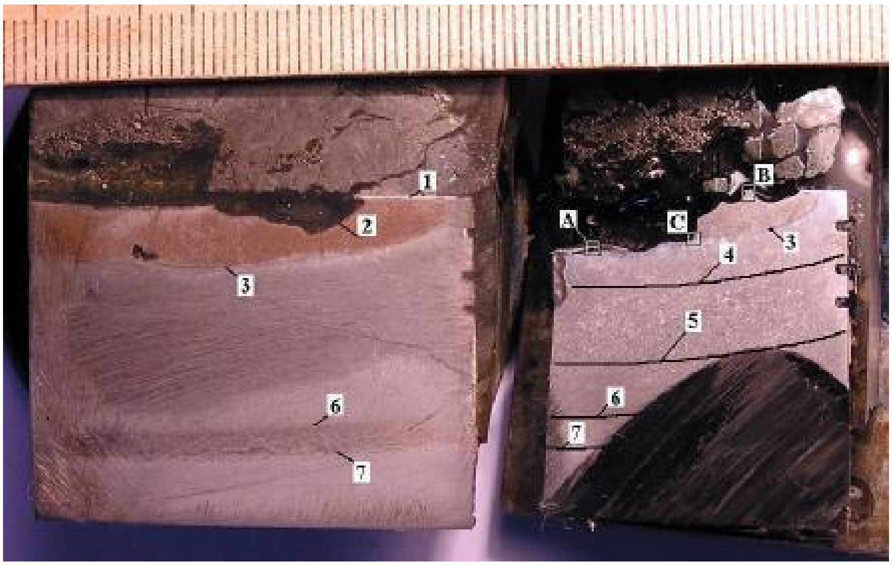

1- apparent plane of original specimen top;
2- profile of the specimen top after the test;
3- profile of the corium-steel interaction zone;
4- apparent plane of initial top;
5- profile of the specimen top after the test;
6- profile of the corium-steel interaction zone;
4-7- boundaries of zones of the melt temperature influence on steel macro- and microstructure;
A-C – parts of section used for the microstructure studies.

Fig. 2.5.5. Macrostructure of the longitudinal section of corium and steel specimen top

Let us consider the structures of alloy in the selected regions and along the zone boundaries.

Region A located on the lower boundary of zone 3. Flaking of metal is found on the surface. It is explained by the penetration of newly-formed melt into the metal (in this section), which probably got there from neighboring regions (Fig 2.5.6).

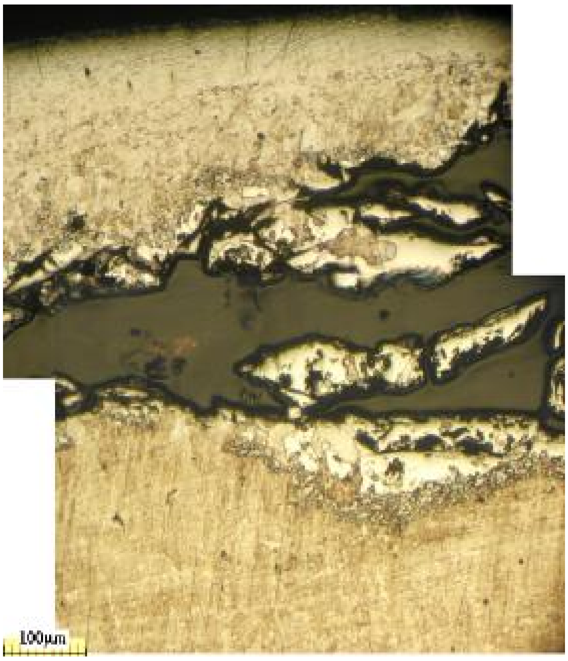

Fig. 2.5.6. Enraged fragment of steel and alloy optical image in region A.

Region B located in the cast structure of a newly-formed alloy. The process of primary crystallization is confirmed by elongated dendrites, which are clearly seen in the deep-layer structures of this zone (Fig. 2.5.7).

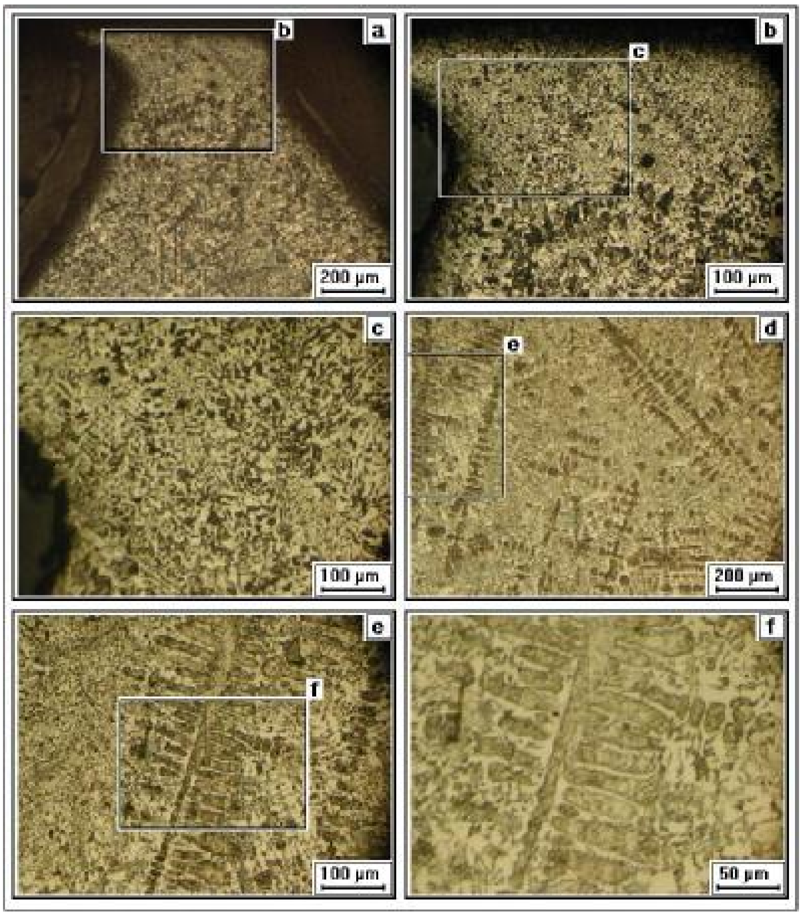

Fig. 2.5.7. Optical image of alloy microstructure in region B

Region C was chosen on boundary 3 between the interaction zone and unablated steel. The optical image of microstructure (Fig2.5.8) testifies to the wetting of steel by this newly-formed alloy and, consequently, to the possibility of a good diffusion exchange between the layers.

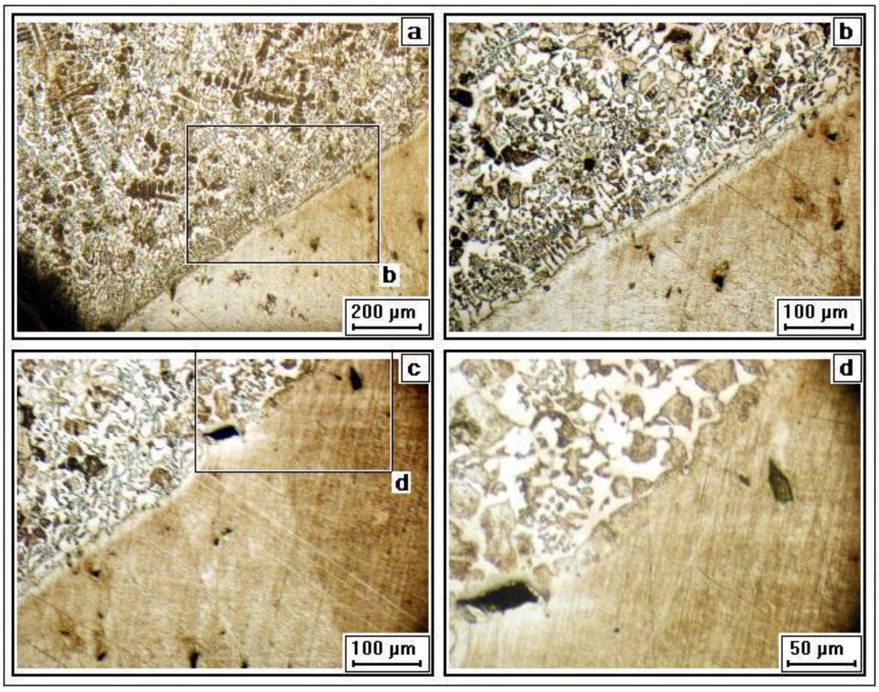

Fig. 2.5.8. Optical image of steel and alloy microstructure in region C

Let us consider the steel structure in different layers of thermal impact.

High-temperature layer between lines 3 - 4, Fig. 2.5.9.

Main features of steel contacting the interaction zone in austenite condition are: sharp grain coarsening and loss of carbon. After the austenite recrystallization the linear grain size continues to be over 600 µm, which corresponds to a zero size. The structure consists of such macro-grains having 1-5 size . The grains have ruptures, which can be interpreted as gas voids. Such structure is possible, if the steel carbon gets oxidized by diffused oxygen and carbon oxide is produced.

On boundary 4 in the lower layer the grains become smaller (size 4-6). Their structure is composed of pearlite enclosed in ferrite lattice. (Fig. 2.5.9).

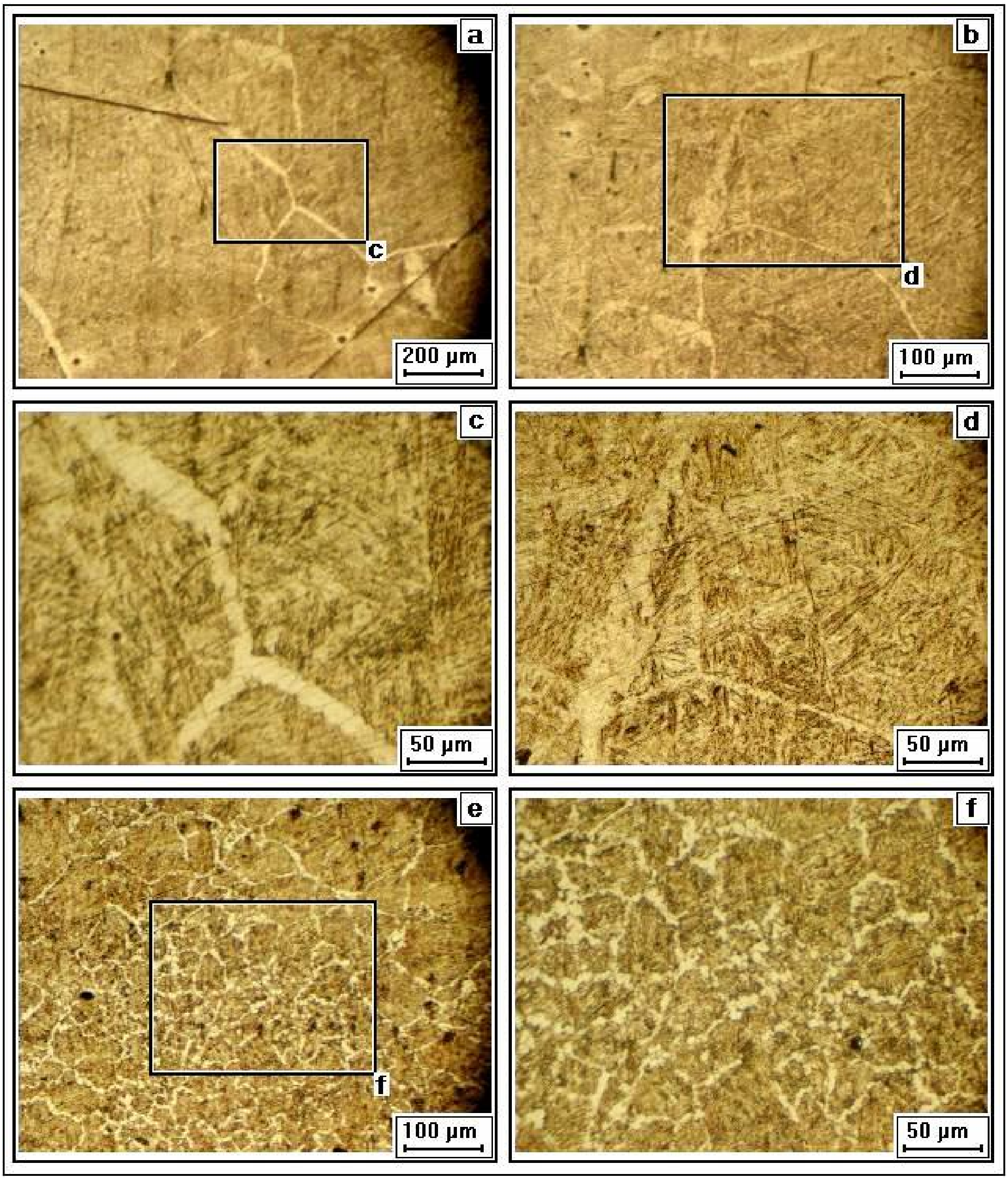

Fig. 2.5.9. Steel microstructure with enlarged fragments in the region marked above line 4

Average temperature layer between lines 4 - 6, Fig.2.5.10.

A typical image of superheated steel with Widmanstatten pattern of large-grain ferrite-pearlite mixture. A considerable presence of pearlite testifies to an enhanced content of carbon, which diffused here from upper layers.

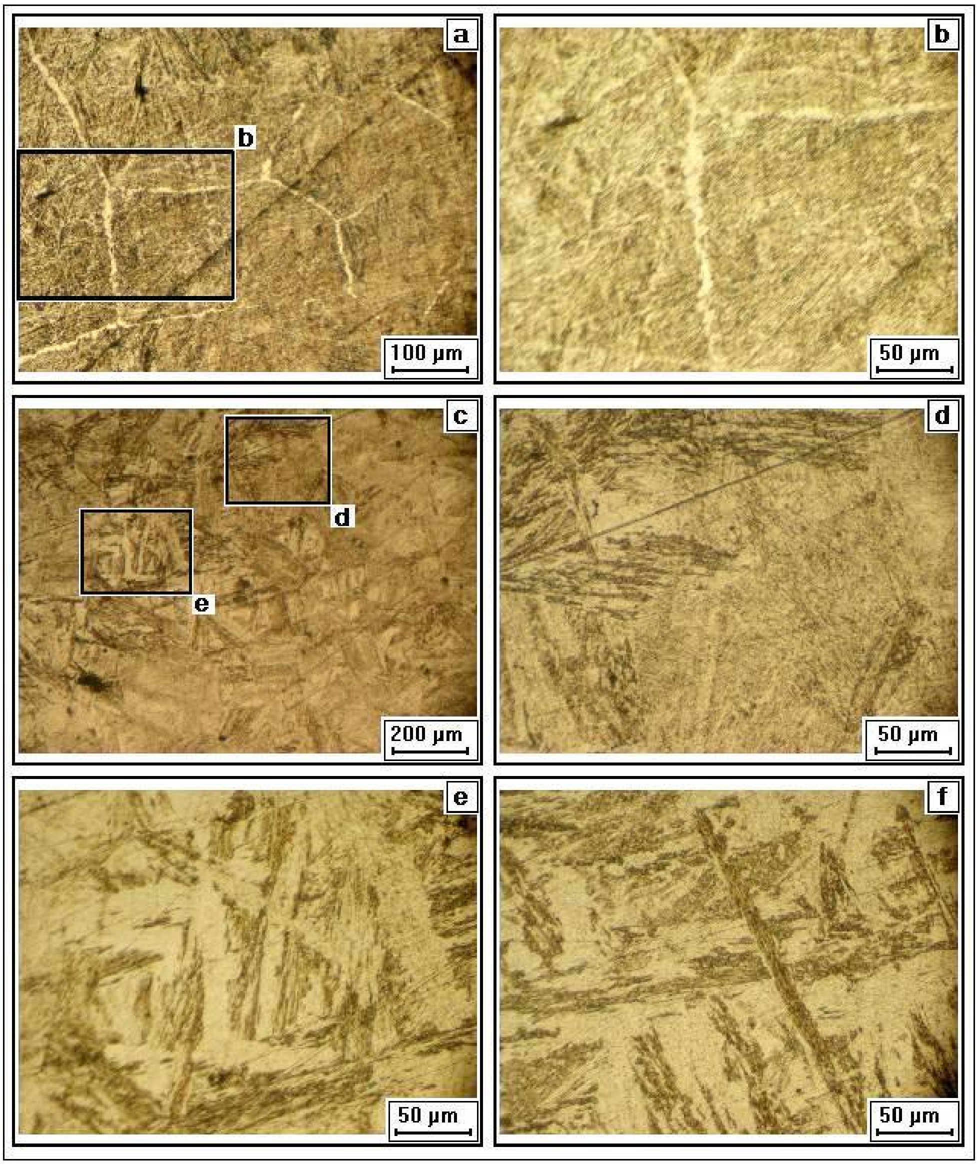

Fig. 2.5.10. Steel microstructure with enlarged fragments in the region marked between lines 4 - 6.

Low-temperature layer between lines 6 - 7 (Fig. 2.5.11).

Line 7 confines the thermal impact zone, there are no structural changes in steel below it. The depth of this zone from the specimen top is 23-24 mm. This is the zone of temperature interval A_1 - A_3 featuring the incomplete transformation of pearlite into austenite. The initial steel grain has grown insignificantly.

The whole thermal impact zone is assumably characterized by carbon and chrome diffusion from hot layers above to cold layers below. This is confirmed by the structure and composition of layers between lines 6 -7. This is lamellar pearlite, which indicates that the composition is eutectoid, having a higher content of carbon than the original steel composition.

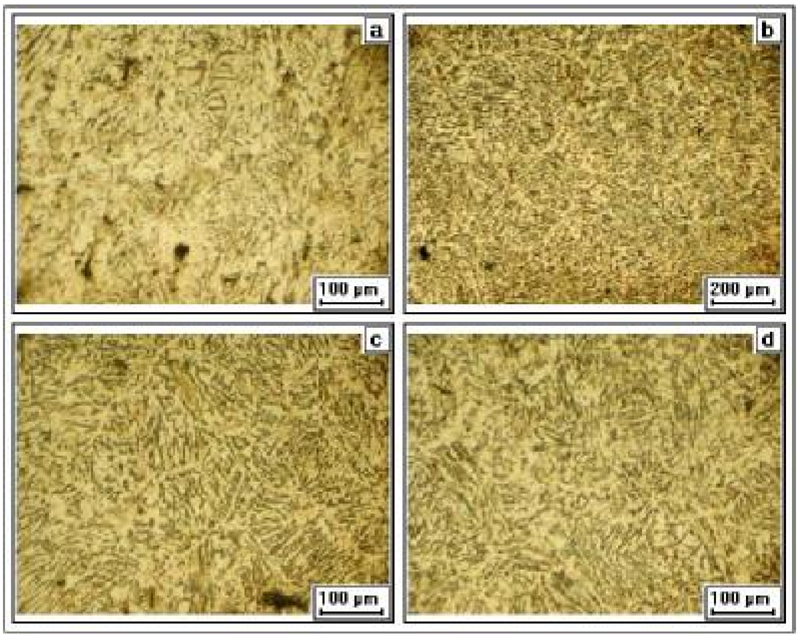

Fig. 2.5.11. Steel microstructure with enlarged fragments in the region marked between lines 6 – 7.

2.5.4. Discussion of results

1). Diffusion of uranium and zirconium into the near-surface steel layers results in the formation of an alloy enriched with U and Zr and having a negligible content of oxygen above line 3 (Fig 2.5.5). The distinct boundary between alloy and steel enables to assume that steel first ablated and afterwards its melt interacted with corium components. It also means that temperature in this zone was higher than steel ablation temperature (T sol - T liq) = (1497 - 1534)ºC, which contradicts the temperature field measurements. Therefore, we must admit that steel composition originally changed due to the diffusion of Zr or U, or both of them, which was followed by the melting of low-temperature alloy along the isotherm.

2). The microstructure of steel affected by high temperatures is sensitive to the content of carbon, diffusion rates and the specimen cooling rate.

Steel microstructure below line (3) consists of ferrite with 0,02% carbon concentration [8], it has grain sizes of 0 - 5. The carbon has evidently left the zone, so only iron alloy is present here.

In the zone between lines (4) and (5) (Fig 2.5.5) another ferrite-pearlite structure of superheated austenite has formed. As the rate of cooling in any point of specimen volume was below 8 - 12 K/s, i.e. sufficiently lower than critical, the formation of martensite is excluded, consequently, we can speak only about pearlite or sorbite. But the sorbite phases can be differentiated on the optical microscope only at the magnification of > 1000^X. We had 50 - 800^X magnification in our optical analysis. So we can see only equilibrium pearlite structure. The presence of carbon redistribution and variations in the cooling rate along the specimen radius results in different modifications of pearlite in its cross section. That is what all our microstructures demonstrate.

3. Discussion of results

The results of a first test with suboxidized corium C~30 enabled to identify a vessel steel corrosion mechanism principally different from the one, which takes place at the interaction between steel and oxidized corium, the latter is characterized by a much higher oxygen potential [2, 8] . The physico-chemical posttest analysis has shown that at a low oxygen potential of corium the vessel steel corrosion follows the eutectics (peritectics) mechanism resulting in the fusible (as compared to steel) metal-iron melt, which is enriched by U and Zr and contains insignificant amount of dissolved oxygen. A peculiar rheology of resultant melt should be noted – the borehole of acoustic defect and technological holes of thermocouples, which were in the zone covered by the melt, remained intact (Fig. 2.4.2, 2.4.29).

As shown by the ultrasonic kinetics measurements, the steel corrosion following this mechanism was preceded by a long-term (about 5 hours) accumulation (induction) period, during which the diffusion of U and Zr from corium through the crust into the surface layer and formation of a liquid sublayer were likely to take place. Initiation of this process (Fig. 2.2.3) can be explained by the changes in the crust thickness/properties at its contact with the liquid sublayer, which provided conditions for a faster transport of reagents (U and Zr) into the zone of eutectics melting. It is shown in [13] that U-Zr-Fe melt wets the suboxidized solid corium, i.e. the oxidic crust can be impregnated by the metallic melt and, if the melt is present in considerable quantities, it can fill the pore space of the crust up to the surface facing the molten corium, which provides good conditions for U and Zr transport from molten corium into the eutectics melting zone. Probably it is the transport of U and Zr that limits the steel corrosion kinetics. Let us note that posttest analysis of the ingot has shown, that after the formation of melt between the steel and corium crust, the latter cracked in some places, which resulted in a partial release of U-Zr-Fe-O melt into the oxidic melt.

With time the steel specimen ablation rate reduced because of the temperature decrease on the interaction interface; after 3 hours the steel corrosion stopped, when the temperature on the interaction boundary, in accordance with posttest calculations of specimen temperature conditions, was ~ 1100-1200°C.

The steel specimen ablation depth before the onset of eutectics melting was ~ 0,27 mm (in accordance with USS readings); the maximum degree of ablation following the eutectics mechanism (at the specimen axis) was 6,7 mm (profilogram of Fig. 2.5.2).

It can be asserted that steel corrosion rate and final depth at the interaction of steel specimen with suboxidized corium depends on the temperature and conditions influencing the rate of U and Zr transport to the steel surface:

- crust thickness and other properties, which depend on the corium-steel heat flux and crust formation history,

- oxygen potential of the melt, which influences the reagent transport to the crust.

In order to describe the phenomena taking place at in-vessel melt retention it is important to know the threshold temperature, at which eutectics interaction starts and below which such interaction stops. For its evaluation let us consider the available data on phase equilibriums in the U-Zr-Fe-O system. In the absence of data about the U-Zr-Fe-O phase diagram let us consider corresponding binary diagrams, which are presented in Fig. 3.1-3.4

Diagrams 3.1-3.2 give an idea about the temperature, at which a liquid forms during the contact of metals. A liquid phase can be formed at a contact of uranium and iron at ~ 725°C (excess of U) or at 1056°C (excess of iron). In the zirconium-iron system the liquid phase is formed at 928°C (excess of Zr) or at 1337°C (excess of iron). Diagram U-Zr (Fig. 3.3) proves the existence of a continuous series of solid solutions in the Zr-U system. Using this diagram we can assert that the temperature, at which the liquid phase formation starts in the (Zr,U)-Fe system will steadily decrease with the increase of U content. Using the data of phase diagram Zr-O (Fig. 3.4) on β-Zr and α-Zr melting temperatures, which show that difference between them is negligible, we can assume that eutectics temperature values in the Zr-Fe and α-Zr(O)-Fe systems will differ insignificantly. As it can be concluded from the phase diagram of Fig. 3.5, in the U-UO_2 system the liquid phase emerges at 1130°C. The presented data enable us to roughly estimate the temperature of liquid phase formation in the U-Zr-Fe-O system at the iron excess, it is 1100°C, which is in agreement with the temperature on the boundary, which we got by the posttest calculation of the MC6 specimen temperature condition (Fig. 2.1.3).

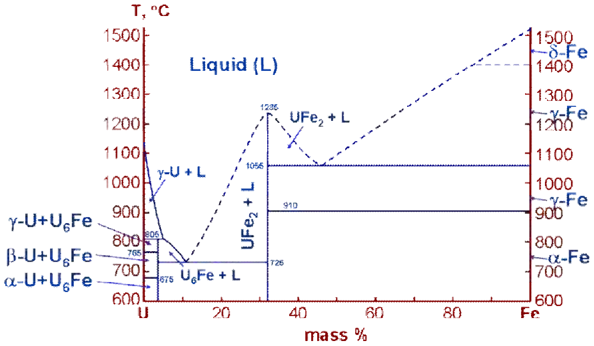

Fig. 3.1 Phase diagram U-Fe [14]

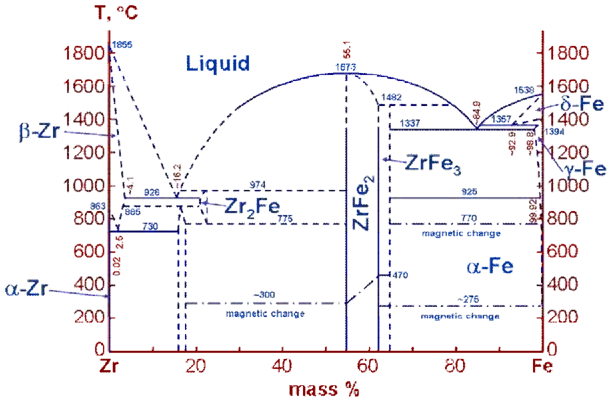

Fig. 3.2 Phase diagram Zr-Fe [15]

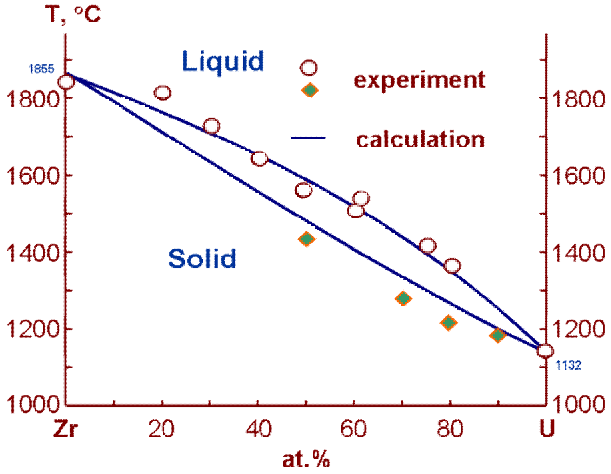

Fig. 3.3 Phase diagram Zr-U [16]

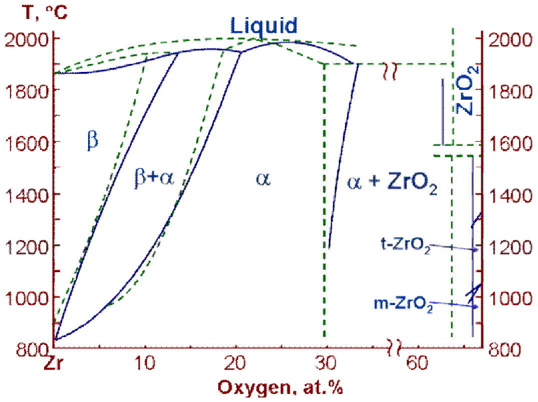

Fig. 3.4. Phase diagram a Zr-O [17]

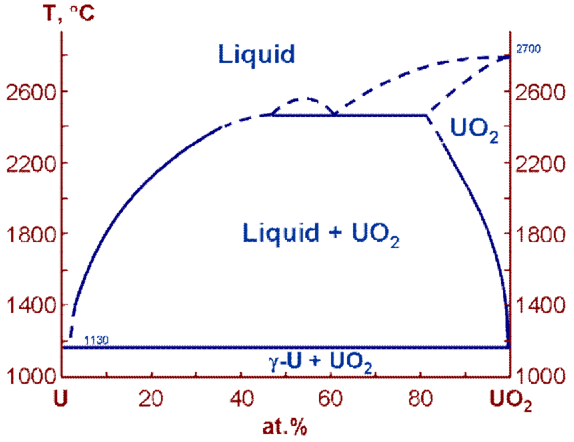

Fig. 3.5 Phase diagram U-UO$_2$ [18]

Scheme illustrating the mechanism of interaction between suboxidized corium and vessel steel is presented in Fig. 3.6.

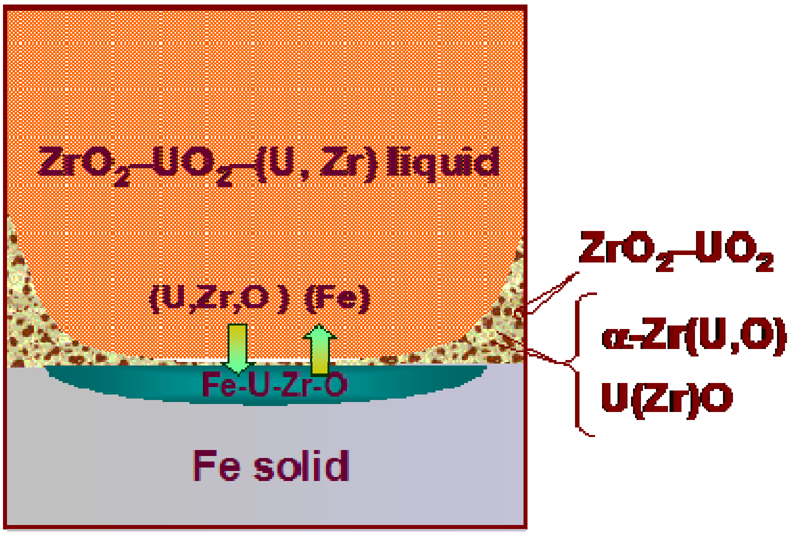

Fig. 3.6 Mechanism of interaction between steel and suboxidized corium

In order to get a better insight into the mechanisms and causes for the accumulative (inductive) period in the interaction process an experiment can be recommended on the interaction of solid corium and vessel steel in the isothermal conditions, the specimen exposition during it would vary from 1 to 10 hours.

In order to specify the temperature, at which the eutectics interaction is started:

- it is planned to take samples of U-Zr-Fe-O melt from MC6 ingot for determining solidus (liquidus) temperatures,
- it is recommended to conduct MC7 test in conditions close to those of MC6, but at lower temperature on the steel surface.

An important implication for further tests within the project is in a further improvement of the ultrasonic sounding method, better quality of information about and enhanced accuracy of steel corrosion depth in conditions, when liquid phases are formed in the interaction zone.

Conclusions

Here is the list of most relevant parameters influencing the corium-steel interaction behavior and quantitative characteristics:

- oxygen potential of the melt, which depends on the melt composition and atmosphere,
- temperature on the interaction interface,

Having compared steel corrosion rates and its final depth influenced by the physico-chemical phenomena taking place at its interaction with corium (Fig.4.1), we can observe that most “favorable”, in terms of in-vessel retention, is the interaction of oxidized (stoichiometric) corium (U,Zr)O_2 (oxidation index of C-100) with steel in neutral atmosphere.

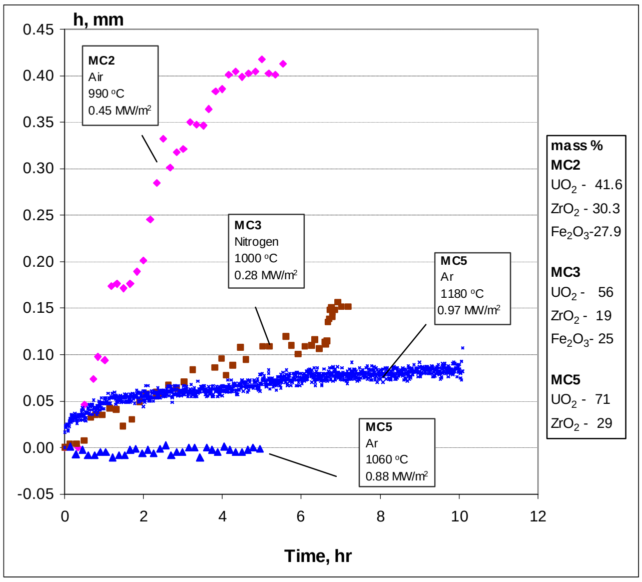

Fig. 4.1 Steel corrosion kinetics in MC 2, 3, 5

The comparison presented in this figure is of approximate nature, because - for the sake of better visualization - the curves, though measured sequentially at different interface temperatures, are set to the same baseline. MC2, MC3 – tests from the 1st Phase of METCOR. [2].

MC 6 steel ablation kinetics is not given in Fig. 4.1, because it is not comparable to the presented data – MC6 temperature on the interaction interface changed with time.

At a lower oxygen potential of the melt (C<100) corium-steel interaction starts following the eutectics mechanism, it is accompanied by the U-Zr-Fe-O melt formation. The interaction accelerates after a delay, which in the given experimental conditions was about 5, this can be explained by the changes in the speed of Zr and U transport into the eutectics melting zone. If we assume that in MC6 within 10 hours the conditions of chemical equilibrium have been reached, we can give a rough estimate of temperature on the interface between the produced melt and solid vessel steel, i.e. the temperature, below which the vessel does not fail, i.e. 1100 – 1200 C. This value is considerably lower than steel melting temperature, which has been previously used in the calculations of in-vessel core retention. The evaluation of minimum interaction temperature requires an experimental clarification.

At a higher oxygen potential (C>100) the physico-chemical interaction between corium and steel also starts, but it follows a different mechanism – diffusion-controlled solid-phase oxidation. The main corroding agent is free oxygen, or oxygen bonded in variable-valence oxides, i.e. the oxidation resources of corium and atmosphere are used. The kinetics of steel corrosion (oxidation) is mainly determined by the diffusion of iron ions through the Wüstite crust that forms on the steel surface [2].

Based on the introduction of generalized – ‘steel corrosion intensity’, which reflects both rate and final depth of corrosion under the temperature on the interaction interface, which decreases as ablation depth increases, then the results of the completed experiments enable us to qualitatively estimate the influence of the melt's degree of oxidation (C) on corrosion intensity. (Fig. 4.2)

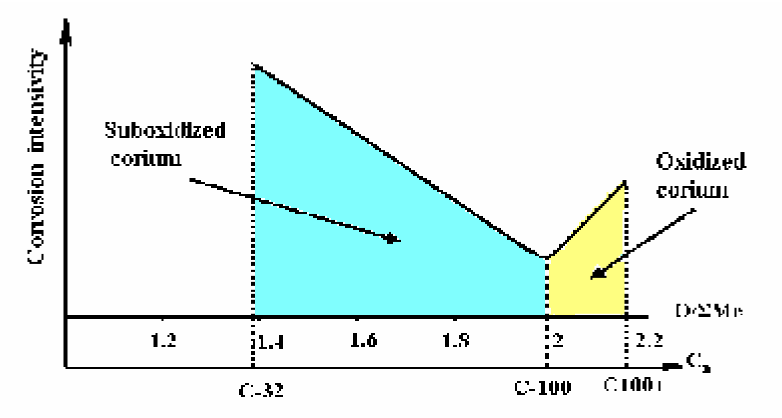

Fig. 4.2 Sensitivity of vessel steel corrosion to the molten corium (C) oxidation degree

The experimental investigation of interaction between the suboxidized molten corium and cooled vessel steel is still in progress, but the very first results of completed tests enabled to reveal new physico-chemical phenomena, which had not been taken into account. Their quantification and modeling will be a priority during further work within the project.

References

1. METCOR Work Plan, Phase 2.
2. V.B. KHABENSKY, S.V. BECHTA, V.S. GRANOVSKY et al., “Investigation of Corium Melt Interaction with NPP Reactor Vessel Steel (METCOR),” *ISTC Project № 833-99. ISTC Final Technical Report* (2001).
3. N.F. Losev. Quantitative X-ray fluorescence. M.:Nauka, 1969,366 p.(In Russian)
4. RASPLAV Final Report. Attachment A. Post-test Examinations Methodology and Results Data published – July, 2000.
5. V.B. Khabensky et al. Methods of physico-chemical analysis // Intermediate report. NITI, MC-02/99, July 1999, (In Russian).
6. G.M. Butirin. High-porosity carbon materials.-M.: Chemistry, 1976,192 p. (In Russian).
7. The determination of picnometric, apparent and gravimetric densities of superfine porous bodies. Manual for laboratory work.-L.:Lensovet LTI,1983, 9 c. (In Russian).
8. V.B. Khabensky, S.V. Bechta et al., “Investigation of corium melt interaction with NPP reactor vessel steel under neutral above-melt atmosphere // Report (METCOR- Phase 2), ISTC Project №3 833.2. (2003). (In Russian).
9. A.P. Guliaev. Metal research. M.: Metallurgy, 1977. (In Russian).
10. I.I. Novikov. Theory of the thermal treatment of metals. M.: Metallurgy, 1986. (In Russian).
11. Yu.M. Lakhrin. Metal research and thermal treatment of metals. M.: Metallurgy, 1993. (In Russian).
12. Thermal treatment in machine building: Reference book / Edited by Yu. M. Lakhtin, A.G. Rakhshtadt – M. Mashinostroenie, 1980, 783 p. (In Russian).
13. V.G. Asmolov, Yu.G. Degaltsev, O.Ya. Shakh, S.S. Abalin, I.M. Semenov, I.F. Isaev, K.V. Pechalin, B.L. Gershman, A.Ye. Ignatochkin, A.B. Grafskiy, V.V. Vlasov, Yu.M. Utkin, A.M. Kovalev
    Study of the Molten Metal Migration in the Oxide Porous Matrix, MASCA project report, MP-TR-5, RRC Kurchatov Institute, July 2003
14. P.Gordon, A.R.Kaufmann // Trans. AIME, 1950, v.188, p.182-184;
    G.G.Michaud // Canadian Met. Quart., 1966, v.5, №4, p.355-365
15. D.Arias, J.P.Abriata // Bull. Alloy Phase Diagr., 1988, v.9, №5, p.597-632
16. T.Ogawa, T.Twai // J. Less-Common Metals, 1991, v.170, №1, p.101-109
17. R.F.Domagala, D.J.McPherson // Trans. AIME, 1954, v.200, p.238;
    E.Gebhardt, H.D.Seghezzi, W.Dürrschnabel // J.Nucl.Mater, 1961, v.4, №3, p.241
18. Ph. Guinet et all // Compt. rend., 1966, v.263, p.17